



**IMPLEMENTATION OF BRANCH-POINT-TOLERANT WAVEFRONT
RECONSTRUCTOR FOR STRONG TURBULENCE COMPENSATION**

THESIS

Michael J. Steinbock, Civ, USAF

AFIT/GE/ENG/12-45

**DEPARTMENT OF THE AIR FORCE
AIR UNIVERSITY**

AIR FORCE INSTITUTE OF TECHNOLOGY

Wright-Patterson Air Force Base, Ohio

**DISTRIBUTION STATEMENT A:
APPROVED FOR PUBLIC RELEASE; DISTRIBUTION UNLIMITED**

The views expressed in this thesis are those of the author and do not reflect the official policy or position of the United States Air Force, the Department of Defense, or the United States Government.

This material is declared a work of the U.S. Government and is not subject to copyright protection in the United States.

IMPLEMENTATION OF BRANCH-POINT-TOLERANT WAVEFRONT
RECONSTRUCTOR FOR STRONG TURBULENCE COMPENSATION

THESIS

Presented to the Faculty
Department of Electrical and Computer Engineering
Graduate School of Engineering and Management
Air Force Institute of Technology
Air University
Air Education and Training Command
in Partial Fulfillment of the Requirements for the
Degree of Master of Science in Electrical Engineering

Michael J. Steinbock, B.S.E.E.,B.S.Co.E.
Civ, USAF

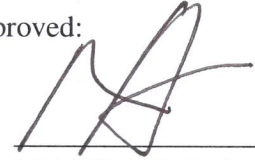
June 2012

DISTRIBUTION STATEMENT A:
APPROVED FOR PUBLIC RELEASE; DISTRIBUTION UNLIMITED

IMPLEMENTATION OF BRANCH-POINT-TOLERANT WAVEFRONT
RECONSTRUCTOR FOR STRONG TURBULENCE COMPENSATION

Michael J. Steinbock, B.S.E.E.,B.S.Co.E.
Civ, USAF

Approved:



Maj Milo W. Hyde, PhD (Chairman)

31 May 2012

Date

1 Jun 2012

Date

5 Jun 2012

Date

Jason D. Schmidt

Jason D. Schmidt, Maj, USAFR (Committee Member)

Salvatore J. Cusumano

Salvatore J. Cusumano, PhD (Committee Member)

Abstract

Branch points arise in optical transmissions due to strong atmospheric turbulence, long propagation paths, or a combination of both. Unfortunately, these conditions are very often present in desired operational scenarios for laser weapon systems, optical communication, and covert imaging, which suffer greatly when traditional adaptive optics systems either cannot sense branch points or implement non-optimal methods for sensing and correcting branch points. Previous research by Pellizzari presented a thorough analysis of various novel branch point tolerant reconstructors in the absence of noise. In this research a realistic model of the Air Force Institute of Technology's adaptive optics system is developed and used for the first realistic tests of these branch point tolerant reconstructors. Utilizing a self-referencing interferometer as the high-order wavefront sensor—this type of sensor being theoretically immune to scintillation—this effort has extended previous theoretical work by adding realistic noise effects to the SRI's measurements before reconstructing the wavefronts and applying the control law. Not only is the adaptive optics correction shown to outperform the traditional techniques by as much as 126%, but several new theories and refinements to existing theories were discovered along the way. This study provides a foundation to guide hardware implementation in the future, where noise effects will be present.

To Russell Lenahan.

Acknowledgements

I owe great thanks to Maj. Jason Schmidt and Dr. Salvatore Cusumano, who originally introduced me to the world of optics as a summer intern and now serve as members of my academic committee. Maj. Schmidt has always gone well out of his way to lend assistance whenever I have asked, and I cannot thank him enough for the time he has put in on my behalf. I value Dr. Cusumano's zeal and humor in a very challenging academic environment. Stories of his exciting career have inspired me to work within the Department of Defense and serve our nation. Of course, I owe a great deal to my advisor, Maj. Milo Hyde. He follows in Maj. Schmidt's footsteps in his utmost dedication to his students. As I continue this research into the future years, I am truly thankful to have Maj. Hyde as my advisor. Most importantly, I wouldn't be here if it wasn't for the love and support from my family. Thank you for giving me the education, tools, and support to bring me here today.

Michael J. Steinbock

Table of Contents

	Page
Abstract	iv
Dedication	v
Acknowledgements	vi
Table of Contents	vii
List of Figures	ix
List of Tables	xiv
List of Abbreviations	xv
I. Introduction	1
1.1 Problem Statement	2
1.2 Key Results	2
1.3 Thesis Overview	5
II. Background and Related Research	6
2.1 Traditional Adaptive Optics	6
2.1.1 Atmospheric Turbulence	6
2.1.2 Wavefront Sensing	12
2.1.2.1 Tilt Tracker	12
2.1.2.2 Shack-Hartmann Wavefront Sensor	13
2.1.2.3 Self-Referencing Interferometer Wavefront Sensor	14
2.1.3 Wavefront Reconstruction	19
2.1.3.1 Linear Algebra	20
2.1.3.2 Zonal Reconstruction	21
2.1.4 Wavefront Correction	22
2.1.5 AO Control	23
2.1.6 Metrics of Performance	25
2.2 Scintillation and Adaptive Optics	27
2.3 Wavefront Reconstruction in Strong Turbulence	31
2.3.1 Post-Processing Congruence Operation Reconstruction	32
2.3.1.1 LSPV	34

	Page
2.3.1.2 Iterative Probing	35
2.3.1.3 Histogram Search	36
2.3.1.4 Brent's Method	37
III. High-Fidelity Simulation Development	38
3.1 AFIT Adaptive Optics System	38
3.1.1 Hardware Specifications and Setup	38
3.1.2 System Radiometry	45
3.1.2.1 Radiometric Assumptions	47
3.1.2.2 Realistic SRI Reference Fiber Coupling	47
3.1.2.3 Power Splitting	49
3.1.3 Sensor Noise Effects	52
3.2 Atmospheric Propagations	54
3.2.1 Parameter Exploration	54
IV. Simulation Results	56
4.1 Reconstructor Performance	56
4.2 Low SNR Reconstruction and Phase Discrepancies	58
4.3 Closed-Loop Behavior of h_{opt}	61
4.4 Fades in Strong Turbulence	66
4.4.1 Potential Fixes	72
4.5 High SNR Phase Discrepancies	74
4.6 Application to Beam Projection	82
V. Conclusions	97
5.1 Challenges Overcome	97
5.2 Key Results	98
5.3 Future Work	101
Appendix A: Detailed Simulation Results	104
Appendix B: PCO Rotational Phase Tilt Propagation	114
Bibliography	119
Vita	123

List of Figures

Figure	Page
2.1 Turbulent eddies shown of size L_0 down to l_0	7
2.2 The Hufnagel-Valley C_n^2 profile model. Figure from [23].	9
2.3 Diagram of a tilt sensor.	14
2.4 Diagram of the Shack-Hartmann WFS.	15
2.5 Diagram of the Point Diffraction Interferometer.	16
2.6 The Self-Referencing Interferometer.	17
2.7 The Fried reconstruction Geometry.	23
2.8 The Hudgin reconstruction Geometry.	24
2.9 Wavefront phase conjugation using a deformable mirror.	25
2.10 High-level control scheme for a tilt compensation system.	26
2.11 Recieved point source irradiance(a) and phase(b) propagated through weak turbulence.	28
2.12 Recieved point source irradiance(a) and phase(b) propagated through strong turbulence.	28
2.13 Effects of the randomized atmosphere on planar phase wavefronts.	29
2.14 Theoretical rotational phase function surrounding a centered branch point in a propagated field.	31
2.15 Effects of adding a uniform piston to the rotational field.	32
2.16 Applying a least squares reconstructor to a rotational field.	33
2.17 Effects of adding a uniform piston to the rotational field.	36
3.1 Layout of AFIT's AO system testbed.	40
3.2 Simulated AO WFS/DM geometry.	40
3.3 The effects of neglecting tilt decoupling on Strehl ratio.	46

Figure	Page
3.4 Optimal process flow for a PCO based reconstruction algorithm.	46
3.5 SRI reference fiber coupling in weak turbulence.	50
3.6 SRI reference fiber coupling in medium turbulence.	50
3.7 Approximate power splitting within the simulated AO system.	51
3.8 Point source atmospheric propagation setup.	55
4.1 Different realizations of unexpected differences between LS noise term and PCO noise term.	62
4.2 Irradiance estimate of input SRI field from noise behavior simulation.	62
4.3 SRI phase measurements of a tilted wavefront where $\text{SNR} \approx 1.5$	63
4.4 Simulation of low-SNR noise effects between least squares and LSPV+1 reconstructors.	64
4.5 Simplified wavefront gradient diagram of a noised induced phase anomaly.	64
4.6 Histograms of h_{opt} as the AO conditions increase in difficulty.	67
4.7 Histograms of h_{opt} as the AO conditions increase in difficulty.	68
4.8 The top plot shows field estimated Strehl ratio and h_{opt} over time with an LSPV+4 reconstructor. The bottom plot shows the IWCL for each of the four ϕ_{rot} realizations over the same time interval. This is in conditions of $\sigma_\chi^2 = 0.5, f_g = 40\text{Hz}, d/r_0 = 1/2$	70
4.9 The top plot shows field estimated Strehl ratio and h_{opt} over time with an LSPV+4 reconstructor. The bottom plot shows the IWCL for each of the four ϕ_{rot} realizations over the same time interval. This is in conditions of $\sigma_\chi^2 = 1, f_g = 40\text{Hz}, d/r_0 = 1/2$	71
4.10 Tilt magnitudes for each PCO rotational phase realization of a LSPV+4 reconstructor over time for weak, medium, and strong Rytov numbers. The higher-order control system is seen to engage at $t = 0.008\text{s}$	73

Figure	Page
4.11 The effects of tilt coupling and controller gain on AO performance.	75
4.12 Plots of AO state in conditions of $\sigma_x^2 = 0.04$, $d/r_0 = 1$. Both tracking and high-order control loops are open.	77
4.13 Plots of AO state in conditions of $\sigma_x^2 = 0.04$, $d/r_0 = 1$. Both tracking and high-order control loops are closed.	78
4.14 Inducing aliasing with the SRI and least squares reconstructor.	79
4.15 Inducing localized aliasing with the SRI and least squares reconstructor. . . .	81
4.16 AO system state during closed loop operation in conditions of $\sigma_x^2 = 0.5$, $d/r_0 = 1$, SNR=60. LSPV+4 is the wavefront reconstructor.	83
4.17 AO system state as the higher-order control loop is closing in conditions of $\sigma_x^2 = 1$, $d/r_0 = 1$, SNR=60. LSPV+4 is the wavefront reconstructor.	84
4.18 Target-plane irradiance patterns using an ideal DM.	88
4.19 Target-plane irradiance patterns using a 10×10 DM with 10% inter-actuator coupling.	89
4.20 Target-plane irradiance patterns using a 19×19 DM with 10% inter-actuator coupling.	90
4.21 Target-plane irradiance patterns using a 32×32 DM with 10% inter-actuator coupling.	91
4.22 Target-plane irradiance patterns using a 10×10 DM with 20% inter-actuator coupling.	92
4.23 Target-plane irradiance patterns using a 19×19 DM with 20% inter-actuator coupling.	93
4.24 Target-plane irradiance patterns using a 32×32 DM with 20% inter-actuator coupling.	94
4.25 Example DM profiles using a 10×10 DM with 20% inter-actuator coupling. . .	95

Figure	Page
4.26 Example DM profiles using a 32×32 DM with 10% inter-actuator coupling. . .	96
A.1 Least-Squares Reconstructor. Weak Turbulence: $\sigma_\chi^2 = 0.04$, $d/r_0 = 1$	105
A.2 LSPV+1 Reconstructor. Weak Turbulence: $\sigma_\chi^2 = 0.04$, $d/r_0 = 1$	105
A.3 LSPV+4 Reconstructor. Weak Turbulence: $\sigma_\chi^2 = 0.04$, $d/r_0 = 1$	106
A.4 Histogram Reconstructor. Weak Turbulence: $\sigma_\chi^2 = 0.04$, $d/r_0 = 1$	106
A.5 Iterative Probing Reconstructor. Weak Turbulence: $\sigma_\chi^2 = 0.04$, $d/r_0 = 1$	107
A.6 Golden-Ratio Reconstructor. Weak Turbulence: $\sigma_\chi^2 = 0.04$, $d/r_0 = 1$	107
A.7 Least-Squares Reconstructor. Medium Turbulence: $\sigma_\chi^2 = 0.5$, $d/r_0 = 1$	108
A.8 LSPV+1 Reconstructor. Medium Turbulence: $\sigma_\chi^2 = 0.5$, $d/r_0 = 1$	108
A.9 LSPV+4 Reconstructor. Medium Turbulence: $\sigma_\chi^2 = 0.5$, $d/r_0 = 1$	109
A.10 Histogram Reconstructor. Medium Turbulence: $\sigma_\chi^2 = 0.5$, $d/r_0 = 1$	109
A.11 Iterative Probing Reconstructor. Medium Turbulence: $\sigma_\chi^2 = 0.5$, $d/r_0 = 1$	110
A.12 Golden-Ratio Reconstructor. Medium Turbulence: $\sigma_\chi^2 = 0.5$, $d/r_0 = 1$	110
A.13 Least-Squares Reconstructor. Strong Turbulence: $\sigma_\chi^2 = 1$, $d/r_0 = 1$	111
A.14 LSPV+1 Reconstructor. Strong Turbulence: $\sigma_\chi^2 = 1$, $d/r_0 = 1$	111
A.15 LSPV+4 Reconstructor. Strong Turbulence: $\sigma_\chi^2 = 1$, $d/r_0 = 1$	112
A.16 Histogram Reconstructor. Strong Turbulence: $\sigma_\chi^2 = 1$, $d/r_0 = 1$	112
A.17 Iterative Probing Reconstructor. Strong Turbulence: $\sigma_\chi^2 = 1$, $d/r_0 = 1$	113
A.18 Golden-Ratio Reconstructor. Strong Turbulence: $\sigma_\chi^2 = 1$, $d/r_0 = 1$	113
B.1 A hypothetical rotational phase (left), and its corresponding least squares reconstruction (right).	115
B.2 The tracker image of the input field, from Fig. B.1.	115
B.3 The four PCO rotational phase realizations from an LSPV+4 reconstructor over the rotational field from Fig. B.1.	116

Figure	Page
B.4 The four corresponding tilt components from each rotational phase realization of Fig. B.3.	117
B.5 The four resulting tracker measurements after the higher-order corrections from each rotational phase realization of Fig. B.3.	118

List of Tables

Table	Page
1.1 Aggregate AO performance gains of all PCO-based wavefront reconstructors over the traditional least squares reconstructor.	3
3.1 Goodrich SU320-KTSW Sensor Specifications	48
3.2 Atmospheric propagation setup parameters.	54
4.1 Averaged field-estimated Strehl ratios over all Greenwood frequencies and SNR's tested for the cases listed.	57
4.2 Field-estimated Strehl ratio standard deviation, averaged over all Greenwood frequencies and SNR's tested for the cases listed.	57
4.3 Field-estimated Strehl ratio normalized standard deviation, averaged over all Greenwood frequencies and SNR's tested for the cases listed.	57
5.1 Aggregate AO performance gains of all PCO-based wavefront reconstructors over the traditional least squares reconstructor.	99

List of Abbreviations

Abbreviation		Page
DoD	Department of Defense	1
DE	Directed Energy	1
AO	Adaptive Optics	1
WFS	Wavefront Sensor	1
DM	Deformable Mirror	1
MCF	Mutual Coherence Function	11
WSF	Wave Structure Function	11
FSM	Fast-Steering Mirror	13
SRI	Self-Referencing Interferometer	14
PDI	Point Diffraction Interferometer	14
LSI	Lateral Shearing Interferometer	21
MEMS	Micro-Electro-Mechanical System	23
DAC	Digital-to-Analog Converter	24
OTF	Optical Transfer Function	26
PCO	Post-Processing Congruence Operation	32
IWCL	Intensity Weighted Cut Length	34
LSPV	Least Squares Principle Value	34
tOSC	the Optical Sciences Company	38
LSB	Least Significant Bit	53
CL	Cut Length	82

IMPLEMENTATION OF BRANCH-POINT-TOLERANT WAVEFRONT RECONSTRUCTOR FOR STRONG TURBULENCE COMPENSATION

I. Introduction

WITHIN the Department of Defense (DoD), directed energy (DE) capabilities have been identified as one of “the key ‘game-changing’ technology-enabled capabilities that enters service during [the next two decades]” [44]. DE spans a wide range of potential applications yet has many technological challenges still to be overcome. Applications of particular interest to the DoD are space situational awareness, laser communication, and laser weapon systems [44]. Currently, a major obstacle in each of these applications is accounting for the optical aberrations induced by the random nature of Earth’s atmosphere. For a point of reference, these same atmospheric effects are what prompted NASA to spend billions of dollars to design and maintain the Hubble Space Telescope. To deal with these atmospheric aberrations, there are only a handful of possibilities. Adaptive optics (AO) utilizes a wavefront sensor (WFS) and reconstructor to estimate the optical distortions on some reference beam traveling through the atmospheric path of interest. Subsequently, a wavefront corrector, such as a deformable mirror (DM), removes the estimated distortions. While there are other methods for dealing with Earth’s random effects on light, AO is unique in providing real-time, improved imaging performance, which is essential for the above applications of interest.

Current AO techniques only provide good correction capability for limited operational regimes. As the optical propagation paths lengthen and/or the atmospheric turbulence becomes stronger, the propagated light begins to constructively and destructively interfere with itself [5]. In these circumstances, traditional wavefront reconstruction techniques

used to drive the optical correction process are unable to completely estimate the optical aberrations. These situations are of definite operational interest to the DoD, but most current AO techniques lose effectiveness in these more challenging situations [31, 39, 42]. The research presented here is aimed at extending the operational regime of AO to offer improved correction capability when optical interference begins to severely degrade performance of traditional AO techniques.

1.1 Problem Statement

Branch points arise in optical transmissions due to strong atmospheric turbulence, long propagation paths, or a combination of both. Unfortunately, these conditions are very often present in desired operational scenarios for laser weapon systems, optical communication, and covert imaging, which suffer greatly when traditional adaptive optics systems either cannot sense branch points or implement non-optimal methods for estimating and correcting branch points. The overall goal for this research is to transition previous theoretical work in optimized wavefront reconstruction for strong turbulence AO to an initial implementation in hardware. To bridge the transition, a high-fidelity computer model is developed and used in testing the new algorithms prior to hardware implementation. The work in simulation is shown to be invaluable in further investigating the behavior of the new wavefront reconstruction algorithms with many unanticipated lessons and discoveries.

1.2 Key Results

This research primarily investigated the behavior and properties of post-processing congruence operation (PCO) based wavefront reconstructors. The following list summarizes the contributions made in this research towards bringing the PCO-based reconstructor to an implementable state.

- *Demonstrated greatly improved strong turbulence AO performance in terms of both mean Strehl and Strehl variance.* The AO performance gains using a PCO wavefront reconstructor over the traditional least squares reconstructor in terms of mean field estimated Strehl ratio and Strehl ratio normalized standard deviation are summarized in Table 1.1. Mean Strehl is a metric of absolute AO correction performance (higher is better), and the Strehl standard deviation is a metric of correction stability (lower is better). These results were presented at the 2012 IEEE Aerospace conference.

Table 1.1: Aggregate AO performance gains of all PCO-based wavefront reconstructors over the traditional least squares reconstructor.

σ_x^2	Mean Strehl	Normalized Strehl Standard Deviation
0.04	0.2%	-2.4%
0.5	19.1%	-50.6%
1	126.4%	-57.6%

- *Identified cause of fades from PCO-based AO and demonstrated a potential solution.* When in closed-loop operation in strong turbulence, PCO algorithms can cause short-term fades as h_{opt} varies. These drops in Strehl are not caused by the higher-order control law as much as different tilt components associated with each PCO rotational realization. The tilt is removed from the higher-order corrections and instantly dumped on the tracking system; causing the fades. One solution was found by allowing tilt in the higher-order corrections with conservative controller gains. This prevented the fades with a slight tradeoff in mean Strehl ratio. Unfortunately, a realistic system with slight misalignments would require a zero-DC-gain control law to implement a similar solution. Additionally, this puts higher stroke requirements

on the DM when tilt is being included. With this new understanding future work in control design could help mitigate these fades based on the application requirements.

- *Demonstrated and developed theory on improved PCO performance in weak turbulence, low SNR regimes.* In weak turbulence, where no branch points are present, a consistent performance improvement of the PCO reconstructors over traditional least squares was found. Although the difference is small, this was completely unexpected based on previous concerns of noise corrupting the PCO process. A new theory proposed by the author shows in high-noise conditions, least squares reconstructors can introduce phase anomalies to the AO corrections. However, the PCO process removes these phase discrepancies introduced by the least squares reconstruction. These findings will be presented at the 2012 SPIE Optics and Photonics conference.
- *Developed a set of theories regarding phase anomalies in high wavefront gradient conditions.* When localized wavefront phases being reconstructed from an SRI are greater than π radians between adjacent subapertures, the least squares reconstructor will alias, leading to a phase anomaly in the reconstructed field. This can be mitigated using a higher density of SRI subapertures, at the cost of SNR. Alternatively, initial results show the PCO corrects the phase anomalies introduced by the least squares reconstruction.
- *Formulated an optimized data flow for an AO system using PCO.* Started by diagnosing coupling between the high-order and tracking control systems when using a PCO-based wavefront reconstructor. Since PCO reconstruction is not a single matrix operation, decoupling tilt from the higher-order commands required a new data flow process. The resulting process, illustrated in Fig. 3.4, minimizes matrix multiplies while maximizing AO effectiveness.

- *Conducted first beam projection simulations using PCO wavefront reconstruction techniques.* Conducted at the end of this research, this establishes a foundation for future efforts to investigate these novel reconstruction methods with respect to beam projection applications. Although the initial simulation results identified needed changes, initial observations indicate promise over traditional least squares reconstruction. The identified flaws have since been fixed and follow-up simulation results will be presented at the 2012 DEPS Beam Control Conference.
- *Developed an extensible AFIT AO system model for future research.* The model is configurable to varying levels of realism and AO capabilities. Allows isolation of the research problem at hand without the difficulties of hardware work and the assumptions of analytical work. This includes the first modeling of realistic fiber coupling to our specific SRI optical setup – crucial to realistic noise modeling.

1.3 Thesis Overview

Chapter II provides an overview of traditional AO and the optical effects as a result of the randomized atmosphere. This is followed by an introduction to branch points and the previous theoretical work in developing an optimized branch-point tolerant wavefront reconstructor. Chapter III describes a high-fidelity computer simulation developed to model AFIT’s AO system. This model exposed new insights, crucial to a successful implementation of the new reconstruction techniques. These insights, discussed in Ch. IV, offer explanations to a number of previously posed questions, and a new extension of the theory is presented for beam projection applications. Finally, Ch. V presents a summary of the challenges overcome, key contributions, and suggested future work from this research effort.

II. Background and Related Research

This chapter introduces the current state of AO and previous theoretical methods for extending AO operability into regimes with scintillation present. An overview of a typical AO system is given, along with two WFS types - each with unique strengths and weaknesses. Following this, the detrimental effects of scintillation are explained with respect to AO. This chapter concludes by discussing previous research in specialized wavefront reconstruction techniques that attempt to improve upon traditional reconstructors when branch points are present in the received beacon wavefronts.

2.1 Traditional Adaptive Optics

As light propagates through Earths atmosphere, stochastic variations in temperature and pressure cause the light to both diffract and refract [5]. This causes beam wander, beam spreading, and phase fluctuations. A simple example of this can be observed in the apparent twinkle of stars at night. The Hubble Space Telescope was built to operate beyond the random atmosphere, where the stars appear as sharp objects. For many applications, these atmospheric effects severely limit performance. For instance, beam projection systems rely on efficient delivery of light to a small target area, and optical communication must maintain a reliable optical link. One remedy is to estimate the atmospheric distortions and correct for them in real time. This approach is called AO, utilizing a WFS and reconstructor to estimate the optical distortions on some reference beam followed by a wavefront corrector to mitigate the estimated distortions.

2.1.1 *Atmospheric Turbulence.*

Within the atmosphere, light is distorted as it encounters spatially and temporally randomized variations in the air's index of refraction. The statistical behavior of these random variations were first described in the 1940's by Kolmogorov, when he used physical

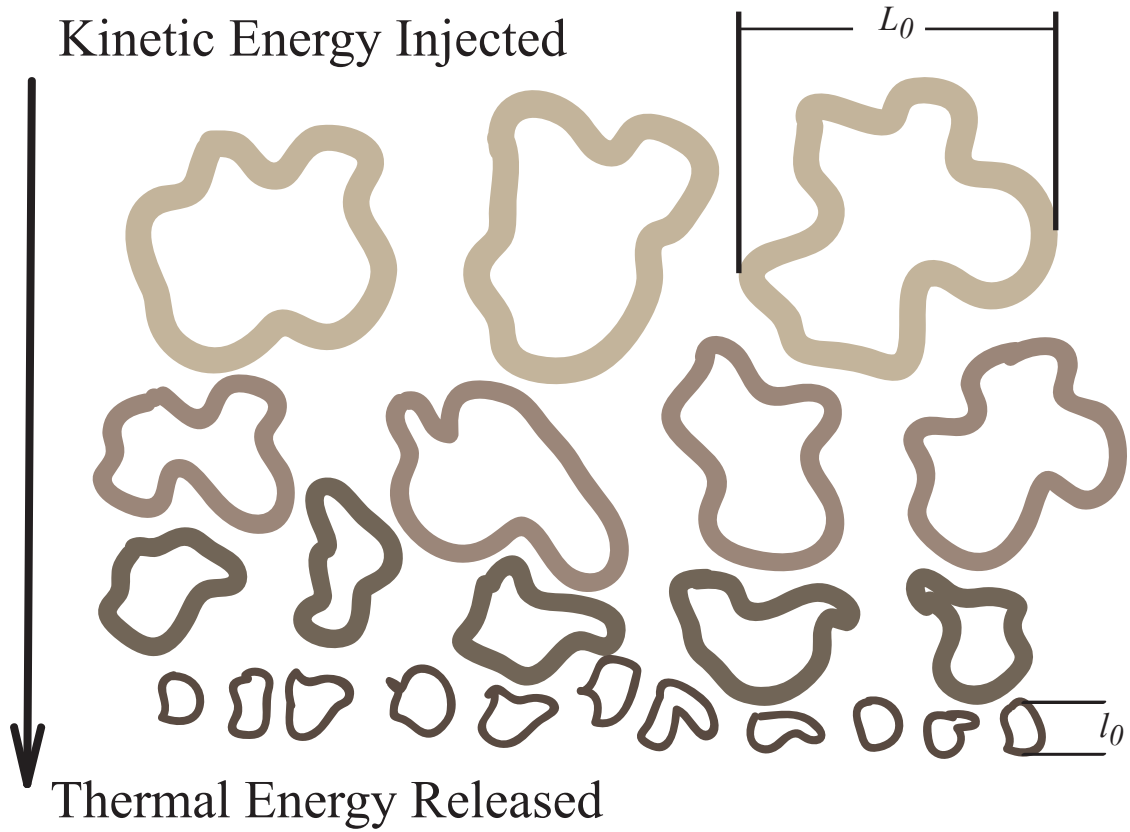


Figure 2.1: Turbulent eddies shown of size L_0 down to l_0 .

insights to describe the velocity of air within the atmosphere [5]. Energy cascade theory says that kinetic energy injected to a viscous fluid creates large sized turbulent eddies. These large eddies break down into progressively smaller eddies before the energy is eventually transferred into heat. The dimensions of these eddies are described by the inertial subrange, where eddie sizes fall between the inner scale, l_0 , and outer scale, L_0 . Within the inertial subrange, the turbulence can be considered statistically homogenous and isotropic [5]. Figure 2.1 provides a visual depiction of the energy cascade theory as kinetic energy is converted down into thermal energy.

With this physical foundation, Kolmogorov was able to formulate a one dimensional structure function for wind velocities within the inertial subrange [5]. From this, one can derive three dimensional power spectrum of the velocity fluctuations within the atmosphere [17]:

$$\Phi_{RR}(\kappa) = 0.066\epsilon^{2/3}\kappa^{-11/3}, \quad (2.1)$$

where κ is the scalar spatial frequency (in units of rad/m) and ϵ is the average energy dissipation rate of the atmosphere. By defining C_V^2 as the velocity structure constant,

$$C_V^2 = 2\epsilon^{2/3}, \quad (2.2)$$

Eq. (2.1) can be simplified to

$$\Phi_{RR}(\kappa) = 0.033C_V^2\kappa^{-11/3}. \quad (2.3)$$

The velocity structure constant, with units of $\text{m}^{4/3}/\text{s}^2$, provides a quantitative evaluation of the energy within the atmospheric turbulence and is actually based in the formulation of the velocity structure function [5].

From Kolmogorov's work, Obukhov [28] and separately Corrsin [8] were able to extend his statistical model of atmospheric velocity variations, first to potential temperature, and later to index of refraction variations. This important final leap directly relates the phase aberrations accumulated by light to the randomized atmosphere. The resulting three dimensional refractive index power spectrum, known as the Kolmogorov spectrum, is given by

$$\Phi_n(\kappa) = 0.033C_n^2\kappa^{-11/3}, \quad (2.4)$$

where n is the index of refraction and C_n^2 is the index of refraction structure constant. C_n^2 is a physical quantity that can be measured for a given location, time of day, and altitude. Several models of C_n^2 exist that can be used for simulations of a desired scenario [5]. Figure 2.2 shows the commonly used Hufnagel-Valley model, along with many of the

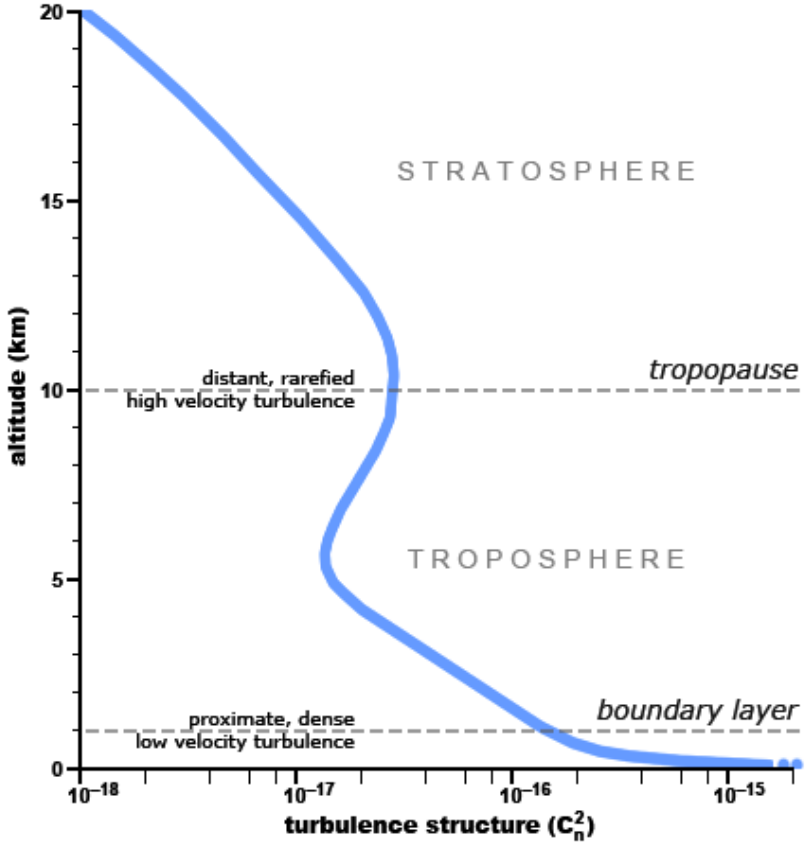


Figure 2.2: The Hufnagel-Valley C_n^2 profile model. Figure from [23].

physical atmospheric layers that drive its behavior. For this research, a horizontal path was assumed - implying a constant C_n^2 along the propagation path.

It is important to note the power spectral models for velocity, temperature, and index of refraction variations all follow similar behavior - easily seen by comparing Eqs. (2.3) and (2.4). However, as presented thus far, effects outside the inertial subrange have been ignored. The Kolmogorov spectrum actually assumes an infinitely large outer-scale and infinitely small inner-scale. This is an assumption made for mathematical simplicity, but does not match the true atmospheric fluidics. Hill developed a numerical model based on a more detailed hydrodynamic analysis [20], later adapted to analytic form

by Andrews [4], given by

$$\Phi_n(\kappa) = 0.033C_n^2 \left[1 + 1.802 \left(\frac{\kappa}{\kappa_l} \right) - 0.254 \left(\frac{\kappa}{\kappa_l} \right)^{7/6} \right] \frac{\exp(-\kappa^2/\kappa_l^2)}{\left(\kappa^2 + \kappa_0^2 \right)^{11/6}}, \quad (2.5)$$

$$0 \leq \kappa < \infty, \quad \kappa_l = 3.3/l_0, \quad \kappa_0 = 2\pi/L_0. \quad (2.6)$$

This is sometimes called the modified atmospheric spectrum, where the math to the right of C_n^2 has been added to Eq. (2.4) to match the results found by Hill. Most notably, this spectrum model includes a spectral bump at wavenumbers near the inner-scale size. As the inner-scale size decreases, light begins to diffract at the smaller eddies [5]. With the Hill spectrum's increased content of small eddie sizes, scintillation effects are seen earlier than a similar propagation using a Kolmogorov spectrum. For this research, the modified spectrum was used in all numerically propagated optical fields.

Mathematically, Maxwell's Equations govern all electromagnetic interactions. In optics, these equations are typically simplified by making three key assumptions:

1. Negligible backscattering and polarization effects.
2. The Markov approximation. Assumes the atmospheric refractive index variations are delta correlated in the direction of propagation.
3. The paraxial approximation. Assumes all light rays of interest travel at angles very near the optical axis.

From these simplifications, several methods exist for applying Maxwell's equations to propagating an initial field through a random medium. For regimes of weak turbulence, one such method is the Rytov approximation [5]:

$$U(\mathbf{r}, L) = U_0(\mathbf{r}, z = L) \exp [\Psi(\mathbf{r}, L)], \quad (2.7)$$

where the initial field is propagated a distance L , $U_0(\mathbf{r}, L)$ is the field propagated through vacuum, and it is modified by the complex phase perturbation, $\Psi(\mathbf{r}, L)$. Further, the

perturbation can be split into amplitude and phase components [38]

$$\Psi = \chi + i\phi. \quad (2.8)$$

Several statistical parameters of the propagated field $U(\mathbf{r}, L)$ can be found using the Rytov approximation described above. First, define the field's mutual coherence function (MCF),

$$\begin{aligned} \Gamma(\mathbf{r}, \mathbf{r}', L) &= \langle U(\mathbf{r})U^*(\mathbf{r}') \rangle \\ &= U(\mathbf{r})U^*(\mathbf{r}')\langle \exp [\psi(\mathbf{r})\psi^*(\mathbf{r}')] \rangle. \end{aligned} \quad (2.9)$$

By taking the modulus of the MCF, the field's spatial coherence can be found - also called the degree of coherence:

$$\begin{aligned} \gamma(\mathbf{r}, \mathbf{r}', L) &= \frac{|\Gamma(\mathbf{r}, \mathbf{r}', L)|}{\sqrt{\Gamma(\mathbf{r}, \mathbf{r}, L)\Gamma(\mathbf{r}', \mathbf{r}', L)}} \\ &= \exp \left[-\frac{1}{2}D(\mathbf{r}, \mathbf{r}', L) \right], \end{aligned} \quad (2.10)$$

where $D(\mathbf{r}, \mathbf{r}', L)$ is the wave structure function (WSF) [17]. Assuming homogeneity, isotropy, and a spherically expanding source, the WSF is

$$D_{sph}(\rho, L) = 8\pi^2 k^2 \int_0^L \int_0^\infty \kappa \Phi_n(\kappa) \left\{ 1 - J_0 \left[\left(1 - \frac{z}{L} \right) \kappa \rho \right] \right\} d\kappa dz, \quad (2.11)$$

where ρ is the distance from the optical axis, $k = 2\pi/\lambda$ is the optical wavenumber, J_0 is a Bessel function of the first kind, order zero, and $\Phi_n(\kappa)$ is the atmospheric index of refraction spectrum model being used. For analytic tractability, the Kolmogorov atmospheric spectrum is assumed for the following definitions.

By substituting the Kolmogorov spectrum into Eq. (2.11), further substituting that into Eq. (2.10), and solving for the e^{-1} point one can find the spatial coherence radius of the field, ρ_0 . However, the more commonly used term, $r_0 = 2.1\rho_0$, called the seeing parameter, can be shown to be [5]

$$r_{0,sph} = \left[0.423k^2 \int_0^L C_n^2(z) \left(\frac{z}{L} \right)^{5/3} dz \right]^{-3/5}. \quad (2.12)$$

This is also referred to as Fried's parameter after being introduced by D. L. Fried [9]. With respect to AO, r_0 is a critical parameter for designing a system. Apertures larger in diameter than r_0 require AO to see additional gains in imaging resolution. Further, the spatial density of wavefront estimation and correction by an AO system are often related to r_0 . To be effective, roughly one WFS subaperture and DM actuator spacing should span r_0 .

To describe the temporal coherence of the field aberrations, Greenwood analyzed an ideal AO system with a single pole control filter. He calculated the characteristic frequency of the system with respect to the ratio of aperture diameter to r_0 [19] and derived what is now called the Greenwood frequency:

$$f_g = 0.254k^{6/5} \left[\int_0^L C_n^2(z) v^{5/3}(z) dz \right]^{3/5}, \quad (2.13)$$

where $v(z)$ is the perpendicular wind velocity along the propagation path.

2.1.2 *Wavefront Sensing.*

The first step to mitigate the atmospheric effects on light is to be able to estimate the distortions introduced for a given propagation path and instant in time. This process is called wavefront sensing and requires some form of reference beacon transmitting light through the turbulence column of interest. With longer electromagnetic wavelengths, such as in radar, the fields of interest can be directly measured and compared. Unfortunately, in optics the short wavelengths and corresponding high frequencies are beyond the detection range of current electronics. In optics, wavefront estimation requires inferring information about the received beacon field from other physical processes [41]. The following subsections give an overview of three such methods.

2.1.2.1 *Tilt Tracker.*

One of the most simplistic wavefront sensors is a tilt sensor. Shown in Fig. 2.3, this sensor is meant to estimate the low-order wavefront aberrations of x and y tilt. By focusing incoming light onto a quadcell detector or sensor array, the deflection of the focused light

can be calculated by the centroid equations

$$\Delta x = \frac{\sum_{x=1}^N x I_x}{\sum_{x=1}^N I_x} - \bar{x}, \quad \Delta y = \frac{\sum_{y=1}^N y I_y}{\sum_{y=1}^N I_y} - \bar{y}, \quad (2.14)$$

where x and y denote detector column and row positions, \bar{x} and \bar{y} are the mean column and row, and I_x and I_y are the summed detected irradiance values for each column and row. Using the results from Eq. (2.14), the incoming wavefront's mean tilt can be determined as

$$\theta_x = \Delta x / f, \quad \theta_y = \Delta y / f, \quad (2.15)$$

where f is the focal length of the focusing optic used, shown in Fig. 2.3.

Tilt comprises approximately 87% of all atmospheric aberrations [27], and as such, using a dedicated fast-steering mirror (FSM) to compensate tilt alone offloads a large stroke requirement from the high-order wavefront corrector [25]. Further, the tracker can be used with broadband light, has no moving parts, and is computationally simple to operate. These reasons make the tracker a very robust wavefront sensor; however, it can only sense the lowest order wavefront aberrations.

2.1.2.2 *Shack-Hartmann Wavefront Sensor.*

The Shack-Hartmann WFS uses a tiled array of trackers across the aperture. This divides the full aperture into subapertures, whose incident wavefronts are assumed to be roughly planar. With this architecture, local wavefront tilts, or gradients, are sensed which are then pieced together using a wavefront reconstruction algorithm - discussed in Sec. 2.1.3. Because of this aperture averaging effect with respect to high order wavefront aberrations, it is advisable to have at least one subaperture per r_0 spacing of the wavefront being sensed [25].

Figure 2.4 shows a Shack-Hartmann design using square lenslets that focus down on to 2×2 pixel regions on a larger focal plane array. This is a typical design, but other variations exist for a range of applications. One common design decision is to include a band of unsensed pixels between subapertures to prevent light from one subaperture 'spilling' into

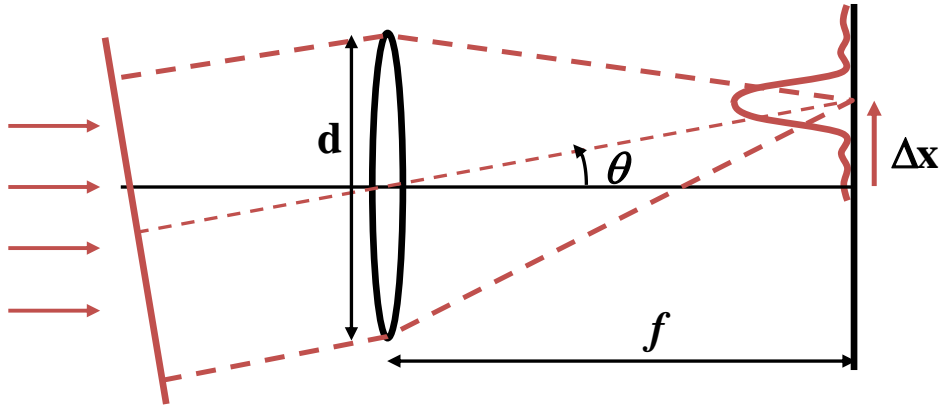


Figure 2.3: Principles of operation for a tilt sensor where θ is the incoming wavefront mean tilt with respect to the sensor's optical axis, d is the lens diameter, f is the effective focal length, and Δx is the lateral shift of the focal pattern irradiance.

an adjacent subaperture's sensed pixels. However, this requires the use of a larger and more expensive focal plane array and typically increases the required sensor readout time. This wavefront sensor is very widely used as it shares the same benefits as the tracker does. The primary downside of this WFS is its high sensitivity to alignment errors. As in most WFS's there is a tradeoff to be made between dynamic range of detectable wavefront tilts, measurement accuracy, signal sensitivity, and speed.

2.1.2.3 Self-Referencing Interferometer Wavefront Sensor.

The Self-Referencing Interferometer (SRI) WFS uses interference effects to directly sense an incoming field, as opposed to most WFS designs which measure some form of wavefront gradients. It is based on the point diffraction interferometer (PDI), shown in Fig. 2.5. The PDI focuses all incoming light to a partially transmissive filter in the focal plane. The on-axis point in the filter is completely transmissive, acting as a spatial filter.

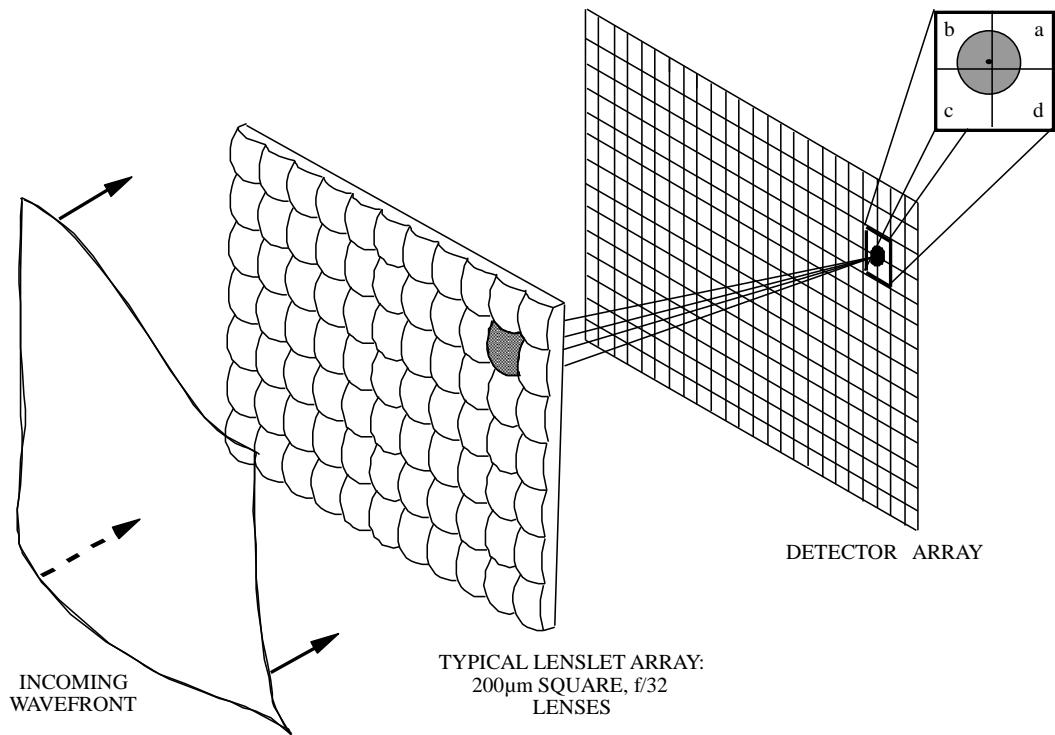


Figure 2.4: Diagram of the Shack-Hartmann WFS.

When the light is recollimated, an interferogram between the aberrated input wavefront and spatially filtered reference wavefront can be seen [24, 34].

Unfortunately, the single interferogram produced by a PDI does not give a direct means of forming a wavefront estimate, but this is where the SRI extends. Here, the incoming light is split into two separate paths before being recombined. The first path is responsible for spatially filtering the incoming wavefronts, similar to the pinhole filter used in the PDI. However, in the SRI a single-mode fiber is used instead of a pinhole filter. Differently from the PDI, this filtered reference beam is further split up into separate beams, and each beam receives a different phase shift – explained below. The second path applies no filtering or altering of the beam, but is carefully matched in length to the reference

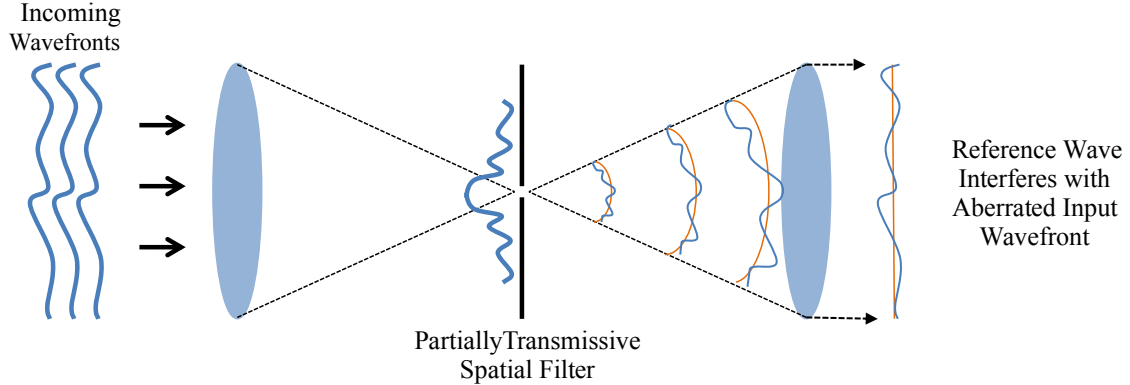


Figure 2.5: Diagram of the Point Diffraction Interferometer.

legs to maintain a high degree of temporal coherence. Finally, each phase shifted beam is recombined with the beacon wavefront to form an interferogram for each. The irradiance pattern of each interferogram is measured on an imaging sensor for use in calculating the wavefront phase. Figure 2.6 shows a simple layout for an SRI.

A direct measurement of the input wavefront phase can be calculated using the separate interferograms [11, 34]. Assuming a perfectly coherent source, the m -th sensed pixel of the n -th interferogram follows

$$I_n(x_m, y_m) = \int \int_{\mathcal{A}_m} |U_b(x, y) + U_r(x, y)e^{-i\theta_n}|^2 dx dy, \quad (2.16)$$

where U_b is the input beacon field, U_r is the reference field, and \mathcal{A}_m is the area of the corresponding pixel. If we assume the amplitudes of both fields are equal to $A/2$, Eq. (2.16) can be shown to equal

$$I_n(x_m, y_m) = A \left[1 + \cos(\phi_{bx_m, y_m} + \theta_n) \right]. \quad (2.17)$$

Here, the planar nature of the reference wavefront is clear, while the aberrated input wavefront remains a function over x_m and y_m . There are multiple methods for calculating

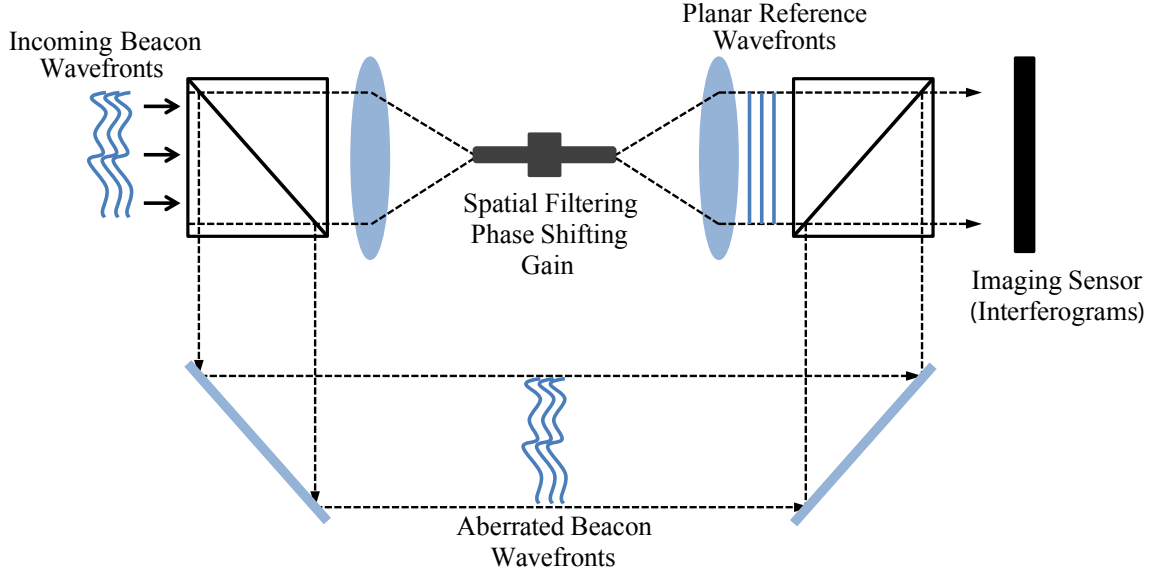


Figure 2.6: The Self-Referencing Interferometer.

the input wavefront phase using different numbers of interferograms with different reference phase shifts applied [11]. For this research, a four bin approach is used. In this configuration, phase shifts of 0 , $\pi/2$, π , and $3\pi/2$ are applied respectively to each reference beam, each interferogram constituting a bin. Following Eq. (2.17), the measured irradiances of each interferogram become

$$\begin{aligned}
 I_1(x_m, y_m) &= A + A \cos(\phi_{b(x_m, y_m)}) \\
 I_2(x_m, y_m) &= A \left[1 + \cos(\phi_{b(x_m, y_m)} + \frac{\pi}{2}) \right] = A - A \sin(\phi_{b(x_m, y_m)}) \\
 I_3(x_m, y_m) &= A \left[1 + \cos(\phi_{b(x_m, y_m)} + \pi) \right] = A - A \cos(\phi_{b(x_m, y_m)}) \\
 I_4(x_m, y_m) &= A \left[1 + \cos(\phi_{b(x_m, y_m)} + \frac{3\pi}{2}) \right] = A + A \sin(\phi_{b(x_m, y_m)})
 \end{aligned} \tag{2.18}$$

From this system of equations, the aberrated input wavefront can be easily calculated according to Eq. (2.19) and (2.20):

$$\tan(\phi_{b(x_m, y_m)}) = \frac{\sin(\phi_{b(x_m, y_m)})}{\cos(\phi_{b(x_m, y_m)})} = \frac{I_4(x_m, y_m) - I_2(x_m, y_m)}{I_1(x_m, y_m) - I_3(x_m, y_m)} \tag{2.19}$$

$$\hat{\phi}_{SRI} = \text{Tan}^{-1} \left(\frac{\mathbf{I}_4 - \mathbf{I}_2}{\mathbf{I}_1 - \mathbf{I}_3} \right). \quad (2.20)$$

For some applications, including the strong turbulence reconstruction techniques in Sec. 2.3, it is important to note that the complete field estimate is available with the relationship

$$\hat{\mathbf{U}}_{SRI} = (\mathbf{I}_4 - \mathbf{I}_2) + i(\mathbf{I}_1 - \mathbf{I}_3), \quad (2.21)$$

from which the field irradiance can be calculated.

Equation (2.20) reveals a remarkable point of interest for real-time AO: using an SRI, the wavefront phase can be directly measured by merely subtracting the measured interferograms, one division, and performing an inverse tangent operation on that result. Further, for a spatial shifting SRI these operations can be performed independently for each subaperture, meaning that calculations can begin immediately as pixel data from each interferogram is read in from the sensor(s). To capitalize on this advantage, thought must be given to the pixel readout order of the sensor(s). The computational time required by the arctangent operation is a tiny fraction of the full wavefront reconstruction required for a Shack-Hartmann. However, the output of the arctangent is wrapped $[-\pi, \pi]$, which is well suited for a segmented DM, but is difficult to reproduce over a continuous face-sheet DM. In the case of a continuous face-sheet DM, one needs to implement a wavefront reconstruction algorithm in the control system [10, 14, 30]. Due to the influence functions of a continuous face DM, sharp wrapping cuts are difficult to reproduce and may even cause damage to hardware. Unfortunately, the reconstruction process eliminates the efficiency gains seen over the Shack-Hartmann WFS.

The SRI still has one major advantage over other WFS technologies in that it is nearly immune to the effects of scintillation seen in strong atmospheric turbulence. A scintillated field has null points in irradiance over the phase wavefronts that are being estimated by a

wavefront sensor. At these points of zero irradiance field estimation issues arise in other wavefront sensing technologies [14]. For the SRI, there may not be any beacon light over a given subaperture, but the reference beam will have a fraction of the incoming aperture averaged intensity. Therefore the local phase is directly calculated as

$$\phi = \tan^{-1} \left(\frac{\mathbf{I}_4 - \mathbf{I}_2}{\mathbf{I}_1 - \mathbf{I}_3} \right) = \tan^{-1} \left(\frac{\mathbf{I}_{ref} - \mathbf{I}_{ref}}{\mathbf{I}_{ref} - \mathbf{I}_{ref}} \right) = \tan^{-1} \left(\frac{\mathbf{0}}{\mathbf{0}} \right) = \mathbf{0} \quad (2.22)$$

In this sense, the SRI is seen to be nearly immune to scintillation; however issues still arise in coupling light into the reference fiber when these conditions exist. To minimize coupling inefficiencies, an effective tilt tracking and correction system is essential when using an SRI. Previous research also investigated using doped reference fibers to achieve an optical gain for the reference beam path. Previous research by Rhoadarmer found that just enough gain to overcome sensor readout and quantization noise is ideal [35], but in practice this is not often implemented. This research seeks to exploit the benefits of the SRI with respect to scintillation in conjunction with a novel wavefront reconstruction technique, discussed later in Sec. 2.3.

2.1.3 *Wavefront Reconstruction.*

It is often necessary to further process the WFS outputs to achieve an unwrapped wavefront estimate. This process is called wavefront reconstruction. For the SRI, WFS phase outputs are first sheared into slope space. Other WFS designs typically directly output wavefront gradients. As slopes, each measurement point is related to the others through a set of linear equations - called the geometry matrix. This system of equations is then solved to find the continuous phase wavefront that minimizes the squared error of the original system of equations. The following subsections describe this process in detail.

2.1.3.1 Linear Algebra.

The problem of relating wavefront gradient measurements to unwrapped phases can be written as,

$$Ax = b, \quad (2.23)$$

where b is the measured gradients in column vector form of length m , x is an n -length column vector of the unwrapped phases being estimated, and A is a geometry matrix relating the two of size $m \times n$. The specific form of A will be discussed in Sec. 2.1.3.2, but it is a known system parameter. The process of solving for x varies depending on the specific properties of A . If $m = n$ and A is full rank, then the solution is straight forward as:

$$\begin{aligned} A^{-1}Ax &= A^{-1}b \\ x &= A^{-1}b. \end{aligned} \quad (2.24)$$

However, in AO this is rarely the case. Instead, there are traditionally more measurements than phase points being estimated ($m > n$). This set of linear equations is overdetermined, requiring an approach to reduce the parameter space to a best fit solution. Premultiplying by A^T , $(A^T A)$ becomes invertible, giving a best fit solution in terms of the minimized squared error for x [40]:

$$\begin{aligned} A^T A \hat{x} &= A^T b \\ (A^T A)^{-1} (A^T A) \hat{x} &= (A^T A)^{-1} A^T b \\ \hat{x} &= (A^T A)^{-1} A^T b \\ \hat{x} &= A^\dagger b \end{aligned} \quad (2.25)$$

This is the basic process which is used in the following subsections to estimate wavefront phase from gradient measurements from the WFS. Other methods exist for solving a system of linear equations such as this; however, the Moore–Penrose pseudoinverse (often referred to as the least squares pseudoinverse) is the most commonly used algorithm.

2.1.3.2 Zonal Reconstruction.

Zonal reconstruction uses a simple relative relationship between measured slopes and the phase estimation points. This relationship is captured by the Geometry matrix, of which there are two predominant types depending on the way in which a particular WFS senses wavefront gradients. The Fried geometry is typically associated with the Shack-Hartmann WFS, while the Hudgin geometry is used with the lateral shearing interferometer (LSI) and SRI.

Wavefront sensors implementing the Fried geometry sense wavefront slopes at the center of each subaperture and relate those slopes to phase estimation points at the corners of each subaperture through Eq. (2.26) and (2.27) [12]. Figure 2.7 shows a 2×2 subaperture array in the Fried geometry.

$$(s_{x-Fried})_{m,n} = \frac{1}{2}(\phi_{m,n+1} + \phi_{m+1,n+1}) - \frac{1}{2}(\phi_{m,n} + \phi_{m+1,n}) \quad (2.26)$$

$$(s_{y-Fried})_{m,n} = \frac{1}{2}(\phi_{m+1,n} + \phi_{m+1,n+1}) - \frac{1}{2}(\phi_{m,n} + \phi_{m,n+1}) \quad (2.27)$$

In this geometry, there are two slope measurements per subaperture, creating $2Q$ equations for P phase estimation points. Relating this to the discussion in Sec. 2.1.3.1, this system of linear equations can be written as

$$G_F \phi = \begin{bmatrix} s_{x-Fried} \\ s_{y-Fried} \end{bmatrix}. \quad (2.28)$$

Alternatively, wavefront sensors implementing the Hudgin geometry estimate phases at the center of subapertures based on gradient measurements between adjacent subapertures [21]. Figure 2.8 demonstrates a 2×2 subaperture wavefront system. The mathematical relationship for this geometry is more simplistic than the Fried geometry as,

$$(s_{x-Hudgin})_{m,n} = \phi_{m,n+1} - \phi_{m,n}, \quad (2.29)$$

$$(s_{y-Hudgin})_{m,n} = \phi_{m+1,n} - \phi_{m,n}. \quad (2.30)$$

Similarly to the Fried geometry, this creates $2Q$ equations for P phase estimations, creating the system of linear equations:

$$G_H \phi = \begin{bmatrix} s_{x-Hudgin} \\ s_{y-Hudgin} \end{bmatrix}. \quad (2.31)$$

Both Eq. (2.28) and (2.31) can be solved as in Sec. 2.1.3.1 by:

$$\hat{\phi} = G^\dagger s, \quad (2.32)$$

where G and s are the appropriate geometry matrix and slopes from above.

Further, G^\dagger is usually precomputed for the given wavefront sensing geometry being implemented. This eliminates the need to compute the pseudoinverse at each frame. The resulting matrix is called the reconstruction matrix,

$$R = G^\dagger. \quad (2.33)$$

This poses the general least squares wavefront reconstruction problem:

$$\hat{\phi} = Rs. \quad (2.34)$$

2.1.4 Wavefront Correction.

The process of correcting the aberrated field inputs is heavily driven by the application of interest. Techniques exist for correction of both field amplitude and phase [2, 7, 36]; however, only phase compensation is discussed further here. Traditional AO uses the methods described in the previous sections to estimate the phase wavefronts and eliminate any estimated aberrations. Figure 2.9 depicts the physical process of phase conjugation. With an accurate estimation of the aberrated input, a conjugate shape is applied to the surface of a wavefront corrector such that when the light reflects, the wavefront is near flat. As mentioned previously, the low order aberrations of tilt are often corrected separately from the higher order aberrations using a combination of deformable mirror and FSM [25, 41].

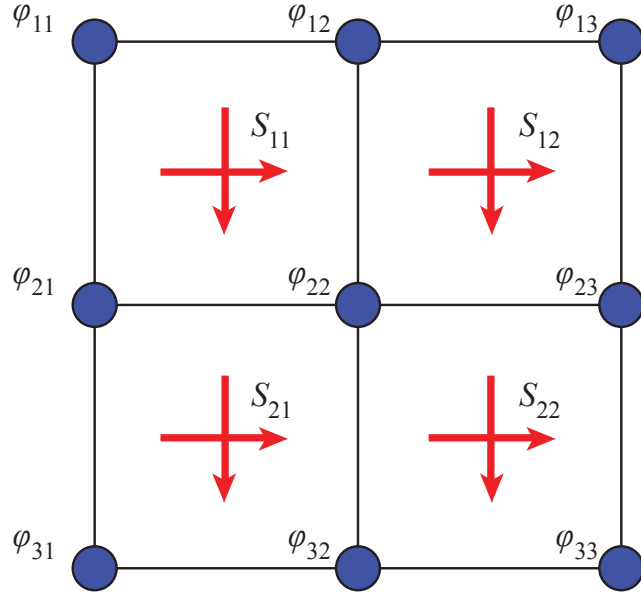


Figure 2.7: The Fried Geometry. Slopes are measured at the center of the subaperture and are related to the phases at each corner. Slope vectors shown here include both x and y components for each subaperture.

There are a number of kinds of wavefront correction devices that lend to specific applications [41]. This research uses a two inch diameter Optics In Motion FSM [3] and 12×12 actuator Boston Micromachines Micro-Electro-Mechanical System (MEMS) DM [1].

2.1.5 AO Control.

To implement a practical AO system, some form of control scheme is necessary to derive useful commands to the wavefront correction device(s) based on the estimated input aberrations [25, 41]. In practice, most AO systems rely on closed-loop control for the increased robustness when integrating complex beam control systems. Figure 2.10 shows a high-level control diagram for a tracking system. An aberrated beam entering the AO system will have some time-varying wavefront tilt, ϕ_t . The beam first reflects off of the

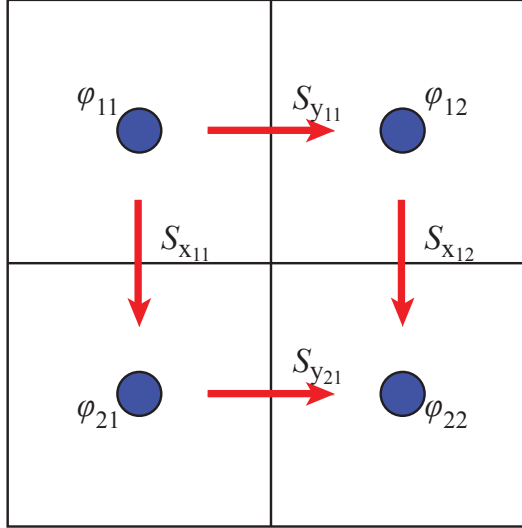


Figure 2.8: The Hudgin Geometry. Slopes are measured between adjacent subapertures, which are related to the phases at the center of each subaperture.

FSM, which leaves the beam with some residual tilt error, ϕ_{t-res} (near zero for a good control system in steady-state operation). The residual tilt error is sensed and estimated by the tracker. The estimated error is then fed into a control law to calculate the next set of adjustments to the FSM – with the ultimate goal of driving the sensed error to zero. For the AO system used in this research, a first-order linear filter of the form,

$$c_k = \alpha e_{k-1} + \beta c_{k-1}, \quad (2.35)$$

is implemented in both the tracking and higher-order control systems. In Eq. (2.35), c_k is the controller output at time step k , e_k is the sensed error at time step k , α adjusts the DC-gain, and β is a servo leakage factor. In a pure integrator setup, $\beta = 1$, but slightly lowering this value decreases sensitivity to any unsensed modes or misregistration errors.

Following the control law, a digital-to-analog converter (DAC) takes the digitized controller calculations and converts them to a usable analog voltage. This is typically

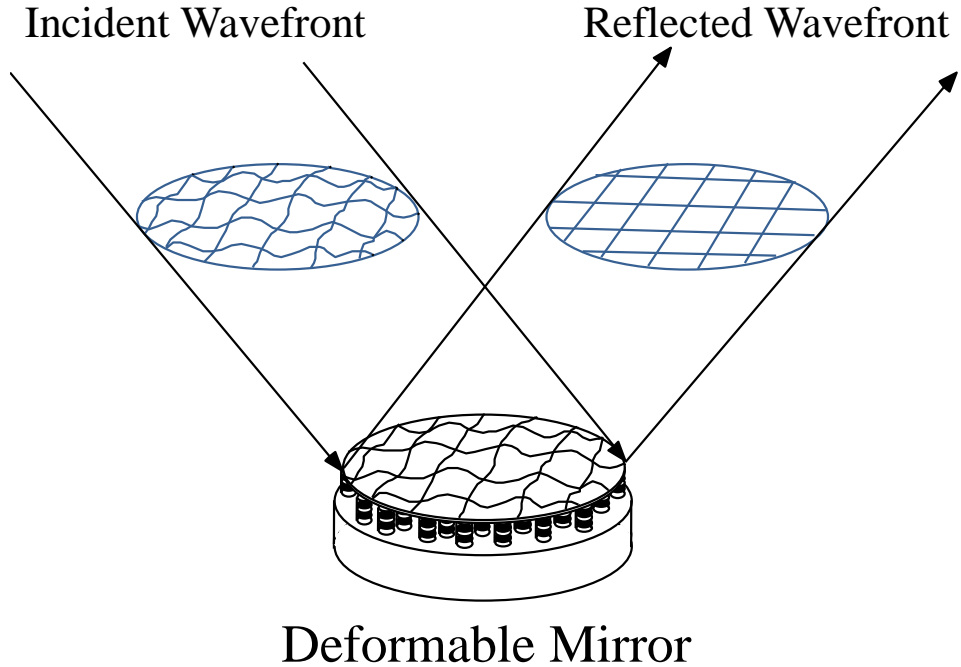


Figure 2.9: Wavefront phase conjugation using a deformable mirror.

buffered and/or amplified prior to being sent to the wavefront corrector. The FSM being used in this research implements its own internal closed-loop controller to maintain the mirror position to the analog position commands [3]. Based on the position of the FSM with respect to the optical axis, a tilt is imparted to the incoming beam, and the process repeats for each frame in time.

2.1.6 Metrics of Performance.

The holy grail of almost any optical system design is to achieve diffraction limited imaging performance for the application at hand. For this to be the case, there must be zero wavefront aberrations throughout the optical system - including the imaging path. With this in mind, the goal of AO is to remove any observable wavefront aberrations from the light of interest before reaching the science sensors or target. In AO, the primary measure

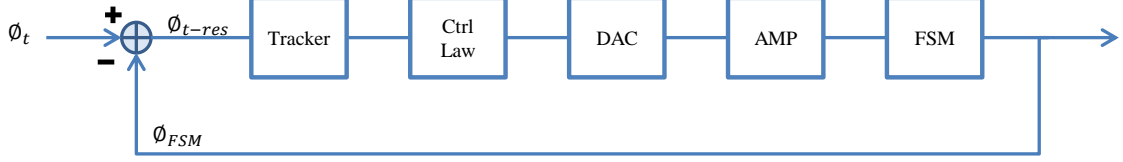


Figure 2.10: High-level control scheme for a tilt compensation system.

of correction performance is Strehl ratio. Strehl ratio is defined as [38]

$$\mathcal{S} = \frac{\int_{-\infty}^{\infty} \int_{-\infty}^{\infty} \mathcal{H}(f_x, f_y) df_x df_y}{\int_{-\infty}^{\infty} \int_{-\infty}^{\infty} H_{dl}(f_x, f_y) df_x df_y}, \quad (2.36)$$

where $\mathcal{H}(f_x, f_y)$ is the aberrated optical transfer function (OTF) [18] and $H_{dl}(f_x, f_y)$ is the diffraction limited OTF. Both of these OTF's are in terms of their spatial frequencies f_x and f_y . There are several approximations to this form that better suit various applications or measurement techniques [25, 38]. For this research field-estimated Strehl is used.

As the name suggests, field estimated Strehl takes a given field and computes an approximate Strehl without the need to propagate to a focal plane. This is often useful for efficient numerical simulations or direct Strehl estimation from WFS reconstructions.

It is given by

$$\mathcal{S} = \frac{\left| \int \int U(x, y) dx dy \right|^2}{A \int \int |U(x, y)|^2 dx dy}, \quad (2.37)$$

where $U(x, y)$ is the field within an aperture of area A . For the simulations to follow, Eq. (2.37) is discretized to the form

$$\mathcal{S} = \frac{\text{mean} [U(x, y)]^2}{\text{mean} [|U(x, y)|^2]}. \quad (2.38)$$

For hardware performance evaluation, field estimated Strehl is subject to the accuracy of the wavefront reconstruction. Therefore, when evaluating the effect of different reconstructors on AO performance in hardware, field estimated Strehl is not a good metric. An alternative

is to use either the tracking camera measurements or a separate, higher resolution, science camera to compute $\mathcal{H}(f_x, f_y)$ from the sensed irradiance point spread functions.

2.2 Scintillation and Adaptive Optics

In electromagnetics, when a field interferes with itself, areas of both constructive and destructive interference result. This is considered a scintillated field [48]. Figures 2.11 and 2.12 show the irradiance of a point source beacon propagated through both weak turbulence and strong turbulence, respectively. In each case, $D/r_0 \approx 2$ and $\lambda = 1.55\mu\text{m}$, but there are key differences between the two that should be highlighted:

Weak Turbulence Example

- $C_n^2 = 5 \times 10^{-15}$, $L = 1\text{km}$
- $\sigma_\chi^2 = 0.01$
- Smooth phase function
- Relatively evenly spread irradiance

Strong Turbulence Example

- $C_n^2 = 2.2 \times 10^{-17}$, $L = 244\text{km}$
- $\sigma_\chi^2 = 1.06$
- Phase function contains sharp cuts
- Scintillated irradiance with both peaks and areas of near zero power.

When describing a given optical path through the atmosphere, weak atmospheric turbulence generally implies that any transmitted light will only accumulate a randomized phase as a result of any refractive or diffractive effects. Figure 2.13 shows light being spherically emitted from a star that is roughly planar upon reaching Earth's atmosphere. However, once these planar wavefronts propagate through the turbulent atmosphere, the wavefronts become aberrated. Strong atmospheric turbulence generally refers to an optical path that causes not only phase accumulation but also interference effects. For this to happen, the beam accumulates a phase aberration early in the optical path. With further

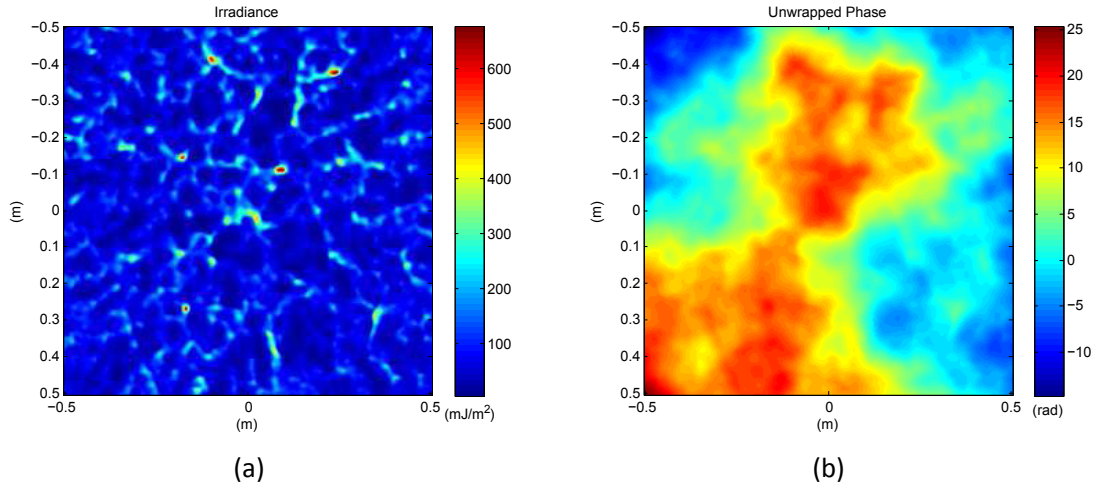


Figure 2.11: Received point source irradiance(a) and phase(b) propagated through weak turbulence.

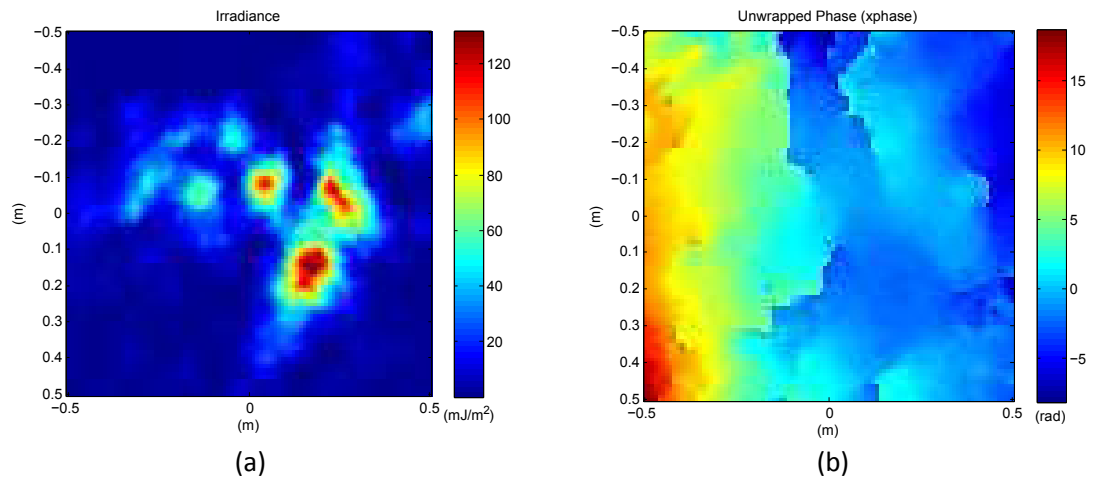


Figure 2.12: Received point source irradiance(a) and phase(b) propagated through strong turbulence.

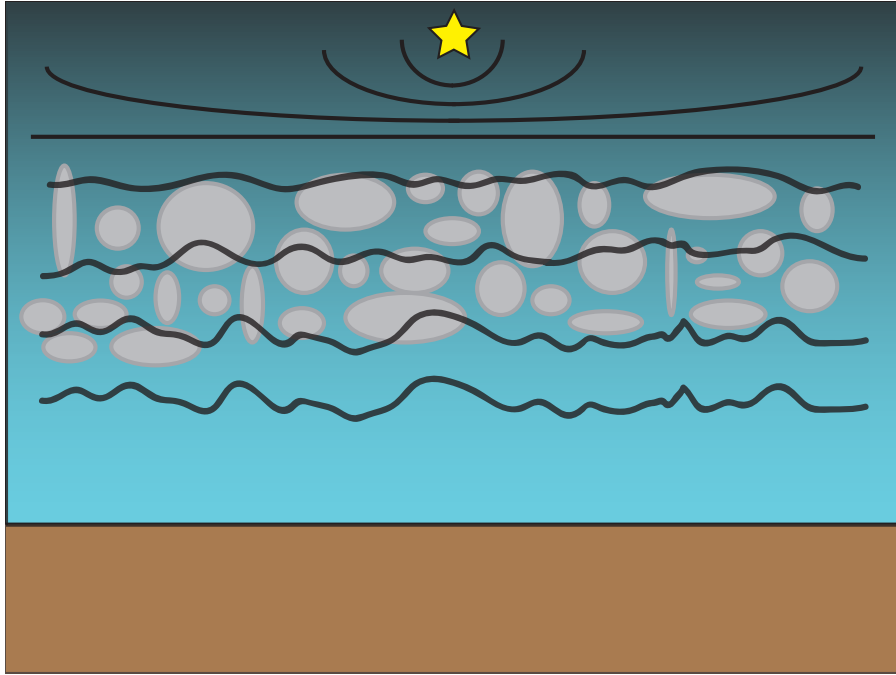


Figure 2.13: Effects of the randomized atmosphere on planar phase wavefronts.

propagation the aberrated wavefronts begin to constructively and destructively interfere - causing scintillation in the received light.

Unfortunately for AO, scintillation presents a unique set of problems with respect to phase conjugation. Fried wrote the first significant publication about scintillation's effect on the corresponding phase function [13], and he found that in areas of no light within the field a new phase component forms. Such points are called branch points. Figure 2.14 shows an idealized field that has a single branch point at the center. At the branch point there is zero amplitude, and the phase goes undefined. To make the field continuous in a modulo-one wave sense, a rotational phase emanates outward from the branch point, producing the corkscrew shape. Expanding to the general case, Fried showed that all branch points create a rotational phase field which is in addition to the generally associated irrotational wavefront aberrations from propagations through the turbulent atmosphere [13]. This can

be written simply as

$$\phi = \phi_{irr} + \phi_{rot}, \quad (2.39)$$

where ϕ_{rot} is the rotational component of the phase due to branch point effects and ϕ_{irr} is the irrotational component typically associated with atmospheric optical propagations. Note that in weak turbulence, $\phi_{rot} = 0$ because there are generally no branch point effects present.

As seen in the theoretical branch point of Fig. 2.14, the rotational phase is defined over a one wave region. This, combined with the rotational nature, requires a sharp cut emanating outward from the branch point along the wrapping edge of the one wave window. This is called a branch cut and can be seen in parts of the reconstructed phase in Fig. 2.12. Branch cuts always link pairs of branch points or travel from one branch point to outside the pupil region. The rotational phases are defined on an arbitrary one wave region, and the 2π window can be shifted without changing the modulo- 2π congruence of the wavefront. However, doing so moves any branch cuts. For example, the rotational phase of Fig. 2.14 is windowed between $-\pi$ to π . If the window is changed to 0 to 2π , the wrapping boundary would move to the opposite side of the corkscrew, and the branch cut would shift sides of the field. Note that shifting this window by integer multiples of 2π give equivalent placements of the branch cuts. Likewise, if the wrapping window is kept fixed, a uniform piston added to the entire field has the same effect [31,45]. This latter technique is preferred for this research simply due to computational efficiency and can be written as

$$\phi'_{rot} = \mathcal{W}[\phi_{rot} + h], \quad (2.40)$$

where ϕ'_{rot} is still modulo- 2π equivalent to ϕ_{rot} . Figure 2.15 gives a graphical example of this process.

Unfortunately for most AO, the wavefront corrector used is a continuous face-sheet design. These correctors will inevitably have a fitting error along any branch cuts in the

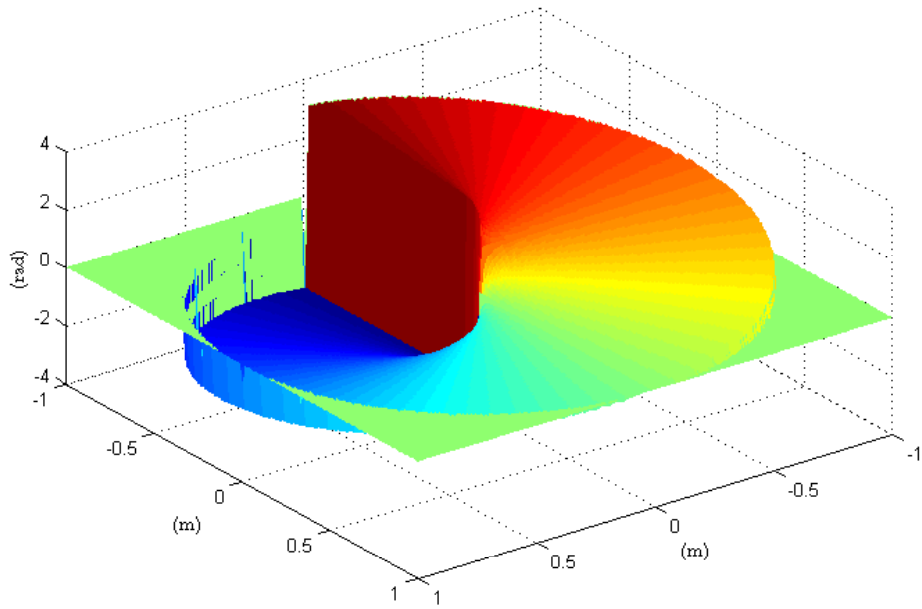


Figure 2.14: Theoretical rotational phase function surrounding a centered branch point in a propagated field.

field being conjugated. The following section poses a strategy to minimize the impact of branch cut fitting errors from the wavefront corrector.

2.3 Wavefront Reconstruction in Strong Turbulence

As described in Sec. 2.1.3, raw WFS measurements usually need reconstruction prior to correction. Herein lies a major problem for traditional AO techniques when branch points are present in the observed field. Any reconstruction matrix calculated using the least squares pseudoinverse from Eq. (2.25) cannot reconstruct a rotational component [13]. This is not a function of the particular WFS/DM geometry chosen – it is instead a behavior of the Moore-Penrose pseudoinverse. Figure 2.16 demonstrates this behavior.

Fortunately, this is not a dead end. There are actually a number of algorithms one can use to recover ϕ_{rot} . Pellizzari provides the most complete comparison to date with a focus

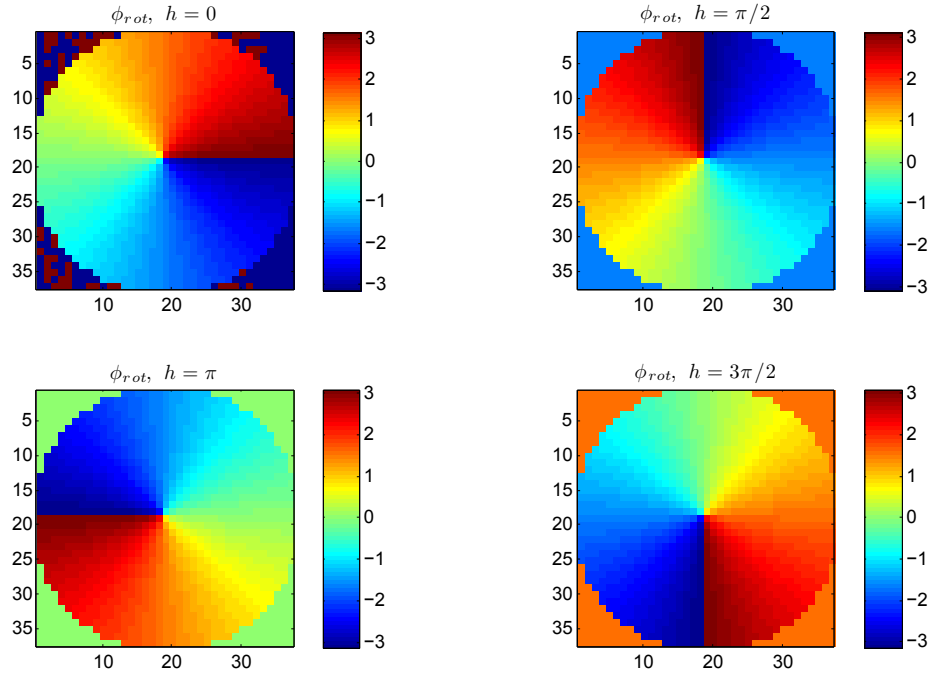


Figure 2.15: Effects of adding a uniform piston, h , to the rotational field while maintaining a fixed wrapping window. Modulo- 2π congruence is maintained, but the branch cut moves as h changes.

on the AO application [31]. Of the many algorithms from a range of science applications, the primary constraint that must be considered for use in AO is computational efficiency. The wavefront must be reconstructed in real-time at the frame rate of the WFS - often in the kilo-frames per second. Pellizzari used this to narrow down his evaluation to fifteen reconstructor options for which he did a more thorough comparison. The research that follows builds from his conclusions. In the subsections below, the most promising real-time branch point-tolerant wavefront reconstructors are described.

2.3.1 Post-Processing Congruence Operation Reconstruction.

The most promising class of algorithms is based on a post-processing congruence operation (PCO) to find and add back in the rotational portion of the field [31, 45]. This

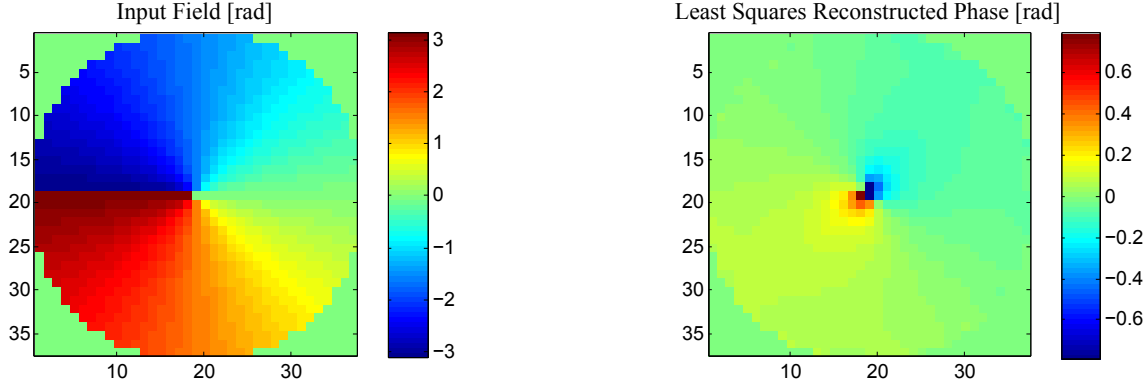


Figure 2.16: Applying a least squares reconstructor to a rotational field.

research chose the SRI because it directly senses the wavefront phase - including any rotational components present. We can thus formulate the problem in terms of Eq. (2.39) and the PCO technique as

$$\hat{\boldsymbol{\phi}}_{irr} = \boldsymbol{\phi}_{LS} = R_{LS} \Gamma(\boldsymbol{\phi}_{SRI}), \quad \text{and} \quad (2.41)$$

$$\hat{\boldsymbol{\phi}}_{rot} = \mathcal{W}[\boldsymbol{\phi}_{SRI} - \boldsymbol{\phi}_{irr}],$$

where $\boldsymbol{\phi}_{SRI}$ is the SRI's raw phase measurement and the $\Gamma(\boldsymbol{\phi})$ operator finds the x and y gradients of $\boldsymbol{\phi}$, consistent with the reconstructor geometry being used [13, 15, 31, 45]. Substituting Eq. (2.41) into Eq. (2.39) gives

$$\hat{\boldsymbol{\phi}}_{PCO} = \boldsymbol{\phi}_{LS} + \mathcal{W}[\boldsymbol{\phi}_{SRI} - \boldsymbol{\phi}_{LS}]. \quad (2.42)$$

This process maintains the traditional least squares phase reconstruction technique for the irrotational phase component and finds the modulo- 2π equivalent rotational phase out of the original measurement. This process adds only a very small computational overhead to gain the rotational component reconstruction.

There is further room for improvement on the basic PCO process. As discussed in Sec. 2.2, the branch cut locations can be varied by applying a piston to the rotational field

prior to wrapping Eq. (2.40). The subsections that follow take the general PCO algorithm and attempt to optimize the particular realization of rotational phase with respect to the branch cut locations by seeking an optimal piston addition, h .

To compare realizations of rotational phase, a cost function posed by Venema [45] and refined by Pellizzari [31] called intensity weighted cut length (IWCL) is used. IWCL first locates any branch cuts in a rotational field—again by shearing the raw phase to get wavefront gradients, and searching for sharp gradients. It then integrates the SRI’s estimated field irradiance from Eq. (2.21) along the estimated cuts. Results from both Venema and Pellizzari show high negative correlation between IWCL and Strehl ratio [31, 45]. This research deviates slightly from the previous IWCL implementations in not normalizing the integrated IWCL by the total field irradiance. While the normalized IWCL is useful for comparing specific test cases, there is no advantage to the additional computations in a real-time AO system.

By seeking to minimize IWCL, branch cuts are moved towards areas of minimized irradiance, thus keeping the effects of DM fitting errors along the cuts to a minimum. This is only one cost metric – others can be chosen based on the application of interest. One alternate was developed for beam projection applications, which is presented later in Sec. 4.6.

2.3.1.1 LSPV.

Least squares principle value (LSPV) was first published with respect to AO by Venema and Schmidt [46]. LSPV+ n takes the one wave range of possible h offsets, and divides it n times:

$$h_{eval} = \left[0 : \frac{2\pi}{n} : 2\pi \right]. \quad (2.43)$$

While the definition above splits h_{eval} equally across the one wave range, there are variants that do not necessarily follow this constraint. The LSPV+ n reconstruction process then

evaluates all n values of h_{eval} in terms of IWCL to determine the best ϕ_{rot} :

$$\hat{\phi}_{LSPV+n} = \phi_{LS} + \mathcal{W}[\phi_{SRI} - \phi_{LS} + h_{opt}], \quad (2.44)$$

$$h_{opt} = \operatorname{argmin}_{h_{eval}} [IWCL(\phi_{rot}(h_{eval}))]. \quad (2.45)$$

LSPV+1 and LSPV+4 were the primary algorithms investigated in this level of PCO optimization. LSPV+1 may seem like a poor choice, but with only one value of h_{eval} , there is no need to compute IWCL - giving a computational advantage. LSPV+200, or other large n , can be used to test for the true ideal h_{opt} for a given field but is not suggested for real-time implementation due to the computational requirements and diminishing marginal gains. Figure 2.17 shows one particular LSPV+4 execution. It is obvious that some values of h_{eval} are less optimal than others.

2.3.1.2 Iterative Probing.

Proposed by Pellizzari [31], this algorithm starts a narrow LSPV+5 search about the midpoint between the previous frame's $h_{opt,k-1}$ and $\langle h_{opt} \rangle$. In this case, the narrow LSPV+5 search evaluates

$$h_{eval1} = \left[\begin{array}{ccccc} -0.3 & -0.15 & 0 & 0.15 & 0.3 \end{array} \right] + \frac{h_{opt,k-1} + \langle h_{opt} \rangle}{2} \text{ waves.} \quad (2.46)$$

The calculated $h_{opt,k}$ from the above LSPV+5 search serves as a seed for a second search. The new search narrows the range of h_{eval} for a finer investigation of the IWCL parameter space about $h_{opt,k}$:

$$h_{eval1} = \left[\begin{array}{ccccc} -0.07 & -0.04 & 0 & 0.04 & 0.07 \end{array} \right] + h_{opt,k} \text{ waves.} \quad (2.47)$$

Pellizzari motivated this by showing that the IWCL-space is roughly parabolic. This iterative probing method allows for further precision with still minimal additional computational requirements.

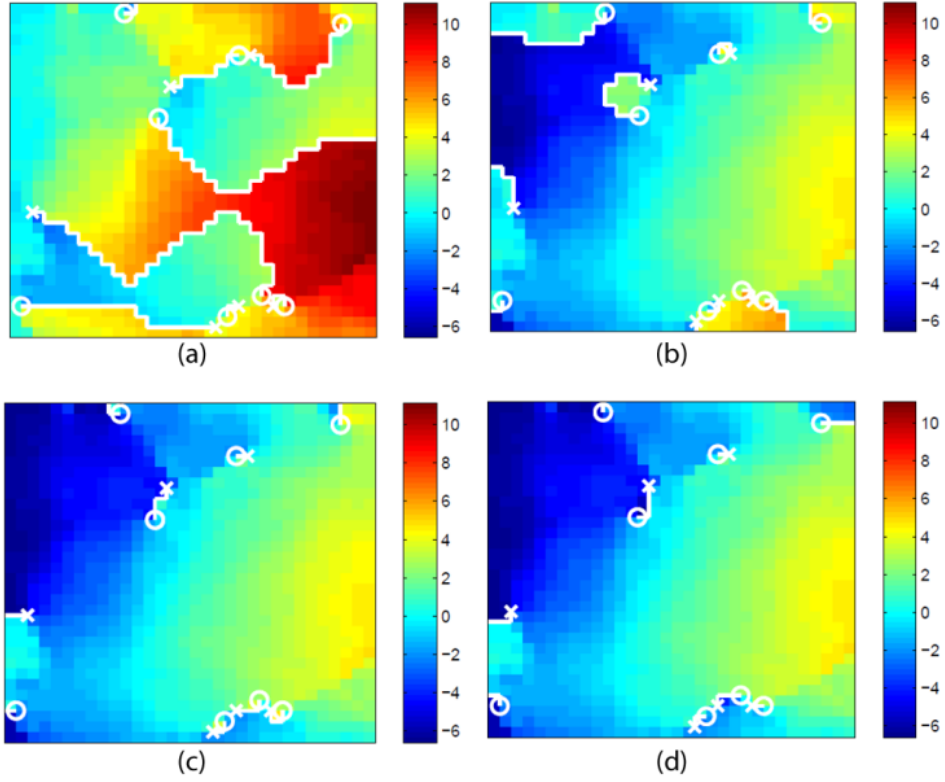


Figure 2.17: These plots depict the rotational portion of a wavefront in radians as a piston shift is applied [45]. Branch points are marked by X's and O's based on their respective charge, and branch cuts are highlighted with white. The non-unique nature of the rotational phase is highlighted by applying piston: π (a), $\pi/2$ (b), 0 (c), and $-\pi/2$ (d). Plots adapted from [45].

2.3.1.3 Histogram Search.

Also proposed by Pellizzari [31], this algorithm minimizes the area of ϕ_{rot} near the wrapping boundaries. It first calculates a histogram of the ϕ_{rot} phase values. From there, it calculates h'_{opt} as the shift required to place the minimally sized histogram bin at the nearest wrapping edge. Additionally, a narrow LSPV+3 search explores the IWCL parameter-space about h'_{opt} to arrive at the final h_{opt} .

2.3.1.4 *Brent's Method.*

The final PCO algorithm posed by Pellizzari utilizes what is known as a Brent's Method [33]. Unlike the iterative probing algorithms above, this type of search algorithm minimizes the required evaluations of the cost function for the optimization problem at hand. For this, it means fewer evaluations of IWCL through a golden ratio search of the h parameter-space. Knowing that the IWCL parameter-space is roughly parabolic, this algorithm recursively refines a parabolic fit by adjusting h . Each parabolic fit uses four data points, from which the search algorithm divides that search range in half. Successive searches maintain a ratio between cost function evaluation inputs such that previous IWCL evaluations are reused as the search narrows.

III. High-Fidelity Simulation Development

This chapter highlights the development of a Matlab model of AFIT’s own AO testbed. From the start of development, this was intended to be a high-realism wave-optics based simulation of the true system dynamics. The following sections highlight the development decisions, lessons learned, and configuration capabilities for the simulation model.

The simulations were developed in the Matlab programming environment. As this is a discrete numerical model, careful consideration was given to adequate spatial sampling of the electromagnetic fields involved. Although this discussion does not cover the theory behind numerical simulation of wave-optics, this information can be found in Schmidt [38]. Additionally, Matlab toolboxes, WaveProp and AOTools, were used to augment the methods proposed by Schmidt. These toolboxes were developed by the Optical Sciences Company (tOSC). Much self-authored functionality and integration code was developed for this research and is described in the sections that follow.

3.1 AFIT Adaptive Optics System

AFIT’s AO system testbed was built as a multi-purpose platform on which to give a hands-on experience for Air Force students being introduced to AO. As it has evolved, it has become an extremely capable and configurable platform for advanced AO research [37]. Despite this, having a simulation model on which to conduct initial research, where many variables of experimental work are idealized, creates a powerful time and money saving tool. The following subsections introduce the physical system and how it was translated into the computer model.

3.1.1 *Hardware Specifications and Setup.*

Built by SAIC, AFIT’s AO system consists of two independent control systems. As described in Sec. 2.1.2, a tracking system handles the low order tilt wavefront aberrations,

while a separate high-order system senses and corrects the remaining wavefront errors. Figure 3.1 shows the optical layout of the AO system which can be fed by anything that relays to an entrance pupil at the FSM. As is currently setup, the beam diameter at the FSM is 14mm before being reduced by a factor of three in a 4-*f* relay to the DM. From then on, the beam remains at 4.67mm and is relayed once more to the sensor entrance pupil which precedes the Shack-Hartman WFS beam-splitter. This size gives ten DM actuators across the beam as shown in Fig. 3.2. A border of actuators remain that are slaved to the actively driven ‘master’ actuators. Slaving unsensed actuators minimizes influence of adjacent actuators at the beam edges on the actively driven actuators [43]. For this research, the Shack-Hartmann WFS is being completely bypassed and going unused. Instead, the higher-order WFS is a 19×19 subaperture spatial SRI operating at 1.9Kfps with one frame of latency from sensor exposure to DM commands out. The tracking sensor has a field of view of 1.8mrad over a 32×32 sensed pixel array operating at 4.76Kfps, again with roughly one frame of delay from exposure to FSM command out. Note that this field of view is referenced to the AO system entrance pupil, not the demagnified beam entering the actual tracker.

This spatially-oversampled WFS-DM geometry is important in properly reconstructing the wavefront with a phase-only WFS when there is potential for large phase differences between WFS subapertures [6]. Such large phase differences are a natural consequence of branch cuts within the field. Therefore, a high-resolution wavefront reconstruction is formed from the 19×19 SRI measurements, which is then downsampled to the DM resolution prior to the control-law calculations. It is important when downsampling only to include phase estimates within the active aperture, otherwise the outer edge of downsampled points will always be artificially biased towards zero.

Simulating the hardware system allows for a few simplifications. First of all, there is no need to simulate any optical relays of the entrance pupil. Instead, all phase corrections

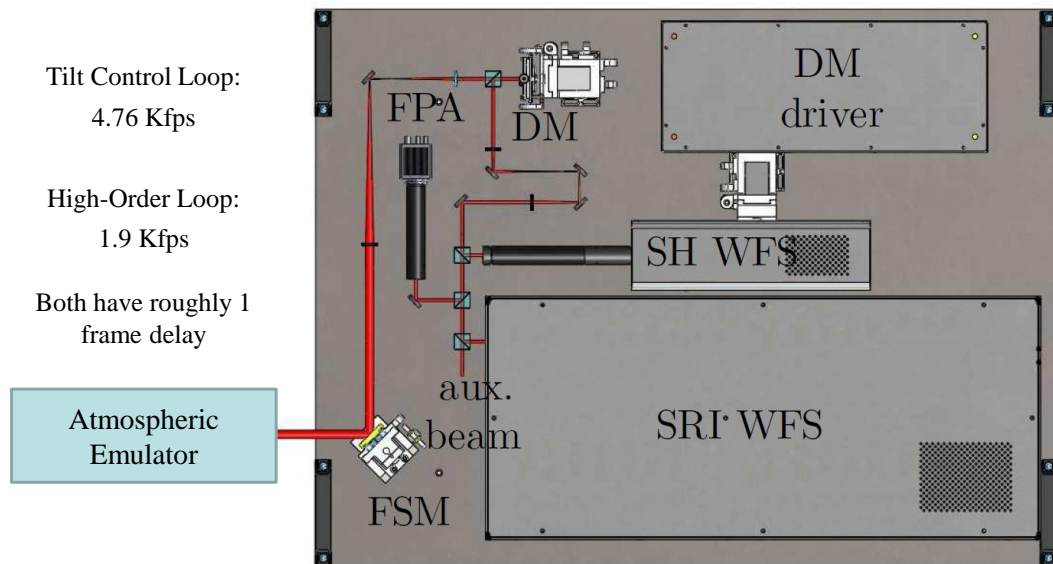


Figure 3.1: Layout of AFIT's AO system testbed.

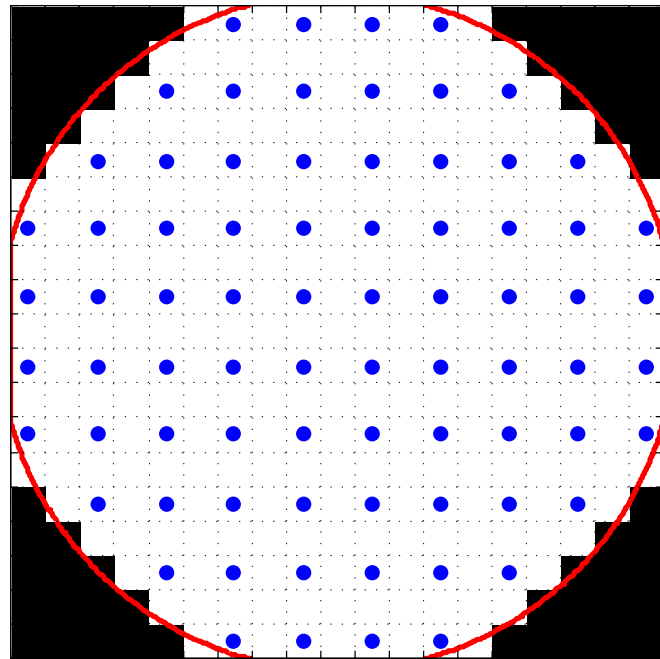


Figure 3.2: Geometry of SRI subapertures (dotted squares) to master DM actuators (blue dots) the beam extent is shown in red.

are performed on the same field, which is then appropriately scaled in irradiance before being sensed by the tracker and SRI. Of course, this assumes a perfectly aligned and zero aberration optical system; however, if one wanted to add either effect, it would be a simple addition.

In simulation, a one meter telescope collects light from the optical propagations. This is not as critical as D/r_0 is, where D is the entrance aperture diameter. As discussed before, the ratio of wavefront corrector size to Fried's parameter, r_0 , is an important consideration when designing a system. For this simulation work, any atmospheric conditions can be generated, leaving the choice of entrance aperture size somewhat arbitrary. The entrance telescope is simulated to have a focal length at the simulated target distance for each scenario, giving a collimated output beam to the AO system.

The telescope also demagnifies the one meter entrance pupil to a 4.67mm exit pupil. This design decision ignores the one-third demagnification from the FSM to DM in the physical system but increases the simulation simplicity. Due to the changed angular magnification at the simulated FSM, the only change between the simulations and physical system is the final gain coefficient between the tracker controller to the analog FSM voltages. Since no inertial effects of the FSM are simulated, this gain discrepancy has no effect on the fidelity of results. To justify excluding simulating inertial effects of the FSM, a comparison between the FSM command frequency spectra (at the highest Greenwood frequency tested) and the physical FSM's measured frequency response showed only a small content approaching the FSM's roll-off frequency.

With the optical system design handled, consideration of the separate control systems must be paid. Often in computer simulations of AO systems, the tracking system and high-order system operate at integer frequency multiples of one another (i.e. Tracking at 4Kfps, High-order at 2Kfps); however, this is not often the case for physical systems. This is an issue when calculating the optical fields that feed the system. As these are computationally

very expensive to generate, a minimum number of frames should be sought. The solution used in this research was to calculate separate lists of sampling times for each control system based on their respective sampling rates. With those, a unique merge of the two lists is performed, while maintaining a table that links each point in time to which sensor(s) is active. This resulting list is not uniformly spaced in time, but it does not have to be. Knowing the turbulence wind speeds and point in time, WaveProp is able to generate the propagated fields without issues. The listing below gives pseudo code through this process for additional clarification.

```

1 % Load propagated fields
2 % Setup sensors and correctors
3
4 for currFrame = 1:numFrames
5     % Apply simulated telescope
6     % Apply last FSM and DM corrections
7
8     if SRI active
9         % Detect, reconstruct, downsample, control law, filter
10    end
11
12    if TRK active
13        % Detect, threshold, centroid, control law
14    end
15
16    % Calculate Strehl
17
18 end

```

With the above system coded up, initial simulations began. Unfortunately, the first set of Strehl plots looked like the left subplot of Fig. 3.3. As the figure shows, initially the AO system is completely off, and the Strehl is roughly zero. The tracking system turns on 0.01s, and the Strehl picks up to roughly 0.1. At 0.02s, the high-order system turns on, leading to a good initial improvement, but the system quickly goes unstable. Upon investigation of the DM commands, it was obvious that tilt was dominating the DM corrections.

While not apparently an issue in the previous work by Pellizzari where the separate control systems operated at the same frequencies, here the higher-order and tilt control systems create a condition where they fight each other. As there is always going to be a slight residual correction error from the tracking system, the SRI detects this and tries to compensate, although at a slower sampling rate. The faster tracking system will have time to sense and correct for the same residual that the higher-order system is still processing.

When the control loop gains are high enough, this behavior can quickly overwhelm the limited stroke of the DM and even drive the whole AO system unstable.

The solution is simple: ensure there are no common correction modes between any control loops. In this case, project out tilt from the higher-order system. In traditional AO, it is common to augment the traditional least-squares reconstructor matrix with a tilt-removal operation, such that the reconstructed wavefront has no tilt components. The process for this is shown in the code below:

```
1 %% Remove Z-Tilt:
2
3 % Generate arbitrary orthogonal tilted wavefronts:
4 [xt,yt] = meshgrid(1:nDMacts);
5 % Zero-mean:
6 xt = (xt - mean(mean(xt)));
7 yt = (yt - mean(mean(yt)));
8 % Only consider the active aperture:
9 xt = xt(activeMask == 1);
10 yt = yt(activeMask == 1);
11 % Transform from 2D-space into Reconstructor-space
12 % and normalize the tilted wavefronts:
13 XZ = xt*xt'/(xt'*xt);
14 YZ = yt*yt'/(yt'*yt);
15 % Create the Tilt-Removal Operator Matrix:
16 P = eye(sum(activeMask(:))) - XZ - YZ;
17
18 % Combine to form a tilt-removed Reconstructor:
19 R_tr = P * R;
```

Unfortunately, with the PCO-based reconstruction techniques, this process is not as simple. As outlined in the previous chapter, the PCO process is

$$\hat{\phi}_{PCO} = \phi_{LS} + \mathcal{W}[\phi_{SRI} - \phi_{LS}]. \quad (3.1)$$

However, to make $\hat{\phi}_{PCO}$ tilt-removed, two forms of least-squares reconstruction are needed:

$$\hat{\phi}_{PCO} = \phi_{LS-tr} + \mathcal{W}[\phi_{SRI} - \phi_{LS-tilt}], \quad (3.2)$$

where ϕ_{LS-tr} is a tilt-removed least-squares reconstruction while $\phi_{LS-tilt}$ retains tilt. This does indeed give a tilt-removed reconstruction, but it requires the calculation of two least-squares reconstructions rather than only one.

A better solution exists. Realizing that the control law follows the reconstruction, a design decision exists on where to calculate actuator slaving. Often, this is rolled in with the least-squares reconstructor; however, this technique will not work with the PCO calculation of ϕ_{rot} . Additionally, the slaving operation should ideally be the last calculation prior to sending the DM commands out. So a tradeoff can be made in this case: only calculate a single, tilt-included, least-squares reconstruction which gives a tilt-included PCO reconstructed waveform. Downsample the reconstruction, send it through the control law, and apply one final matrix operator which removes piston, removes tilt, and applies slaving. This is the optimal data-flow process for a PCO reconstructor; shown in Fig. 3.4. In total, this requires just two matrix multiplies – one for the least-squares reconstruction and one for the final filtering. With the tracking and higher-order control systems decoupled, performance improved greatly. This is seen in the right plot of Fig. 3.3.

3.1.2 System Radiometry.

With the simulation model framework mostly in place, focus could be turned to modeling radiometry throughout the optical system. This is crucial if noise effects are going to be accurately simulated, as photon shot noise is signal-dependent [17] and other noise sources are only meaningful in relation to the signal level.

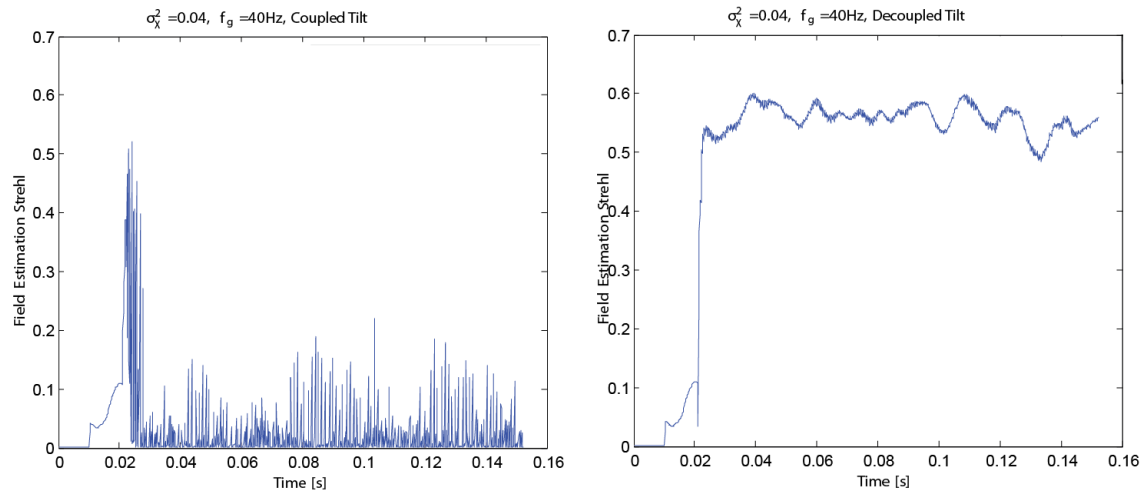


Figure 3.3: The effects of neglecting tilt decoupling on Strehl ratio. Right plot shows tilt properly decoupled over the same input wavefronts for comparison.

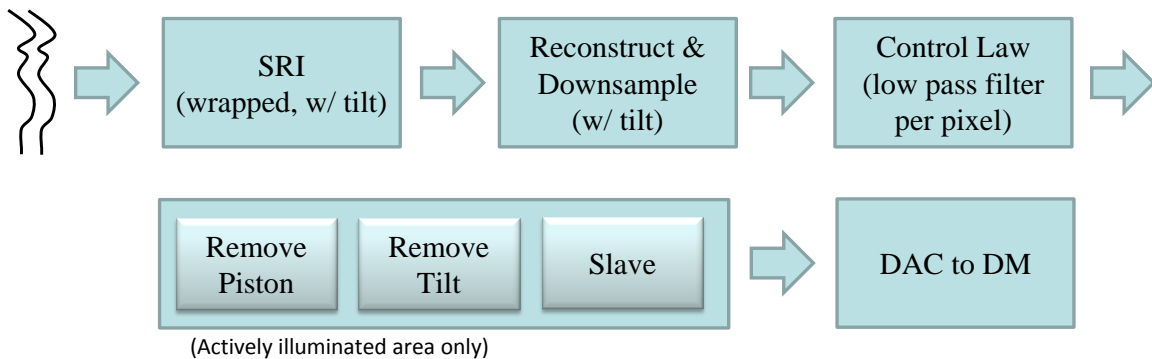


Figure 3.4: Optimal process flow for a PCO based reconstruction algorithm.

3.1.2.1 Radiometric Assumptions.

In the physical AO system, power can be varied to each signal path using polarized beam splitters preceded by adjustable half-wave-plates [37]. This requires the input light be initially filtered by a polarization analyzer. For the simulation work, no polarization effects are modeled - only the power splitting ratios. In this sense, the input light for the simulations would be equivalent to just after the initial polarization analyzer on the physical table.

A number of assumptions were made in this radiometric model:

1. No losses due to reflections.
2. No losses due to dispersion or misalignments.
3. Ideal beam splitters.

Realistically there is a small loss through the system despite the anti-reflective coatings used on all optics. Additionally, the beam splitters have a finite extinction ratio. This is relevant for the beam paths that theoretically receive no light. Realistically, the Shack-Hartmann and auxiliary beam paths receive a small percentage of the light.

Additionally, realistic sensor models were created in WaveProp based on the camera datasheets from Goodrich. For both the tracker and SRI, a Goodrich SU320-KTSW sensor is used, with the key specifications shown in Table 3.1.

3.1.2.2 Realistic SRI Reference Fiber Coupling.

Previous simulations assumed the SRI had a constant fiber coupling coefficient into its single-mode reference fiber, regardless of the input wavefront condition. This is a rough approximation for quick evaluation but is insufficient for a realistic noise analysis, determining low signal performance, and examining transient behavior before the AO system reaches steady-state.

Table 3.1: Goodrich SU320-KTSW Sensor Specifications

Resolution	$320 \times 256^{\dagger}$
Pixel Pitch	$25\mu\text{m}$
Quantum Efficiency	$>0.65^{\ddagger\ddagger}$
Full Well e ⁻	$750,000\text{e}^{-}$
RMS Read Noise	$183\text{e}^{-\ddagger\ddagger\ddagger}$

[†] Can address a smaller rectangular region of the array for increased speed.

^{††} Actual quantum efficiency at 1550nm is likely greater, but 0.65 was used for these simulations. A sensor calibration can experimentally determine this value [22].

^{†††} Based on correspondence with Goodrich technicians for a FPA gain of one.

Based on previous work by Wheeler [47], frame-by-frame fiber coupling efficiency and exit mode shape can be calculated. Using the physical optic and fiber parameters of AFIT’s SRI hardware, the single mode accepted into the fiber (LP_{01}) is back-propagated to the SRI entrance pupil. With this, the input aberrated beam is projected onto the known back-propagated LP_{01} fiber mode, giving a realistic frame-by-frame coupling coefficient. Similarly, the exiting LP_{01} fiber mode is a magnified version of the input mode, based on the specific re-collimating optics used after the output of the fiber. This output mode is scaled by the current frame’s coupling coefficient as

$$U_{fiberout}(k) = (U_{input}(k), U_{01-in}) U_{01-out}, \quad (3.3)$$

where (\cdot, \cdot) denotes an inner product, k represents the current time step, U_{input} is the input aberrated beam of the SRI reference leg at time step k , U_{01-in} is the normalized back-propagated LP_{01} mode that is coupled into the fiber, and U_{01-out} is a normalized version of the collimated fiber exit mode. This operation captures the stochastic variations in coupling efficiency, while other effects like Fresnel reflections are treated separately and deterministically. As is shown in Figs. 3.5 and 3.6, fiber coupling is particularly important

in modeling transient behavior immediately after closing the loop in strong turbulent, low signal situations.

3.1.2.3 Power Splitting.

As shot noise is dependent on the signal level at the detector and the other noise sources are only meaningful relative to the signal level, careful work had to be taken to ensure proper radiometry throughout the simulated AO system. This problem was initially approached by adjusting the power splitting between tracker and SRI to achieve roughly equivalent signal levels on each detector. For the tracker this is straight forward, but the SRI presents a challenge with the input-dependent fiber coupling. For this calibration, a low-Rytov turbulence scenario was used to determine the optimum tradeoff in power splitting. Figures 3.5 and 3.6 illustrate this tradeoff. Before the AO system is engaged, the fiber coupling is near zero. First the tilt system is engaged, giving a very slight increase in coupled light. This coupled signal must be sufficient to form the SRI wavefront estimate, otherwise the higher-order control loop may not successfully close when engaged. When the higher-order system engages, coupling immediately jumps as the DM starts correcting. This is shown in Fig. 3.5 when the fiber power becomes stronger than the signal power. However, as fiber coupling efficiency is directly correlated with Strehl ratio, stronger turbulence degrades the power coupled into the SRI reference fiber, as seen in the medium-Rytov case of Fig. 3.6. A balance must be struck between supplying enough power to initially engage the higher-order control loop while not taking too much power from the signal leg. The power splitting can thus be optimized for the expected atmospheric conditions, or as in this research, a general compromise was found that accommodates a wide range of scenarios. Figure 3.7 shows the power splitting breakdown through the AO system that was empirically determined, and as it turns out matches up closely to the physical AFIT hardware setup.

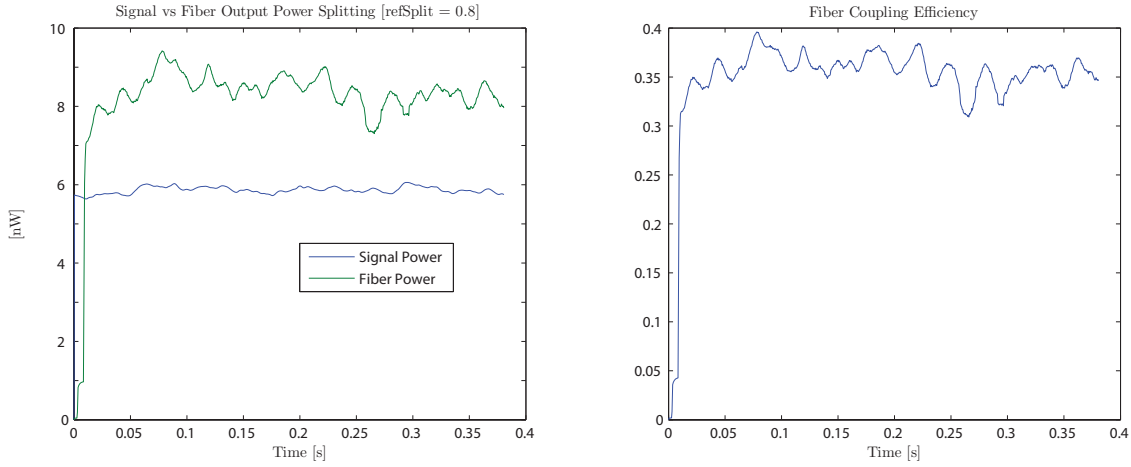


Figure 3.5: SRI reference fiber coupling as the AO system starts up. The left plot shows the power in the fields for both the signal and reference (labeled Fiber Power) legs through the SRI. The right plot calculates the fiber coupling efficiency over time. Atmospheric conditions are $f_g = 20\text{Hz}$, Rytov number = 0.04.

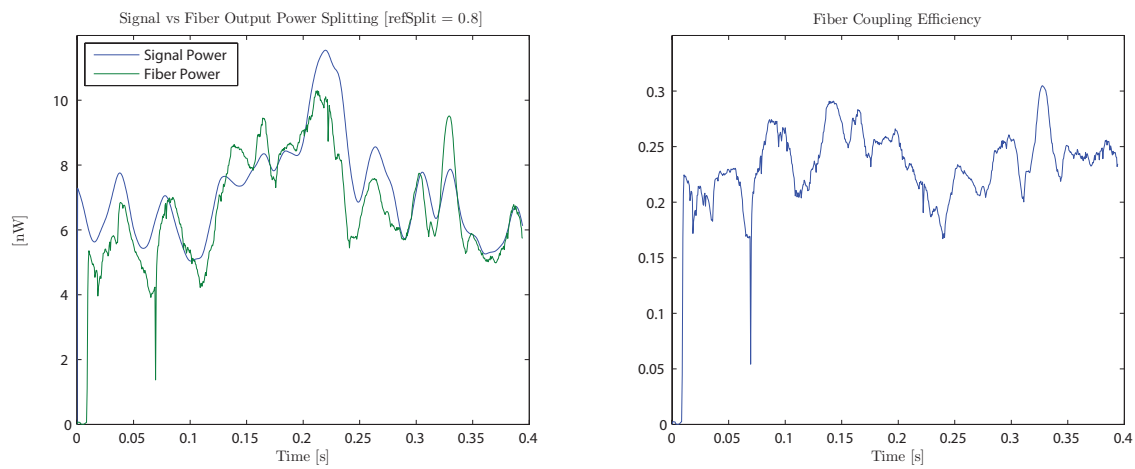


Figure 3.6: SRI power splitting between reference and signal legs on the left using a LSPV+4 reconstructor for turbulence with a Rytov number of 0.488 and Greenwood frequency of 20Hz. The resulting fiber coupling is shown on the right.

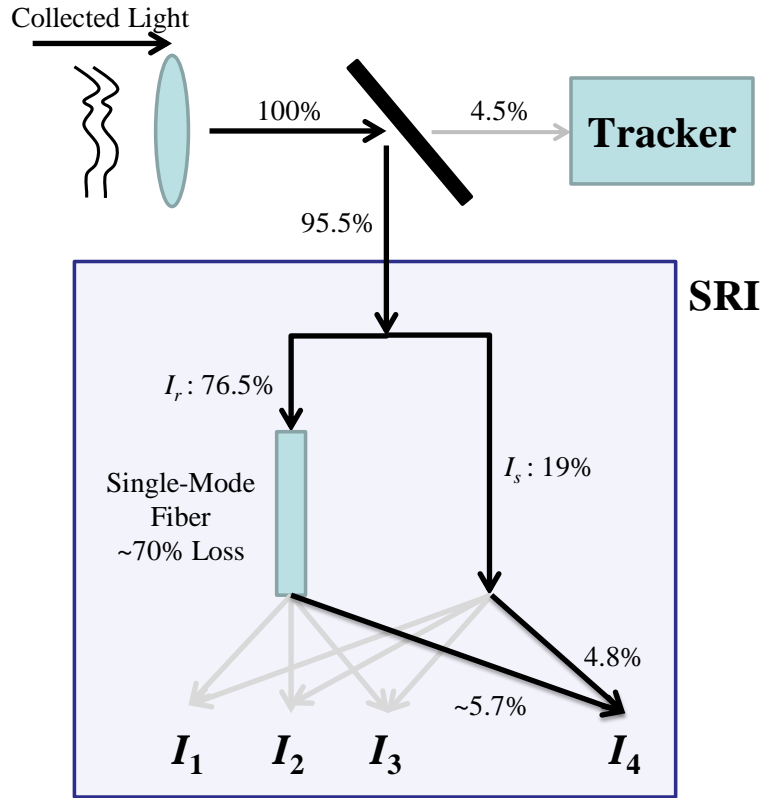


Figure 3.7: Approximate power splitting within the simulated AO system. The SRI's interferograms are represented with I_1 through I_4 . I_r and I_s are the reference and signal paths, respectively. The fiber loss will depend on the instantaneous Strehl ratio of the field entering the SRI.

3.1.3 Sensor Noise Effects.

With the system radiometry setup, focus can be turned to the noise sources. For this discussion, focus is on a single pixel of one SRI interferogram, as we are most interested in noise effects relating to the reconstruction performance. However, it should be noted that the balanced power distributions and same detector models used in the SRI and tracker yield roughly equivalent SNR's. Noise sources analyzed include photon shot noise σ_{shot}^2 , detector readout noise σ_{read}^2 , and ADC quantization noise $\sigma_{quantization}^2$ so that the total system noise is given by

$$\sigma_{sys} = \sqrt{\sigma_{shot}^2 + \sigma_{read}^2 + \sigma_{quantization}^2}. \quad (3.4)$$

Photon shot noise follows a Poisson distribution and is only a function of the signal strength. Its noise contribution to Eq. (3.4) can be expressed as [35]

$$\begin{aligned} \sigma_{shot}^2 &= \bar{K} \\ &= \frac{\eta_{qe}}{N_{bins}} \left[T_{int} \mathcal{A}_{px} \frac{(I_s + \eta_c I_r)}{2} \right] \end{aligned} \quad (3.5)$$

where \bar{K} is the mean photoelectron count for a given pixel, η_{qe} is the detector quantum efficiency, N_{bins} is the number of SRI interferograms captured simultaneously, T_{int} is the detector integration time in seconds, \mathcal{A}_{px} is the area of one pixel in square meters, η_c is the mean coupling efficiency into the single-mode fiber, and I_s and I_r are the irradiances for the signal and reference legs of the SRI, respectively. As this is an interferogram, I_s and I_r are averaged, rather than simply adding their signals.

As mentioned in Table 3.1,

$$\sigma_{read}^2 = (183e^-)^2. \quad (3.6)$$

This read noise number varies depending on the gain and calibrations used, but this gives a rough middle ground for an InGaAs camera in this class and represents one bit of digital resolution. This sensor uses a 12bit ADC to quantize the analog photocurrents. Assuming

a rounding ADC, the quantization noise can be expressed as [35]

$$\begin{aligned}\sigma_{\text{quantization}}^2 &= \frac{1}{12} \text{LSB}^2 \\ &= \frac{1}{12} (183e^-)^2,\end{aligned}\tag{3.7}$$

where there are 183 photoelectrons per least significant bit (LSB) of the 12bit ADC.

With all of the noise sources defined, the challenge becomes to define a meaningful SNR to test AO and reconstructor performance. The noise is now defined in terms of photoelectrons for an individual pixel of one interferogram. The signal will thus be defined as the average number of photoelectrons incident on one pixel over the same integration period. Making use of Fig. 3.7, roughly 5% of the entrance power reaches the pixel from both the signal and reference legs of the SRI. Since this is an interference pattern, the combined signal could range between 0-10% with a mean about 5%. Therefore, the signal estimate is 5% of the input power. Note that this decreases if Strehl performance degrades for any reason. Putting Eqs. (3.4)–(3.7) together with the previous definition of signal, SNR can be defined as

$$\text{SNR} = \frac{\bar{K}}{\sqrt{\sigma_{\text{shot}}^2 + \sigma_{\text{read}}^2 + \sigma_{\text{quantization}}^2}}\tag{3.8}$$

$$\text{SNR} = \frac{\bar{K}}{\sqrt{\bar{K} + (183e^-)^2 + \left(\frac{1}{\sqrt{12}} 183e^-\right)^2}}.\tag{3.9}$$

Using the above equation for SNR, the required input beam power can be calculated for $1.55\mu\text{m}$ light. Note that these SNR values are not in decibels. In the extreme, before the higher-order loop is closed, actual signal levels can be much lower than these estimates due to poor fiber coupling, as seen in Figs. 3.5 and 3.6. Because of this, initially closing the loop has been found to be the primary obstacle for the SRI-based AO system to overcome. Ensuring the tracking system is closed before trying to close the higher-order loop is essential in low signal conditions.

3.2 Atmospheric Propagations

While not the primary focus of this research, realistic aberrated optical inputs are needed to test the AO system over. An ideal point source beacon at a wavelength of $1.55\mu\text{m}$ was used in all cases. As mentioned before, care was taken in ensuring adequate spatial sampling of the wavefronts using methods from Schmidt [38]. WaveProp also alerts users if inadequate sampling is detected. Table 3.2 lists the spatial sampling used in this research, where σ_x^2 is the Rytov number, d/r_0 is the ratio of the DM actuator spacing to Fried's parameter, δ_{src} is the beacon source plane grid spacing, δ_{AOsys} is the receive plane grid spacing entering the simulated telescope, N Grid Points is the number of discrete spatial samples per side of the simulated field, C_n^2 is the index of refraction structure constant along the propagation path, and D_z is the propagation path length.

3.2.1 Parameter Exploration.

To fully characterize the AO system performance, a wide parameter-space was investigated. Most importantly, this research evaluates the effect of an increasing Rytov number on reconstruction performance. Additionally, for each Rytov number, a range of Greenwood frequencies and SNR's are investigated. Finally, two r_0 's were considered at $d/r_0 = 1$ (Challenging) and $d/r_0 = 1/2$ (More realistic). This is all summarized in Fig. 3.8.

Table 3.2: Atmospheric propagation setup parameters.

σ_x^2	d/r_0	δ_{src} [mm]	δ_{AOsys} [mm]	N Grid Points	C_n^2	D_z [km]
0.04	1	0.4	8	1024	2e-14	1
0.5	1	4	4	2048	1e-15	20
1	1	5	7	2048	4e-16	50
0.5	0.5	9	13	1024	7.88e-17	80
1	0.5	12	15	2048	2.2e-17	244

- Horizontal Propagation of a point source
- Hold d/r_0 constant in all cases: 1, $1/2$
- Vary Rytov Number: 0.04, 0.5, 1
- Vary Greenwood Frequency: 20, 40, 60, 80, 100Hz

Lead to various combinations of D_z , C_n^2 , and V_{wind}

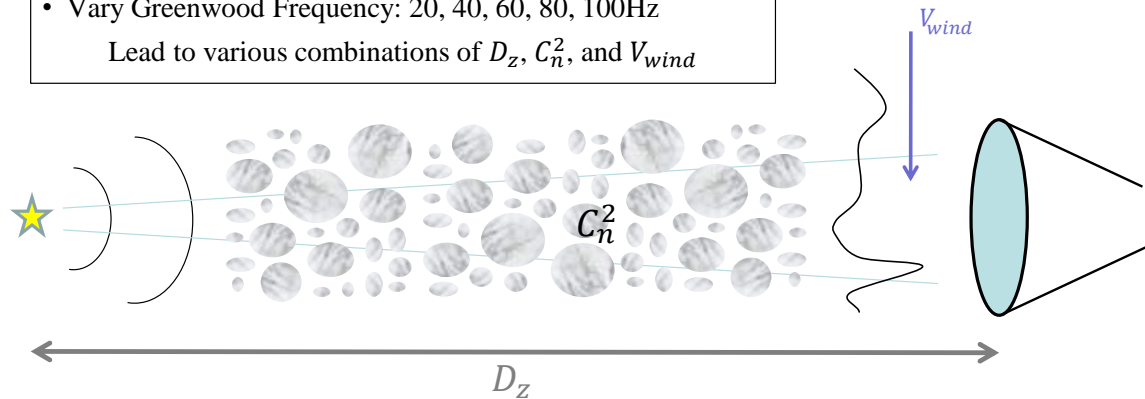


Figure 3.8: Point source atmospheric propagation setup.

IV. Simulation Results

This chapter first presents a compiled set of simulation results from the various reconstruction methods introduced in Ch. II. Obvious performance improvements from the traditional least squares reconstruction approach are seen, especially as turbulence strength increases. While that was the original intended scope for the simulation portion of this research, further investigations led the author to several additional insights on PCO-based reconstruction that greatly clarify previous questions and hypotheses. These new findings include least squares phase anomalies due to gradient aliasing, the cause and potential solutions to sharp fades when using PCO reconstruction in strong turbulence, and refined behavior models of h_{opt} during closed-loop operation. This chapter concludes with an extension of the PCO technique in strong turbulence to beam projection applications.

4.1 Reconstructor Performance

Due to the large number of simulations run, this section presents a summarized set of the raw results. While exploring the effects of SNR and Greenwood frequency were informative along the research pathway, the more general performance trends between each reconstruction technique can be explored without these details. The tables that follow present averaged statistics of the field-estimated Strehl ratio from each one second simulation run. For each Rytov number and reconstructor combination, all simulations were grouped together to calculate the mean, standard deviation, and normalized standard deviation of the field-estimated Strehl ratio. The mean Strehl ratio measures absolute AO correction performance, and the standard deviation of the Strehl ratio measures the stability of the AO correction. Higher mean Strehl ratios and lower standard deviations are desired. More detailed plots of the simulations run, linking effects of SNR and Greenwood frequency, are found in Appendix A.

Table 4.1: Averaged field-estimated Strehl ratios over all Greenwood frequencies and SNR's tested for the cases listed.

σ_x^2	LS	LSPV+1	LSPV+4	Histogram	Iter. Probe	Brent's
0.04	0.5406	0.5416	0.5416	0.5416	0.5416	0.5416
0.5	0.3242	0.3844	0.3869	0.3876	0.3872	0.3846
1	0.0949	0.2047	0.2177	0.2183	0.2202	0.2134

Table 4.2: Field-estimated Strehl ratio standard deviation, averaged over all Greenwood frequencies and SNR's tested for the cases listed.

σ_x^2	LS	LSPV+1	LSPV+4	Histogram	Iter. Probe	Brent's
0.04	0.0329	0.0322	0.0322	0.0322	0.0322	0.0322
0.5	0.0835	0.0498	0.0496	0.0470	0.0487	0.0488
1	0.0677	0.0647	0.0674	0.0625	0.0626	0.0646

Table 4.3: Field-estimated Strehl ratio normalized standard deviation, averaged over all Greenwood frequencies and SNR's tested for the cases listed.

σ_x^2	LS	LSPV+1	LSPV+4	Histogram	Iter. Probe	Brent's
0.04	0.0628	0.0613	0.0613	0.0613	0.0613	0.0613
0.5	0.2581	0.1310	0.1295	0.1223	0.1267	0.1278
1	0.7162	0.3198	0.3152	0.2899	0.2881	0.3058

4.2 Low SNR Reconstruction and Phase Discrepancies

Among the first observations made was in the initial weak turbulence testing. In weak turbulence, there are no branch point effects present, and therefore $\phi_{rot} = \mathbf{0}$ in the absence of any noise effects. The expectation was to observe equivalent performance between all reconstructors. However, a consistent performance improvement of all tested PCO reconstructors was seen over the least squares reconstructor, specifically at the lowest SNR's tested. This was very much a surprise, as prior work hypothesized that the addition of noise may be debilitating to the PCO technique [31]. This sparked a series of follow-up investigations to explore what was going on. All tests performed verified the initial findings that all the PCO reconstructors outperformed the least squares reconstructors in low-SNR situations. The question then became: Why?

An initial theory was proposed by the author that was based on differing noise propagation through the two reconstruction techniques. The hypothesis is based on the idea that the least squares operator could actually amplify the SRI measurement noise such that

$$\|\phi_{LS_n}\|_2 \geq \|\phi_n\|_2 \quad (4.1)$$

where ϕ_{LS_n} is the least squares propagated noise component, ϕ_n is the noise component from the measurement process, and $\|\cdot\|_2$ is the Frobenius norm [16]. This idea was formed by calculating the condition number [16] of the least squares reconstruction matrix and finding it to be roughly 15 – ignoring the suppressed reconstruction modes. Now relate this to the PCO algorithm defined in Eq. (2.42):

$$\hat{\phi}_{PCO} = \phi_{LS} + \mathcal{W}[\phi_{SRI} - \phi_{LS}]. \quad (4.2)$$

The above form can be expanded in terms of all noise components involved:

$$\hat{\phi}_{PCO} = \phi_{LS_\phi} + \phi_{LS_n} + \mathcal{W}\{\mathcal{W}[\phi + \phi_n] - (\phi_{LS_\phi} + \phi_{LS_n})\}. \quad (4.3)$$

The theory proposes that the two ϕ_{LS_n} terms cancel each other out in the PCO process, leaving only ϕ_n contributing to the final reconstruction. Under the assumption of Eq. (4.1), only having ϕ_n would be less of a degradation than ϕ_{LS_n} . A rough analytical trace for this theory was created, but it needed additional verification to justify some simplifications made.

A simulation was written to model this process which proved the theory wrong. This verification simulation models AO system behavior in steady-state closed-loop operation by generating an irrotational test field (could be as simple as a plane wave) that has a nearly flat wavefront. The mean field irradiance is scaled using the equations from Sec. 3.1.3 to have an SNR of roughly 1.5. This field is sent through the SRI model to add realistic measurement noise effects, and that field, ϕ_{SRI} , is sent through both a least squares reconstructor and a simple LSPV+1 reconstructor. From these, the noise terms can be extracted and examined.

Specifically, the simulation found that

$$\phi_{LS_n} = \phi_n, \quad (4.4)$$

which invalidated the author's original theory for the PCO reconstructor performance improvement. In hopes of gleaning more, additional realizations of noise were run, and something unexpected was noted in a number of cases. Amongst other things, the simulation plotted $\phi_{LS_n} - \phi_n$, usually showing no difference. However, Figs. 4.1a and 4.1b show two examples of what appeared to be branch points at first glance.

Yet, these are not branch points for a number of reasons. First, the field that was input to the SRI had a uniform irradiance. One could argue that shot noise creates areas of zero irradiance, which is a valid argument. The detected field irradiance can be calculated from the SRI interferograms by Eq. (2.21), and Fig. 4.2 shows the estimated input irradiance corresponding to the measurement of Fig. 4.1b. It is clear that areas of zero detected photons are scattered all over the aperture, but there is no correlation to the anomalies

observed in Fig. 4.1b. Since these effects do not seem to be caused by the input irradiance, looking to the SRI phase measurement, a clue is found. Shown in Figs. 4.3a and 4.3b, the points from Figs. 4.1a and 4.1b can be traced to points in equivalent locations within the SRI phase that make transitions larger than π radians between adjacent subapertures due to measurement noise. While examining ϕ_{SRI} , closer examination was given to both the least squares and LSPV+1 reconstructed wavefronts, and it was clear that while the PCO reconstructor successfully reconstructed the original phase, the least squares reconstruction had anomalies at the locations of the sharp phase differences in ϕ_{SRI} .

To further examine this phenomenon, a second simulation was run that isolates the noise generated large phase differences from the SRI. A hypothetical ϕ_{SRI} is generated that is completely flat except for two adjacent center subapertures that are set to -0.9π and 0.9π , as shown in Fig. 4.4a. Without the surrounding additional noise, this simulation exposes the aperture-wide reconstruction effects due to large noise-induced adjacent phase difference. Figure 4.4c shows the LSPV+1 reconstruction, matching the SRI wavefront with an extra π piston shift from the PCO h term. On the other hand, the least squares reconstruction clearly identifies the source of the phase anomalies evident in Fig. 4.1.

The ϕ_{rot} term from the PCO algorithm cancels out the least squares anomaly; however, this exposes a misnomer in this case. The wrapped term in the PCO algorithm, which in a noiseless case is equivalent to any rotational component in the phase function, can actually be any phase components missed, or in this case artificially introduced by the least squares reconstruction relative the SRI phase measurements. The author likens this to accounting for slope discrepancies when using a Shack-Hartmann WFS. Since the SRI measures phase, not wavefront gradients, the author terms this as accounting for the phase discrepancy. In the case of the noise induced phase discrepancies, they are not actually rotational in nature. As described in Sec. 2.3 a least squares generated operator cannot reconstruct rotational phases. Further, Fig. 4.5 plots the gradients for one of these anomalies, where red represents

a positive field and blue is negative. The author stresses these arguments to say these are not so-called “noise-induced branch points”. They are not rotational, and they are actually anomalies introduced by the least squares reconstruction that do not exist in the true phase function.

Since these phase discrepancies result from noise creating artificially large adjacent phase measurements on an otherwise nearly-flat wavefront, it is now clear why all PCO algorithms outperform the least squares reconstructor when no branch points are present and only at the very lowest SNR’s. The author’s original theory failed to explain why the performance gain was only seen at SNR’s lower than five, as it predicted a lowered noise propagations for any noise present. The new theory requires such low SNR’s to induce the large adjacent phase measurement errors. If only using a least squares reconstructor in these cases, the control system will attempt to conjugate these phase discrepancies that do not exist in the true wavefront leading to potentially unstable AO performance.

The cause for the observed least squares behavior turns out to be an aliasing effect of the wavefront gradients fed to the the least squares reconstructor. Section 4.5 presents the research that led to this recent understanding. Any gradients larger than π radians are assumed to be wrapping cuts; however these points are not wrapping cuts. So, the large adjacent gradients are wrapped, but the surrounding gradients remain. This is the cause for the phase discrepancy surrounding such points.

4.3 Closed-Loop Behavior of h_{opt}

Pellizzari’s work found a numerical PDF approximation for h_{opt} [31], which found $\langle h_{opt} \rangle = 0$. However, there is a very important difference between preceding research and this work in the implementation of the PCO wrapping operator. Previously, the wrapping

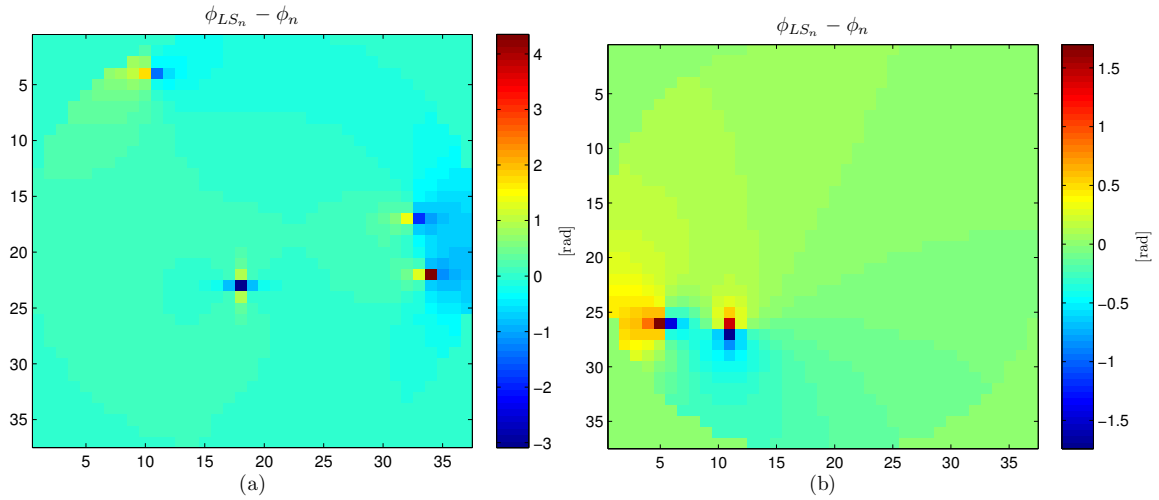


Figure 4.1: Different realizations of unexpected differences between LS noise term and PCO noise term.

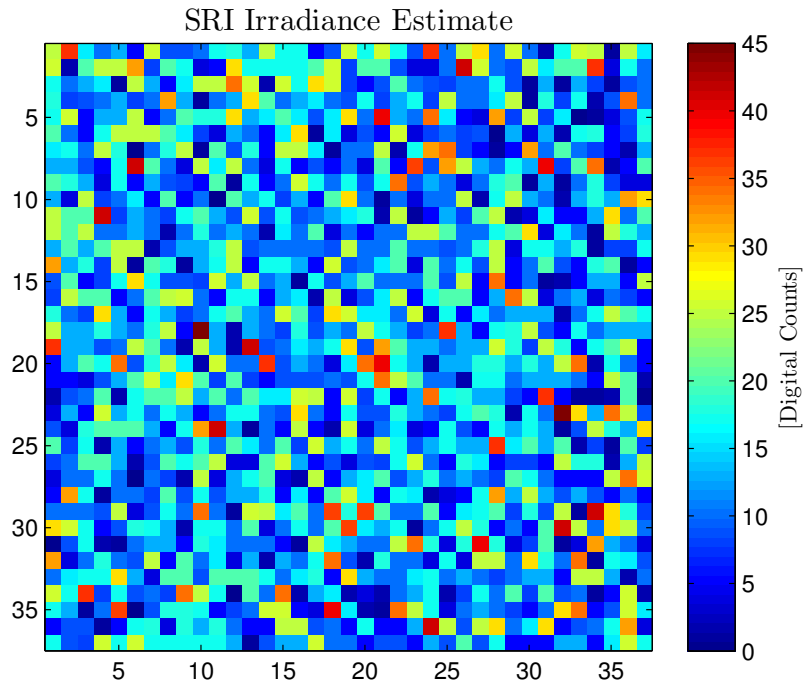


Figure 4.2: Irradiance estimate of input SRI field from noise behavior simulation. This corresponds to the measurement of Fig. 4.1b.

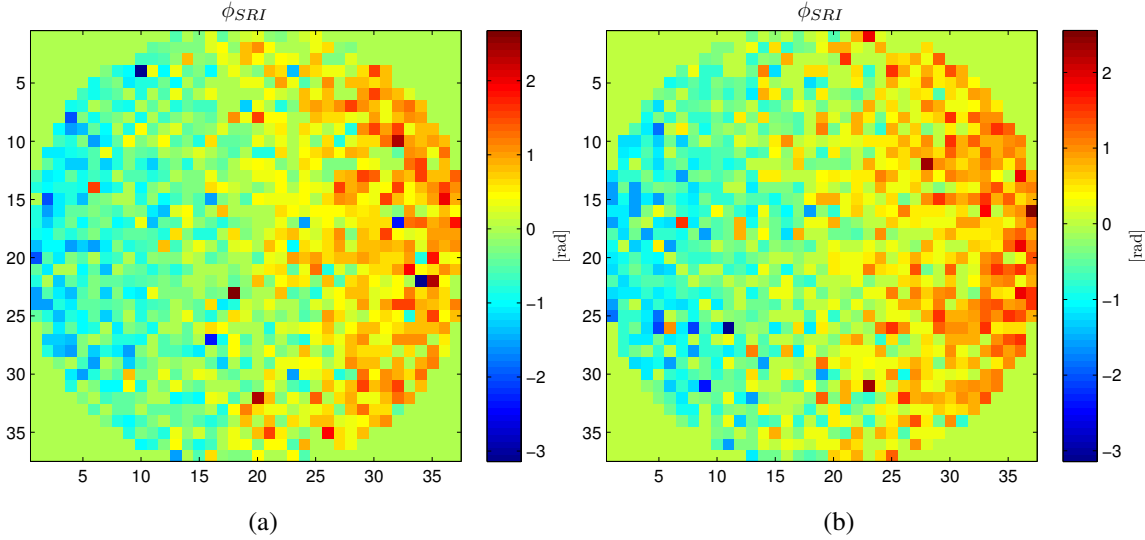


Figure 4.3: SRI phase measurements of a tilted wavefront where $\text{SNR} \approx 1.5$. In the subplots, (a) corresponds to Fig. 4.1a and (b) corresponds to Fig. 4.1b.

was performed by

$$\mathcal{W}[\phi] \equiv \frac{\text{Tan}^{-1}\{\text{imag}[\exp(i2\pi\phi)], \text{real}[\exp(i2\pi\phi)]\}}{2\pi}, \quad (4.5)$$

which is physically correct but not computationally efficient. Switching to a modulus operator, this process can be implemented easily on most CPU's and FPGA's used for AO control. This is simply written as

$$\mathcal{W}[\phi] \equiv \text{mod}(\phi, 2\pi). \quad (4.6)$$

Both methods are correct, but the wrapping window for Eq. (4.6) is now from 0 – 2π radians, rather than $-\pi$ – π radians. When this research began testing LSPV+1, based on Eq. (4.6), the AO performance was terrible. After recalculating the PDF of h_{opt} , it was obvious that the PDF calculated by Pellizzari needs to be defined with respect to the wrapping window being used. By shifting his entire PDF to be over the new wrapping window, $\langle h_{opt} \rangle = \pi$. It turns out the initial implementation of LSPV+1 tested here, used the least optimal h , leading

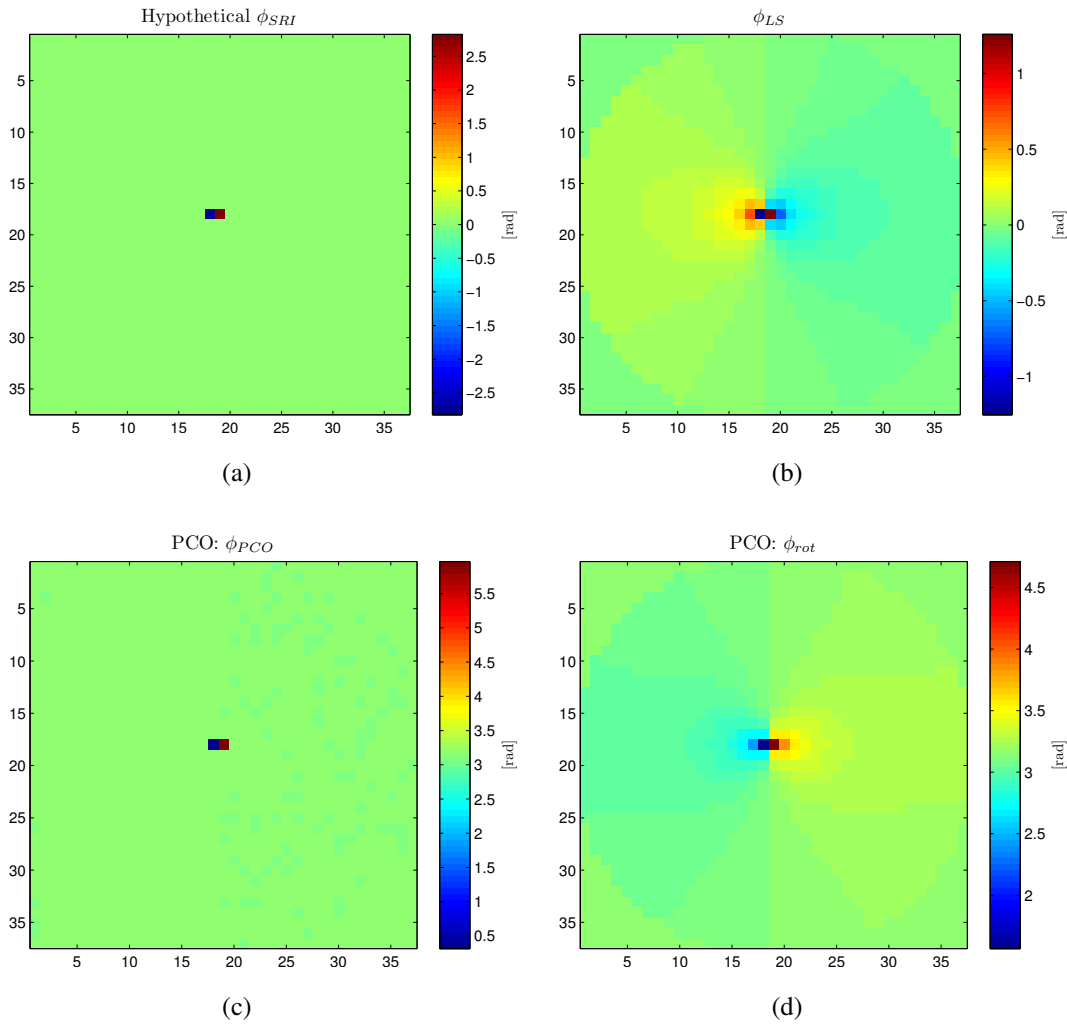


Figure 4.4: Simulation of low-SNR noise effects between least squares and LSPV+1 reconstructors.

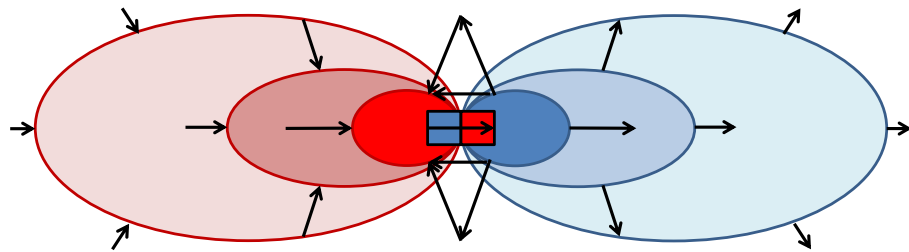


Figure 4.5: Simplified wavefront gradient diagram of a noised induced phase anomaly. The center two squares represent the central discrete pixels of the anomaly.

to the poor results observed. This is an important lesson for practically implementing these algorithms or anyone implementing a non-standard wrapping function for a PCO application.

Over the course of this research, it was noted that the LSPV+1 reconstructor demonstrated near equivalent AO performance to the more advanced PCO reconstructors tested. The computational simplicity of LSPV+1 makes it a promising lead for high-speed and low-latency AO. It was also noted that the LSPV+1 performance gap between the other PCO algorithms widens as the Rytov number increases. Although the performance is still very similar, as seen by Table 4.3, the increasing performance gap between LSPV+1 and the other PCO reconstructors at $\sigma_\chi^2 = 1$ prompted an investigation as to why.

LSPV+1 always uses $h = \langle h_{opt} \rangle$, which in the weak Rytov case is more than sufficient when no branch points are present. However, as the Rytov number increases and additional rotational phase components are introduced, one can surmise that only having one realization of ϕ_{rot} could be limiting in some cases. The previous research did not show significant variations in the PDF of h_{opt} as the Rytov number increased above weak turbulence, perhaps due to the absence of noise effects. However, a series of simulations were run to retest this idea with the hypothesis that the PDF of h_{opt} broadened away from $\langle h_{opt} \rangle$ as the Rytov number increased. To generate the PDF's, LSPV+200 was run over a series of one-second cases, each with increasing challenge for the AO system. For each simulation, a histogram was generated of the h_{opt} values chosen by the LSPV+200 algorithm to generate a rough PDF. Figures 4.6 and 4.7 show the simulation results with the histograms as well as field estimated Strehl ratio plots overlaid with the normalized h_{opt} as a function of time. As the AO beacon conditions worsen, the histogram shows a broadening of h_{opt} 's PDF. All turbulence parameters showed a slight broadening effect of the distribution, but increasing Rytov number is by far the dominant factor.

The confirmed broadening of the h_{opt} PDF explains why the LSPV+1–LSPV+4 performance gap widens as the atmospheric conditions worsen. This fact also may lend to choosing a specific PCO reconstructor based on expected conditions. As the conditions become increasingly difficult, particularly with respect to Rytov number, it may be more beneficial to take the additional computational hit with one of the other PCO reconstructors.

4.4 Fades in Strong Turbulence

While debugging the reconstruction and AO system simulation, a mechanism was implemented to record videos of many important system parameters as the system stepped through time. Following the development phase, this capability was used to study the overall behavior of the AO system when using a PCO wavefront reconstructor. This additional work resulted in identifying the source of fades when using a PCO reconstructor when a significant rotational phase is present in the input wavefronts.

At system startup, the WFS observes the fully aberrated beacon wavefronts, ϕ . At this point, the complete rotational phase from any branch points reaches the WFS. When the AO system switches on, the DM conjugates the reconstructed WFS field. Now, the WFS senses only the residual wavefront error, ϕ_{resid} – not the fully aberrated wavefronts. The control law maintains the DM commands at roughly the conjugate of the incoming aberrations, but the wavefront reconstructor is no longer seeing the fully aberrated field. As ϕ_{resid} flattens out, the PDF of h_{opt} becomes increasingly centered about $\langle h_{opt} \rangle$.

This was all known prior to the research presented here; however, additional insights may be gleaned by thinking deeper into the process. In steady-state, closed-loop operation, the residual wavefront error is near-zero. Any branch points and corresponding branch cuts that are present within ϕ may not be visible in ϕ_{resid} , and even if they are partially apparent, they would most likely be of reduced visibility due to partial compensation. In this regime, the branch cut finding algorithm may easily miss cuts that are actually present

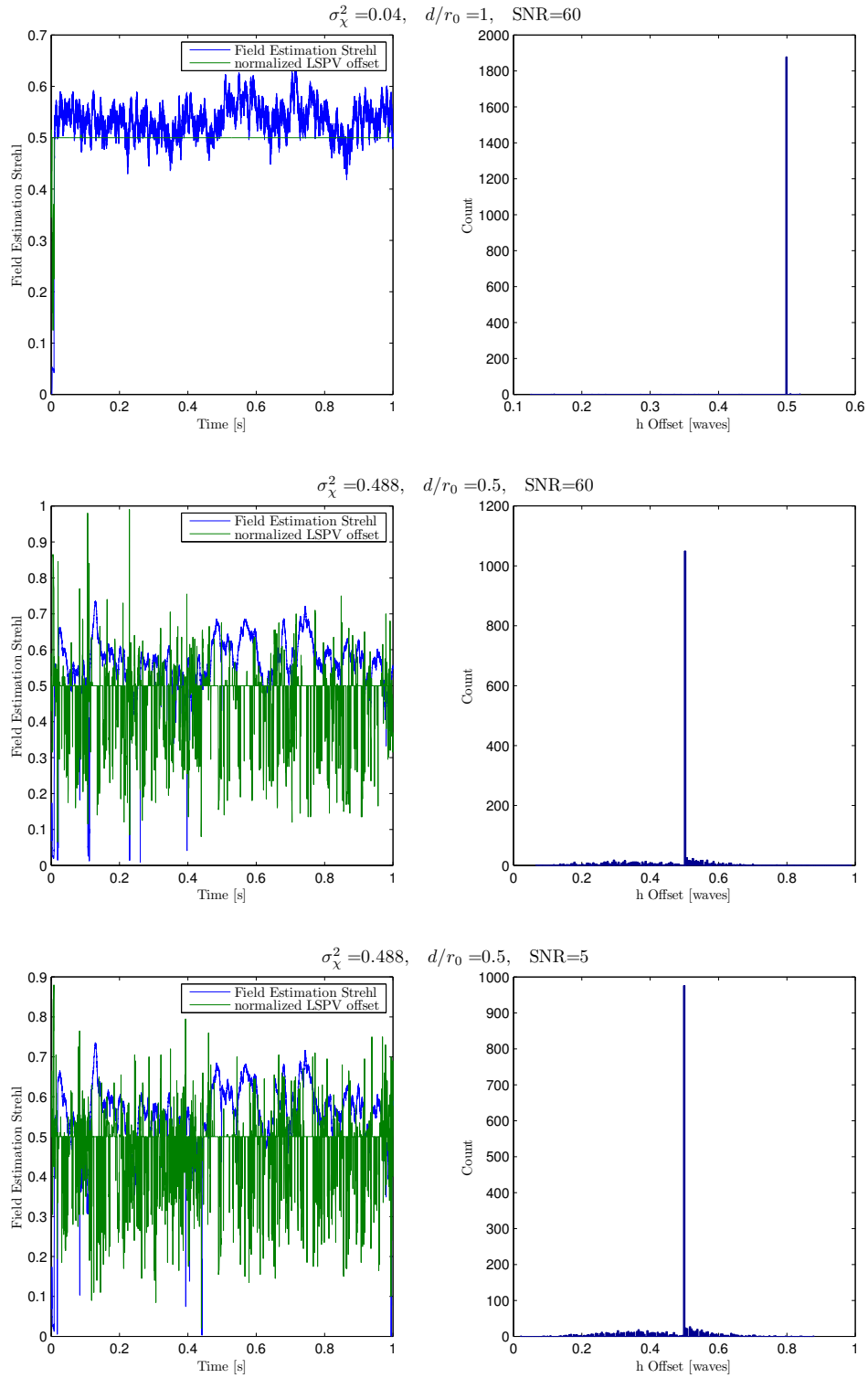


Figure 4.6: LSPV+200 Strehl ratio and h_{opt} plots over one second simulation runs to evaluate the behavior of h_{opt} 's PDF as atmospheric conditions change.

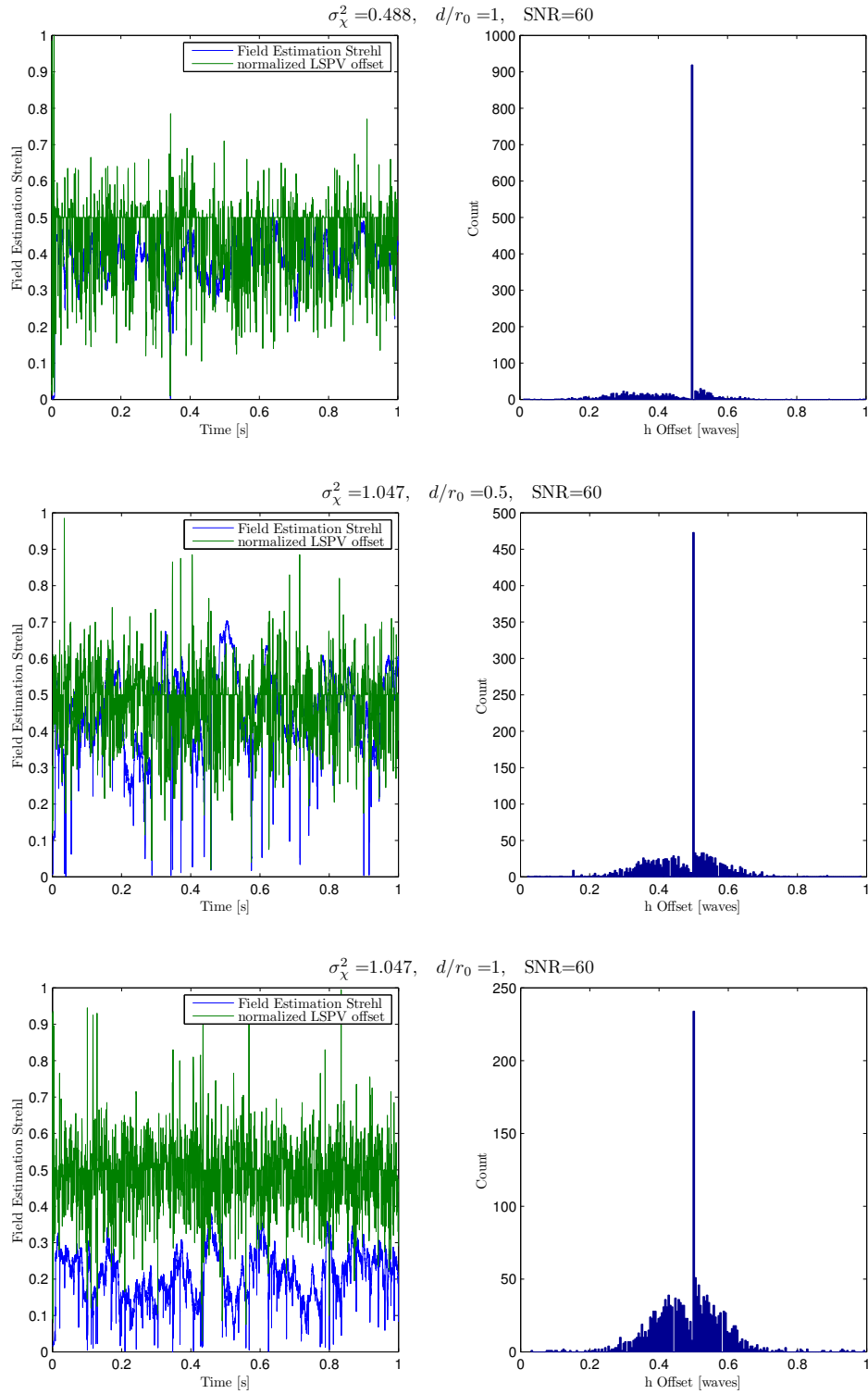


Figure 4.7: LSPV+200 Strehl ratio and h_{opt} plots over one second simulation runs to evaluate the behavior of h_{opt} 's PDF as atmospheric conditions change.

in the corrected field. The author poses a question as to what IWCL really means, since IWCL was meant to be calculated over the fully aberrated wavefront, ϕ , not ϕ_{resid} .

So what is going on when a PCO algorithm changes h_{opt} while in closed-loop operation? Well, it depends primarily on the rotational effects present in the field; in other words, the Rytov number. Starting the discussion with a weak Rytov number case, the rotational component of the PCO reconstruction was seen to be almost always completely zero, with the exception of any noise induced effects presented in Sec. 4.2. In this weak turbulence case, h_{opt} very rarely changes, and when it does change due to noise induced phase anomalies, it has no effect on the overall system performance.

In the medium Rytov number cases simulated, similar behavior is noted. Figure 4.8 shows a plot of field-estimated Strehl ratio, overlaid with each frame's h_{opt} for an LSPV+4 reconstructor. In this regime, h_{opt} changes frequently, but overall AO performance remains unaffected. This initially disagreed with the author's theories, as the PCO rotational phase component was seen to have consistent notable content. However, the most recent discoveries show that this content is not rotational in nature. The cause is discussed at length in Sec. 4.5. Without a significant rotational component within the residual phase error, h_{opt} varies in a way to keep the PCO phase discrepancies within the wrapping window and away from the wrapping boundaries. At a change in h_{opt} , only the reconstructed wavefront's piston changes, but since piston is removed prior to sending DM commands out, there is no performance impact. While there are a few exceptions, this is the primary behavior observed in the medium Rytov number cases.

Things change with strong Rytov number cases. As Fig. 4.9 shows, any changes in h_{opt} mostly result in sharp fades. More specifically, the fades distinctly follow changes in h_{opt} . Using the video capability developed for debugging, it was noted that the tracking spot shape is not effected at these fades but is shifted off-axis. This behavior was consistently observed at the fades in Strehl ratio. It seemed that the change in h_{opt} somehow propagates

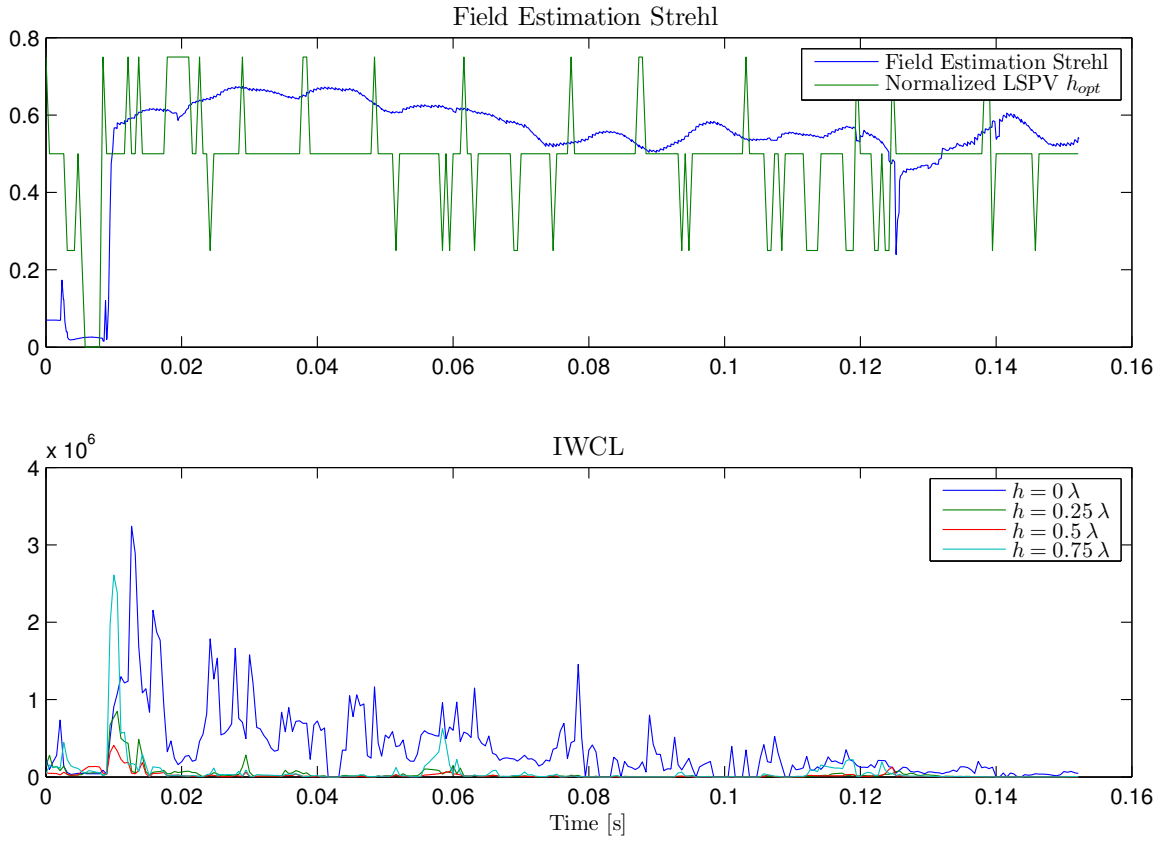


Figure 4.8: The top plot shows field estimated Strehl ratio and h_{opt} over time with an LSPV+4 reconstructor. The bottom plot shows the IWCL for each of the four ϕ_{rot} realizations over the same time interval. This is in conditions of $\sigma_\chi^2 = 0.5$, $f_g = 40\text{Hz}$, $d/r_0 = 1/2$.

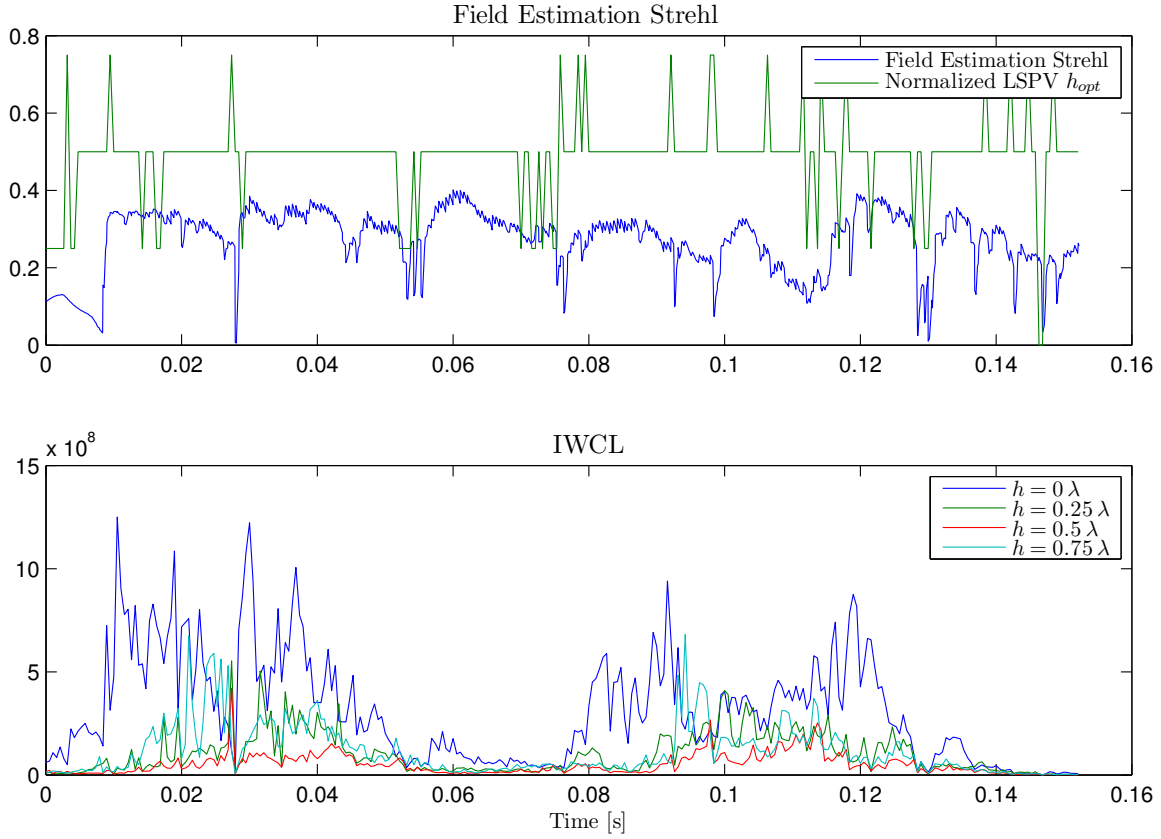


Figure 4.9: The top plot shows field estimated Strehl ratio and h_{opt} over time with an LSPV+4 reconstructor. The bottom plot shows the IWCL for each of the four ϕ_{rot} realizations over the same time interval. This is in conditions of $\sigma_x^2 = 1$, $f_g = 40$ Hz, $d/r_0 = 1/2$.

a change in tilt through the AO system, thus causing the fades. This prompted several simulation tests, one of which lead to an explanation.

A number of AO simulations were rerun with the LSPV+4 reconstructor, this time calculating the tilt components for each PCO rotational phase realization. Since h_{opt} seemed to be at the root of the behavior, the least squares reconstruction was ignored for these tilt calculations. Figure 4.10 shows the results from the three Rytov cases. First to

note is that the tilt components of the PCO rotational phase definitely differ as h is varied! For the weak case, all rotational tilt components vanish as soon as the higher-order control loop closes – as expected. In the medium case, the three most likely h -values produce small, yet similar tilts. However, in the strong case, even after the higher-order control loop engages, there is widely varying tilt components between each rotational phase realization. This is the key.

In the strong Rytov case, when the PCO algorithm changes h_{opt} , a new wavefront tilt realization is reconstructed. When this propagates through the rest of the higher-order control data path, described in Sec. 3.1.1, the final tilt-removal operator cuts out whatever tilt component exists. To the tracking system, these changing tilts are certainly measurable. This is the cause for the fades in Strehl ratio. While the higher-order correction of the wavefronts do not suffer during the changes in h_{opt} , it takes the tracking system roughly two frames to account for the tilt changes from the high-order system. To explicitly demonstrate this process, Appendix B traces a hypothetical rotational phase through the AO system.

4.4.1 Potential Fixes.

All the tilt components are known variables, and as such, a solution to prevent the fades is certainly possible. In fact, there are likely a number of potential solutions. One method would be to implement a feed-forward tilt-offloading path to the tracker from the higher-order system. Another method is to allow the higher-order control system to correct for some or all of the reconstructed tilt. At first, the author recalled the tilt coupling issues presented in Sec. 3.1.1, but by lowering the control system gains, a stable state can be reached. While this imposes larger stroke requirements on the deformable mirror, it is a relatively simple controls problem compared to the feed-forward implementation with two different operating frequencies.

The AFIT AO system model was modified to compare AO performance over equivalent realizations of high Rytov turbulence with both a tilt coupled and decoupled

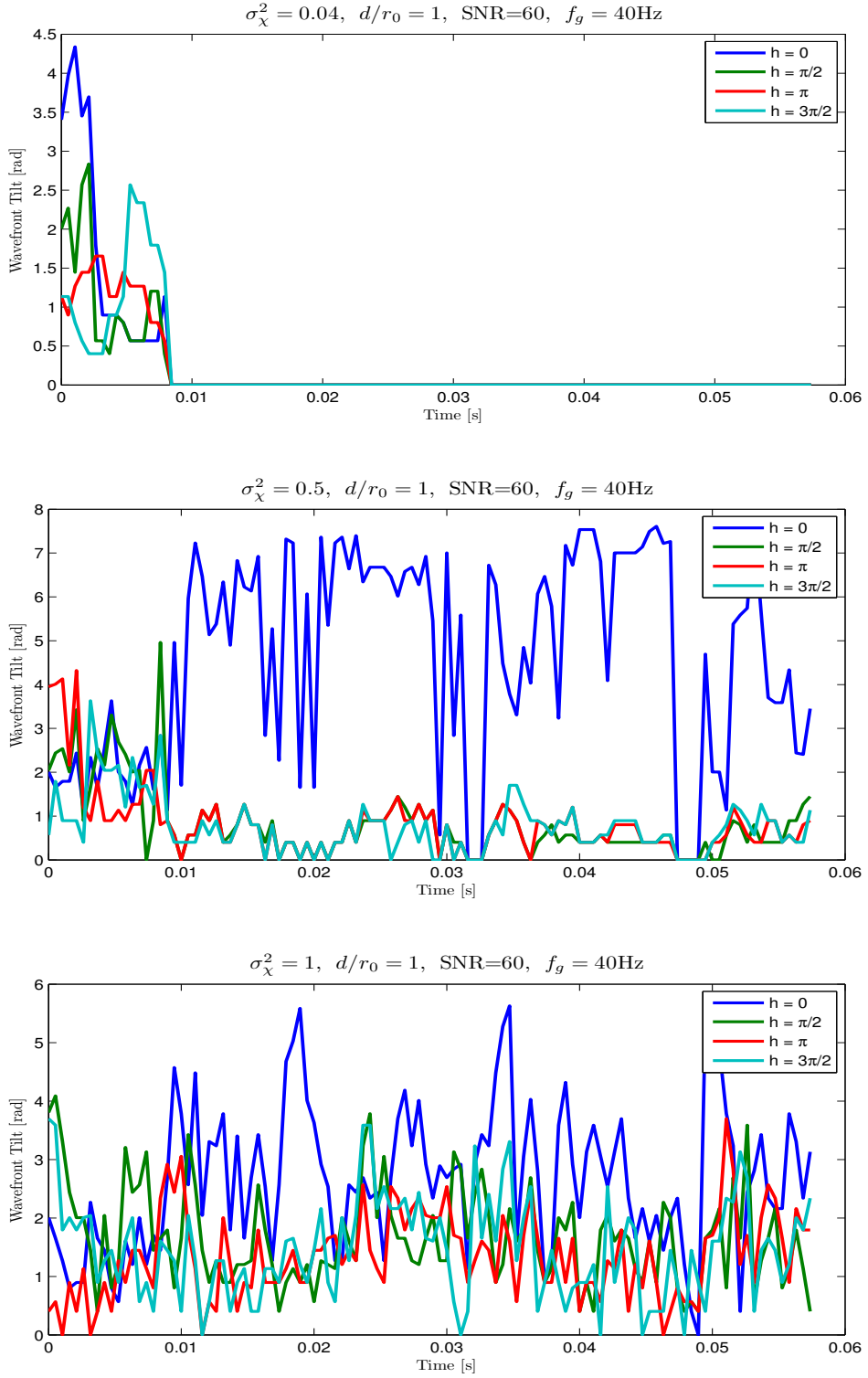


Figure 4.10: Tilt magnitudes for each PCO rotational phase realization of a LSPV+4 reconstructor over time for weak, medium, and strong Rytov numbers. The higher-order control system is seen to engage at $t = 0.008$ s.

control system. The limitations of such a setup are made clear by selecting three increasingly aggressive control gains. Figure 4.11 shows the results, where the left column is decoupled and the right column is coupled. The gain starts at relatively conservative points, giving good performance in each case. However, note there are no fades in the coupled case, even as h_{opt} changes! Increasing the gain, the decoupled performance sharpens but the coupled performance begins to go unstable. Further increasing the gain, the decoupled system still runs well, but the coupled system quickly drives itself unstable. Note that this test in simulation allows for perfect component alignments. In reality there will always be a slight misalignment between components and sensors. Because of this, a zero DC gain controller would be required on both the tracker and higher-order control system to implement a coupled tilt control setup.

This test verifies the theory on tilt propagation from the changing PCO rotational phase realizations to the tracking system as the cause for the sharp fades previously observed with these reconstructors. Further, suggestions for alleviating this are given.

4.5 High SNR Phase Discrepancies

A very recent modification to the simulations was to separate and plot ϕ_{LS} and ϕ_{rot} as the AO frames increment. To the author's great surprise, phase discrepancies similar to those described in Sec. 4.2 were clearly apparent in high SNR conditions of all Rytov numbers tested. This section describes the author's initial tests and theories as to why these phase discrepancies exist and what impact they have on AO performance. The author stresses that these are only initial theories, and further work is needed to refine these ideas.

Figure 4.12 shows an example of the AO system in weak turbulence, with an SNR of 60, prior to closing any of the correction loops. In such low Rytov number and high SNR conditions the PCO rotational phase term was expected to have no content, but that was not the case. The first clue came when the control loops started correcting in the weak

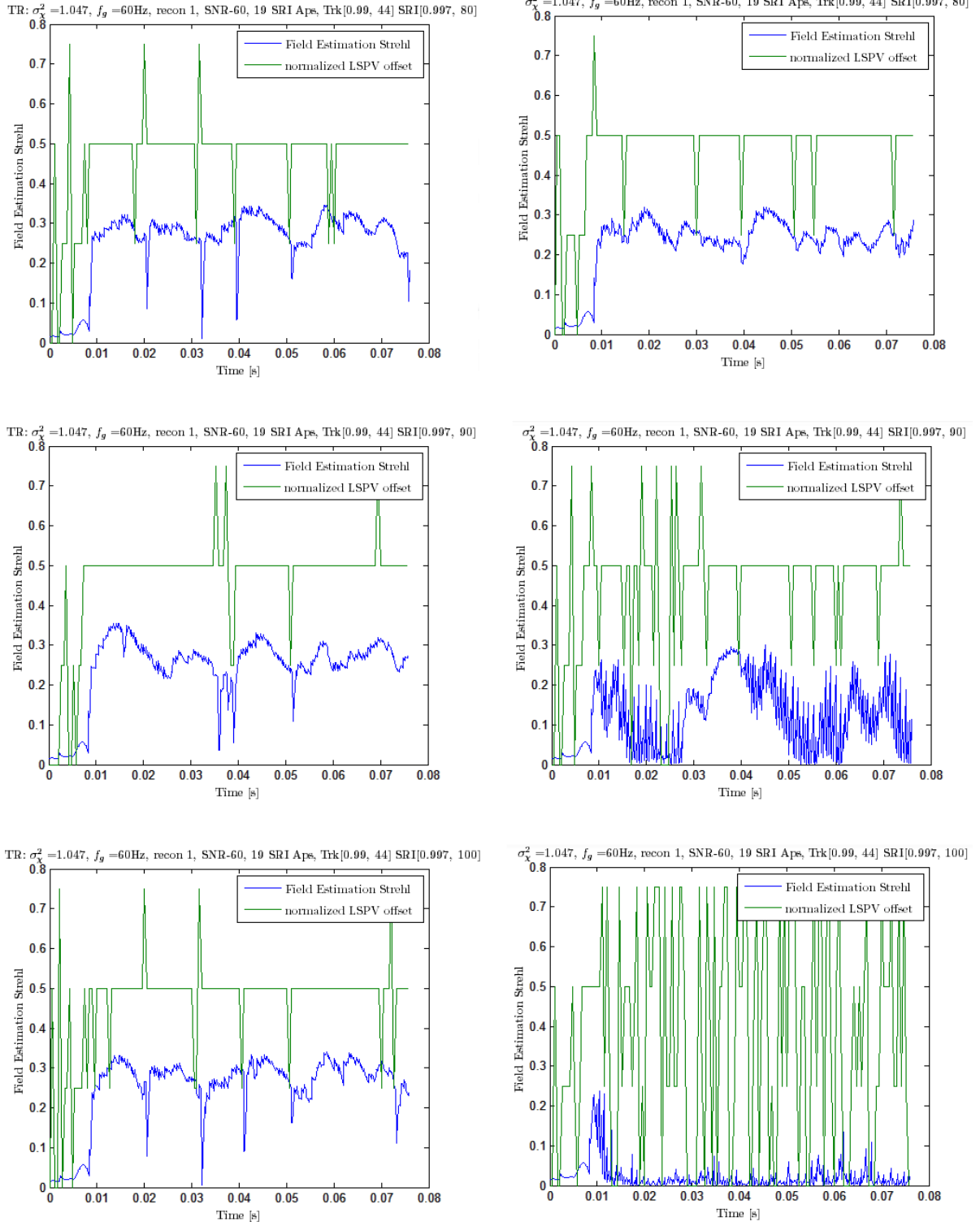


Figure 4.11: Plots of AO performance with tilt decoupled (left column) and tilt coupled (right column) between the two control systems. Each row implements an increasing higher-order control gain.

turbulence case. Within several frames, the PCO rotational component became flat – as we had expected for the entire low-Rytov simulation, shown in Fig 4.13.

The primary differences with regard to the reconstruction process between the two above cases are the magnitudes of the residual wavefront gradients. These phase effects are also present in the higher Rytov number cases, but the low Rytov case excludes any rotational field effects from the analysis. A number of simplified tests were conducted to look at how high localized wavefront gradients propagate through the reconstruction process. The first question was to explore how the SRI and reconstructors handle slopes of increasing magnitude. As previously described, the slopes that the reconstructors operate on are generated by shearing the raw SRI measurements in the x and y directions. To account for wrapping cuts, the sheared slopes are wrapped to be within $-\pi \leq s < \pi$ radians. This slope wrapping operation sets up the fundamental limit on slope magnitudes that can be properly reconstructed by the least squares process. Any slopes between adjacent subapertures larger than π radians will be interpreted, incorrectly, as a wrapping cut.

Figure 4.14 explores this idea with two tilted wavefronts in the first row of plots. The corresponding SRI measurements of each tilted field are shown in the middle row, and the final row shows each least squares reconstruction. The first column is correctly reconstructed, but the second column, which exceeds the tilt sampling limit, has two significant errors. First, the magnitude of tilt over the wavefront is greatly reduced from its actual tilt. Second, the direction of tilt is reversed. The author hypothesizes that the degree of each of these errors will change based on how much tilt is being passed into the system – similar to aliasing in discrete signal theory [29].

Figure 4.15 extends the previous aliasing test closer to the atmospheric simulation conditions. A flat wavefront with a sharp, linear slope down the center of the field is created. The slope is at roughly 0.8π radians per-SRI subaperture. Additionally,

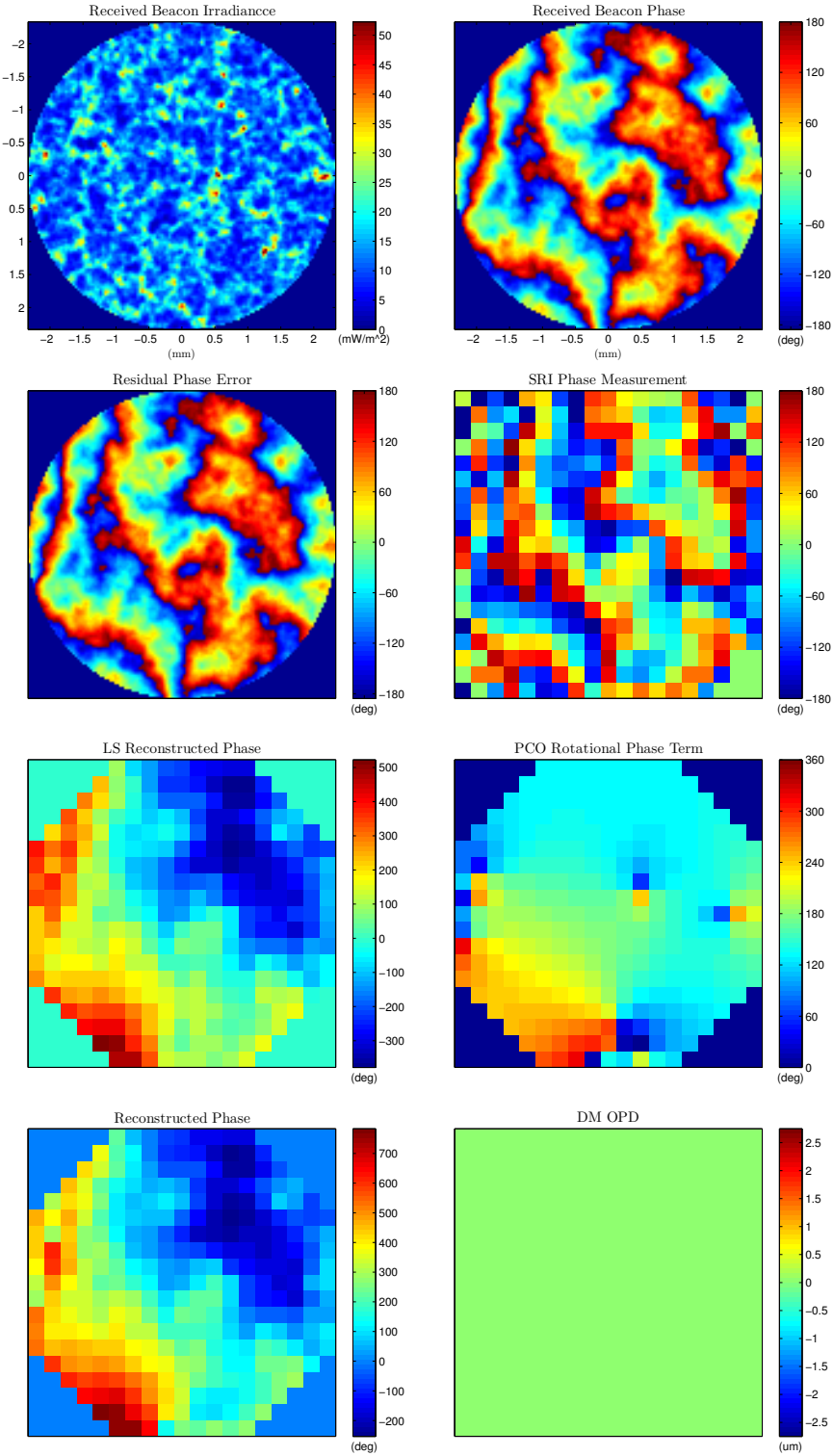


Figure 4.12: Plots of AO state in conditions of $\sigma_\chi^2 = 0.04$, $d/r_0 = 1$. Both tracking and high-order control loops are open.

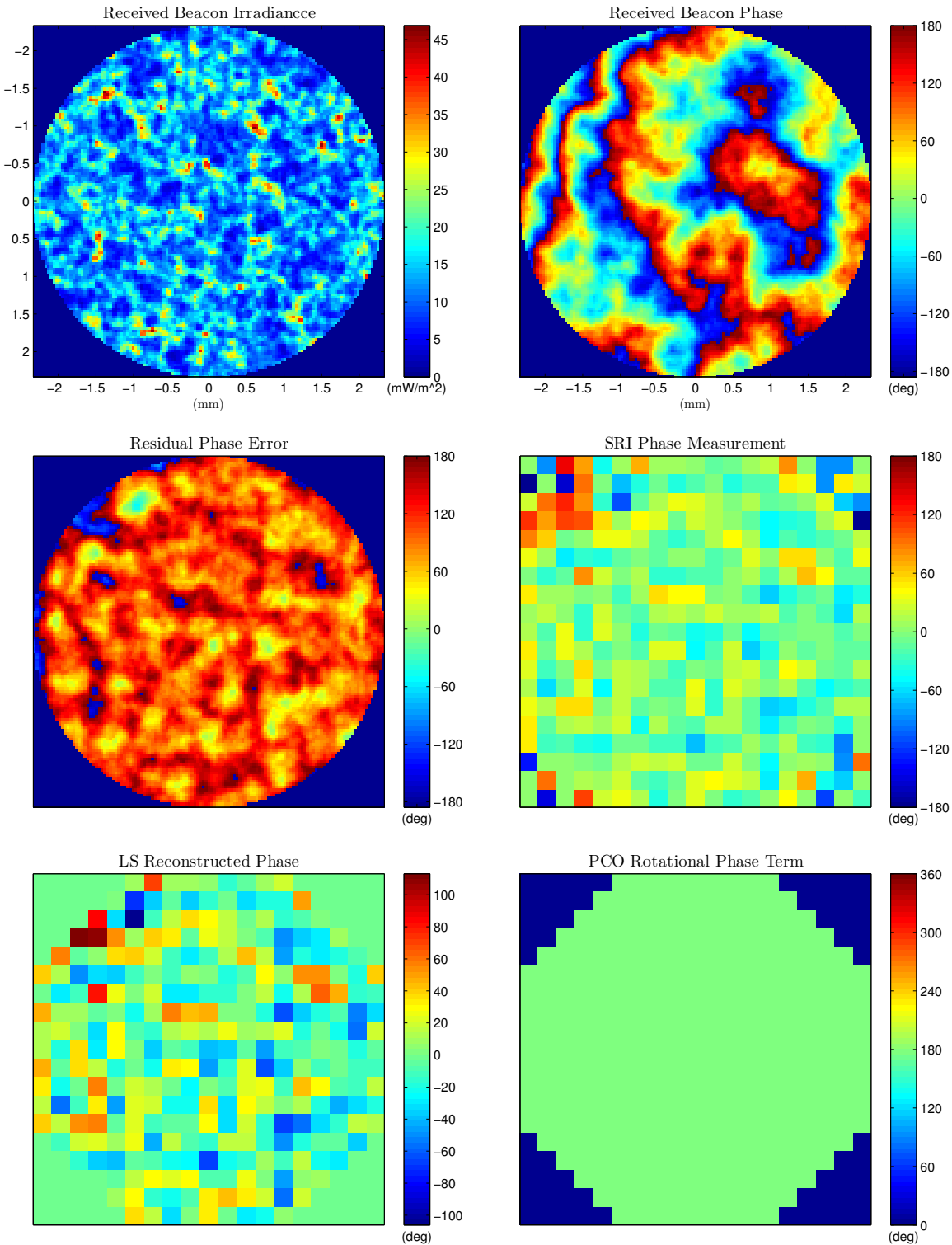


Figure 4.13: Plots of AO state in conditions of $\sigma_\chi^2 = 0.04$, $d/r_0 = 1$. Both tracking and high-order control loops are closed.

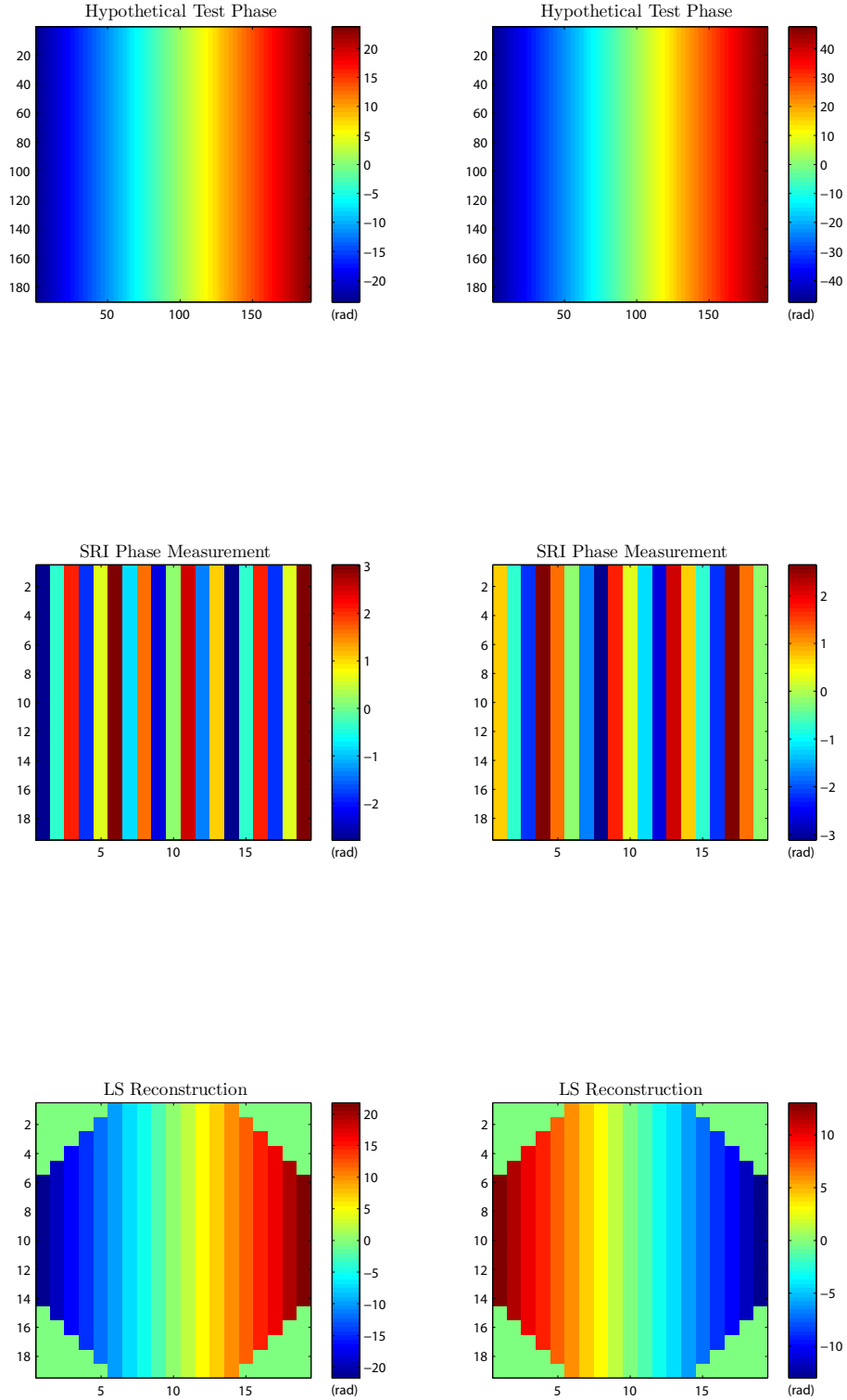


Figure 4.14: Inducing aliasing with the SRI and least squares reconstructor. The left column shows roughly 0.9π radians of tilt between adjacent subapertures, while the right column has roughly 1.5π radians of tilt between adjacent subapertures.

a central region of the slope is set at roughly 1.5π radians per subaperture. This is similar to most of the atmospheric wavefront being within the slope sampling limit of the reconstructor, with small regions that exceed it. The first observation made was that the least squares reconstruction mostly resembles the input wavefront, but it is clear there are some discrepancies, including aliasing over the high-slope region. In the initial tests, only the LSPV+1 algorithm was used for comparison. While it does produce a correct modulo- 2π congruent reconstruction, the ϕ_{rot} realization created has sharp cuts that are less than ideal for any continuous face-sheet DM. This observation motivated a test with the LSPV+4 reconstructor, which calculated the most accurate reconstruction. To the PCO algorithms, the sharp cuts from the LSPV+1 ϕ_{rot} realization are treated as if they were branch cuts. In the LSPV+4 reconstructor, the cuts are penalized, giving a realization that minimizes the sharp transitions.

The author claims these tests point out that sharp, localized wavefront gradients are the cause for the observed phase discrepancies when reconstructing a high-SNR field. The LSPV+4 rotational phase term from Fig. 4.15 has a high resemblance to the features seen in the atmospheric simulations. While these features were not found in low-Rytov number closed loop operation, they were found in the higher Rytov number closed loop simulations. Figures 4.16 and 4.17 show closed loop operation for $\sigma_x^2 = 0.5$ and $\sigma_x^2 = 1$, respectively. The strong turbulence plots show the system as it is initially closing the loop, and some rotational phase due to branch points is likely present in addition to the phase anomalies being discussed here.

These tests shed additional light on the increased performance drop between LSPV+1 and the other PCO reconstructors as the Rytov number reaches one. The broadening of h_{opt} 's PDF must be, in part, due to these phase discrepancies. Further, the previous simulations performed by Pellizzari would likely not have encountered these issues with a simulated SRI of over twice the subaperture density. While increasing the SRI subaperture

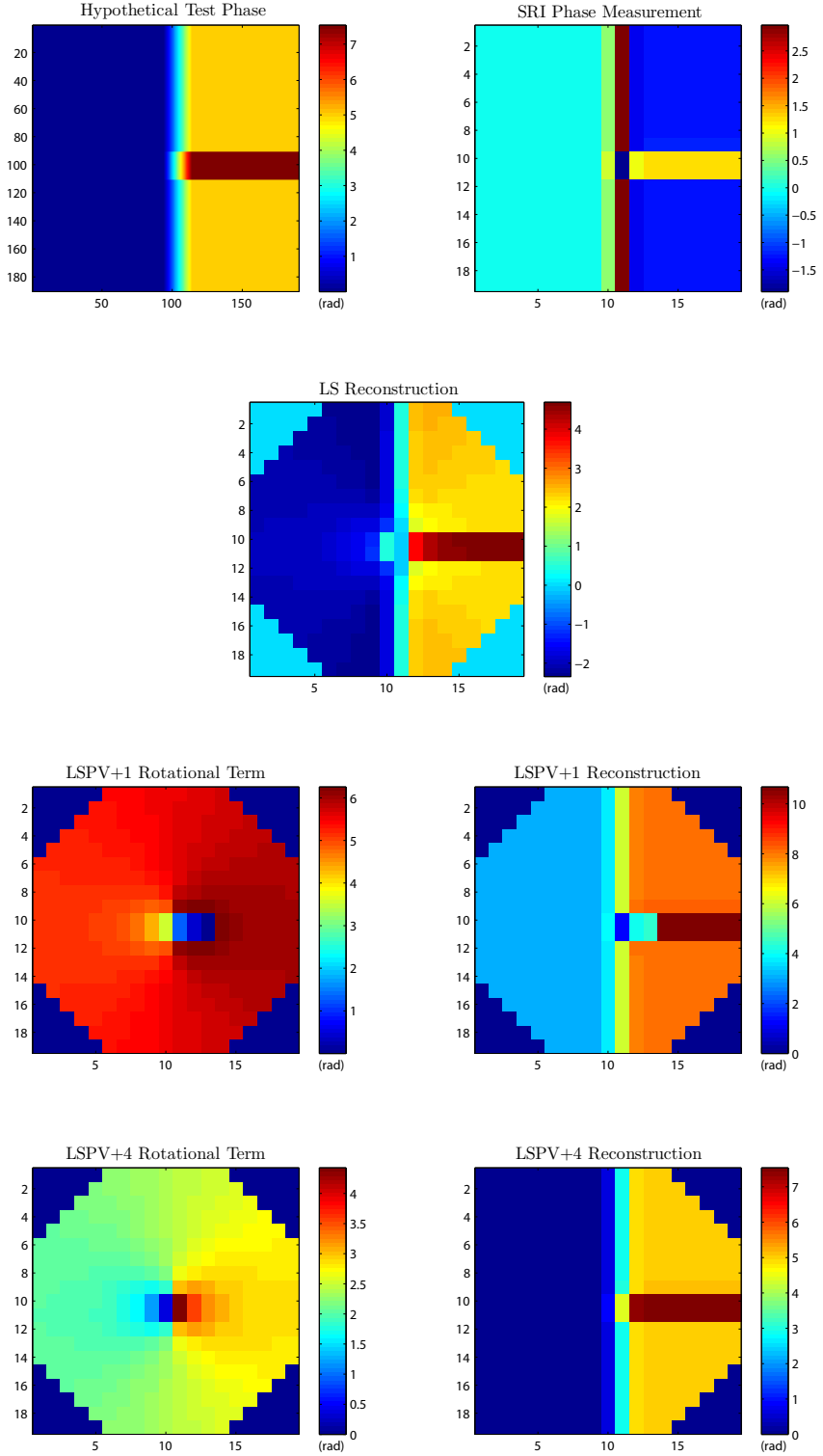


Figure 4.15: Inducing aliasing with the SRI and least squares reconstructor. A tilt runs down the center of the wavefront, and the very central portion exceeds the SRI tilt sampling limit. This is traced through the SRI and various reconstructors.

density is a potential solution to this behavior, one must consider the additional splitting of light and its impact on SNR. The initial results shown here demonstrate an unintended benefit of the PCO algorithm as it compensates for reconstruction errors due to localized wavefront gradient aliasing.

4.6 Application to Beam Projection

All research up to this point regarding PCO-based wavefront reconstructors has been studied with respect to one-way AO systems. Such one-way applications include, but are not limited to, remote sensing and astronomy. Another class of applications involve dual-path propagation, namely those which not only receive light, but also project compensated outgoing beams. Beam projection applications include optical communication and laser weapon systems. These applications typically involve more horizontal propagation paths, thus entering the strong turbulence regime much more frequently than vertical path applications. This section presents initial results and observations for a range of wavefront correction techniques with respect to beam projection applications.

The author hypothesizes most of the same conclusions made for the single-path AO problem hold true but introduces an alternative to intensity weighted cut length (IWCL) for PCO reconstruction. The author hypothesizes that cut length (CL) is a better PCO reconstruction metric for beam projection applications where the outgoing beam is not amplitude modulated to match the received beacon field. While all PCO reconstructed fields will be modulo- 2π equivalent, different PCO variations differ in the placement of detected branch cuts within the field. Assuming an ideal corrector, this does not actually make a difference. However, when a continuous face-sheet DM is used, there will always be a DM fitting error in trying to reproduce the sharp branch cuts.

For initial comparison of wavefront reconstruction techniques with respect to beam projection applications, a simplified simulation was developed using tOSC's WaveProp.

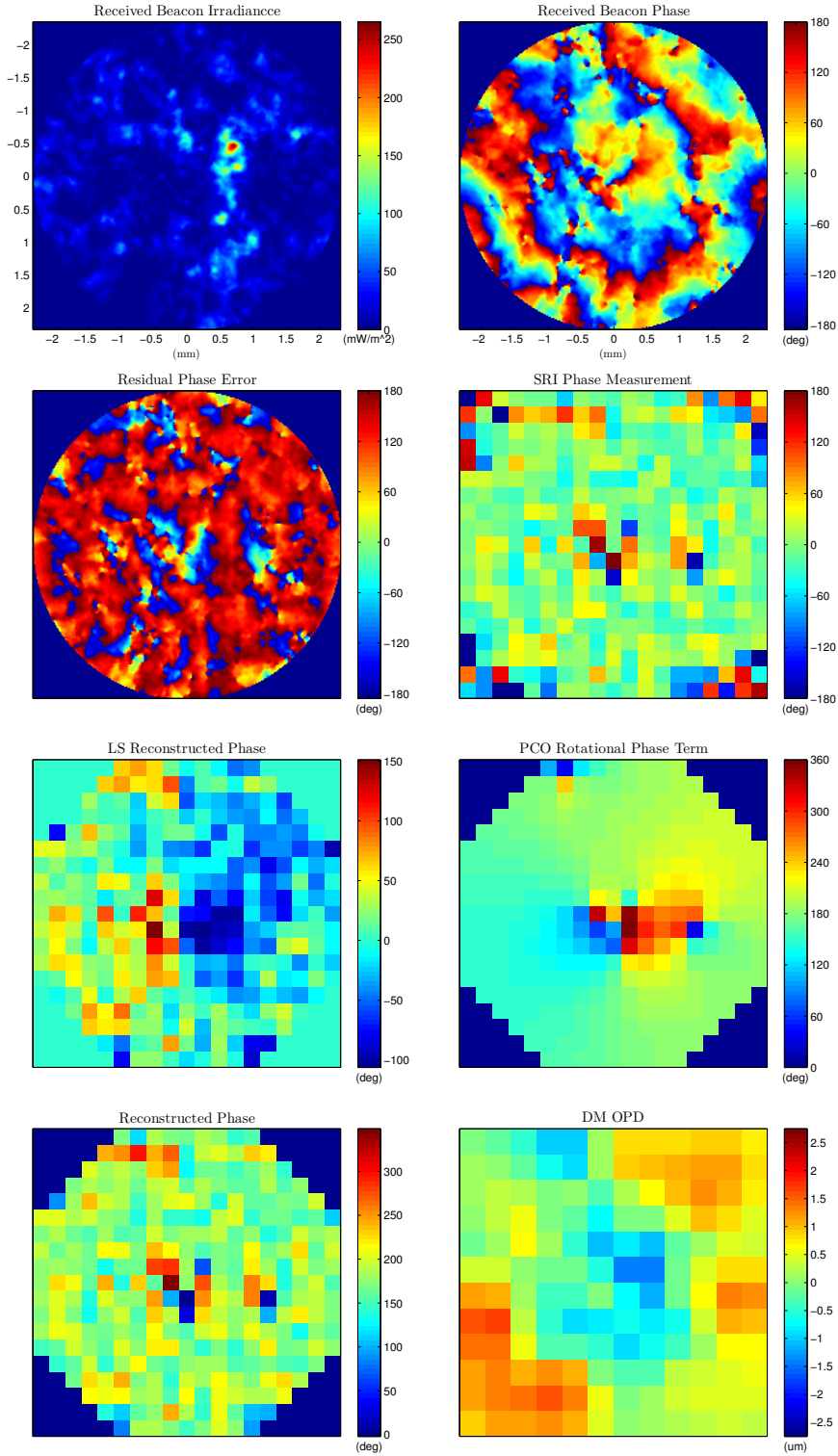


Figure 4.16: AO system state during closed loop operation in conditions of $\sigma_\chi^2 = 0.5$, $d/r_0 = 1$, SNR=60. LSPV+4 is the wavefront reconstructor.

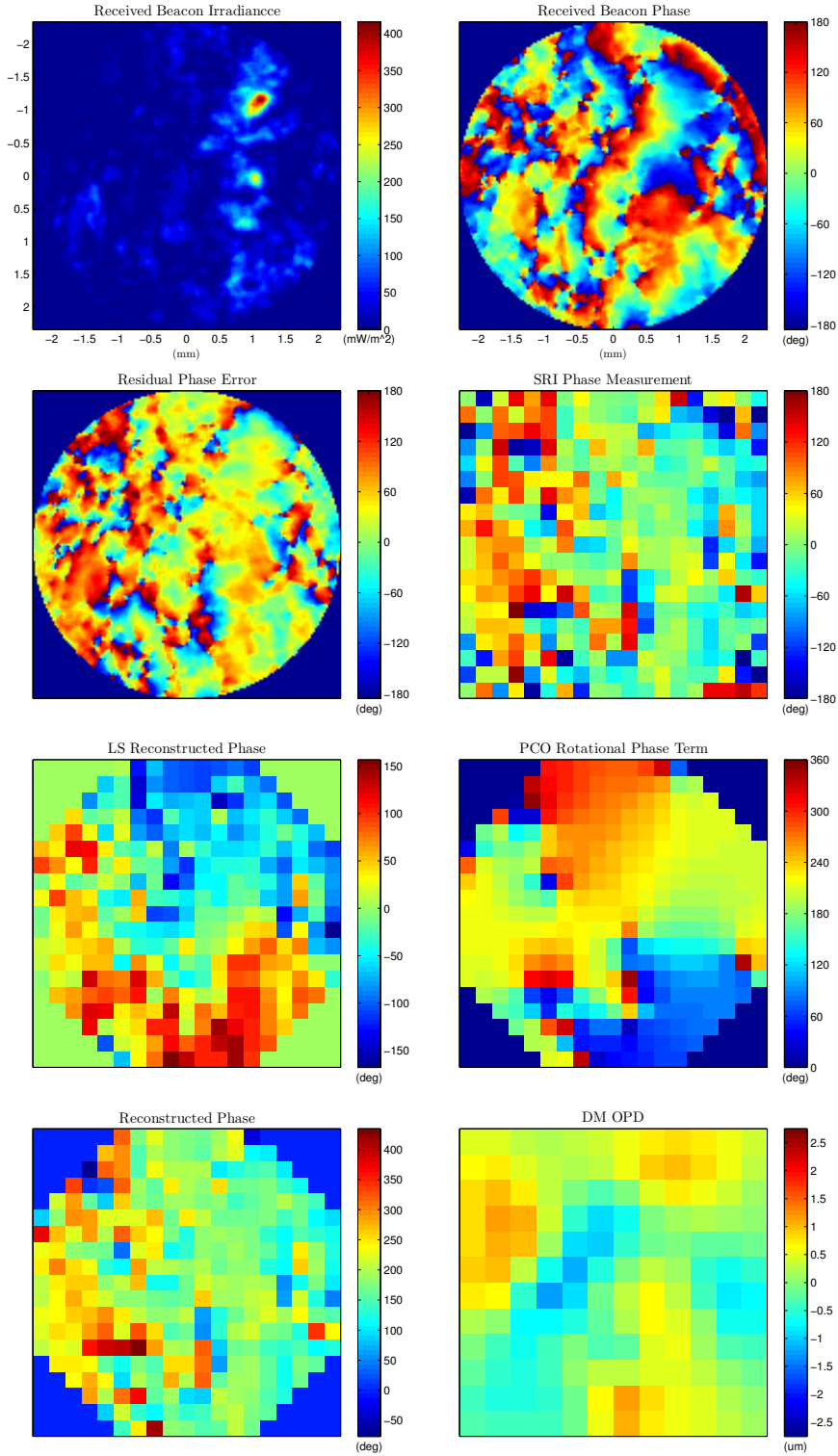


Figure 4.17: AO system state as the higher-order control loop is closing in conditions of $\sigma_\chi^2 = 1$, $d/r_0 = 1$, SNR=60. LSPV+4 is the wavefront reconstructor.

Again, an ideal point source beacon illuminates the turbulent path of interest, with a Rytov number of one. The receive telescope is 40 centimeters in diameter, focused at the beacon distance. An idealistic SRI senses the collimated wavefront (no fiber coupling or noise effects), and an ideal DM applies the appropriate conjugation to the outgoing beam. The ideal DM has no stroke limit, negating the need for a FSM or tracking system. No temporal effects are included in this initial experiment. Instead, unique realizations of turbulent paths are generated, through which the beacon propagates. For each turbulent realization, the AO system senses the field and various reconstruction techniques calculate corrections for the outgoing beam. Each of these pre-compensated beams are then back-propagated through the turbulence to the beacon source plane, where the irradiance patterns are averaged over all turbulence realizations for each reconstruction method. The author acknowledges the lack of temporal effects will not paint a complete picture of expected AO performance. However, this is an important first step to both develop a dual-path test simulation, as well as compare general reconstructor performance in these difficult atmospheric conditions.

The following tests compare reconstruction performance of traditional least squares, LSPV+20 using IWCL as a metric, LSPV+20 using CL as a metric, and Xphase as developed by tOSC. LSPV+20 was chosen instead of LSPV+4 in order to more accurately compare the PCO technique with respect to each metric function. For reference, ideal phase conjugation and ideal field conjugation are also tested. The first round of simulation results is shown in Fig. 4.18. To the author’s initial surprise there was no apparent difference between the ideal phase conjugation, PCO methods, and Xphase. This points out an important point: these reconstruction algorithms all produce modulo- 2π equivalent results, but each uses a different rotational realization in hopes of optimizing placement of any branch cuts with respect to an expected DM fitting error. This initial simulation did not include any DM inter-actuator coupling effects. Further, the SRI and DM were assumed to have the same spatial resolution as the simulated fields themselves. Without any of these

realistic effects, all of the above reconstruction methods gave exactly equivalent results. The poor performance of the least squares reconstruction and great performance of the field conjugations also serve as good sanity checks before moving forward.

The simulation was modified to include realistic SRI sampling and DM parameters (except actuator stroke). As this introduces some subjectivity for the parameters chosen, a range was evaluated to explore the current realistic parameter-space. Inter-actuator couplings of both 10% and 20% were evaluated for DM's of size 10×10 , 19×19 , and 32×32 . The respective SRI subaperture arrays were 19×19 , 37×37 , and 63×63 , again, following the sampling recommendation set by Barchers [6]. The WFS to DM command downsampling method was a matrix operator based on a pyramid convolution three subapertures wide, only considering the active subapertures. The ideal phase and field conjugation methods remain at the full field sampling density for comparison.

Again, 100 realizations of turbulence were run for each of the six DM setups described above. The results of which are shown in Figs. 4.19-4.24. Additionally, Figs. 4.25 and 4.26 provide a visual example of the ‘best’ and ‘worst’ DM fits for an example turbulence realization for each reconstructor. These initial results show some interesting behaviors; although, not all good. Most notably, the 10×10 DM seems to outperform the higher density DM's. Upon reinspection of the simulation code, the AFIT DM setup was used – including a guardband ring of DM actuators which is not used in the higher density DM setups. While it is not definitive that the guardband was the cause for the apparent improved performance, it is a difference that must not be included in future tests. Secondly, the LSPV algorithms and Xphase often show higher peak on-axis power than the ideal phase conjugation. The author hypothesizes this is a result of a constructive interference effect; although, that is only a theory. One final concern upon viewing these results was the varying power levels between each simulation case. In the initial code, the turbulence seeds were set based on the computer clock – resulting in the observed behavior. For future work, the

seeds are now set based on the trial number such that each DM simulation will use the same set of turbulence realizations.

These initial results show the field conjugation performing best and least squares worst. Beyond that, Xphase seems to slightly edge out LSPV+20 IWCL in most cases. Surprisingly, the LSPV+20 using CL as the reconstruction metric underperformed the IWCL metric. The author hypothesizes this is another interference effect at play, but is uncertain on the precise means. However, before making too many conclusions based on the results at hand, the author stresses the flaws pointed out in the preceding paragraph. Further simulations are being conducted to form a better result-set for comparison. Additionally, future simulations including temporal effects are crucial to better understand this problem.

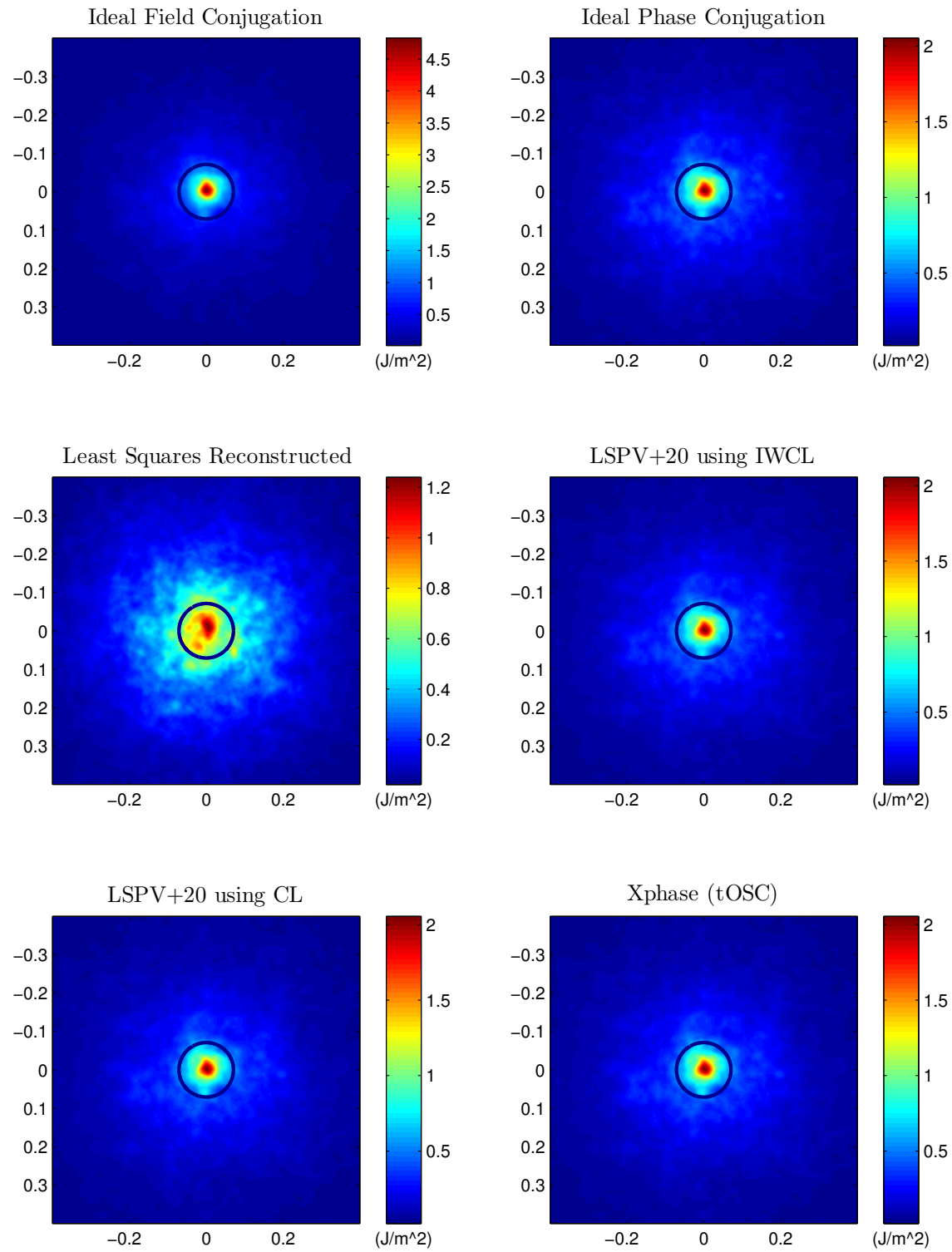


Figure 4.18: Target-plane irradiance patterns, averaged over 100 turbulence realizations with an ideal DM. The central circles show the diffraction limited spot size.

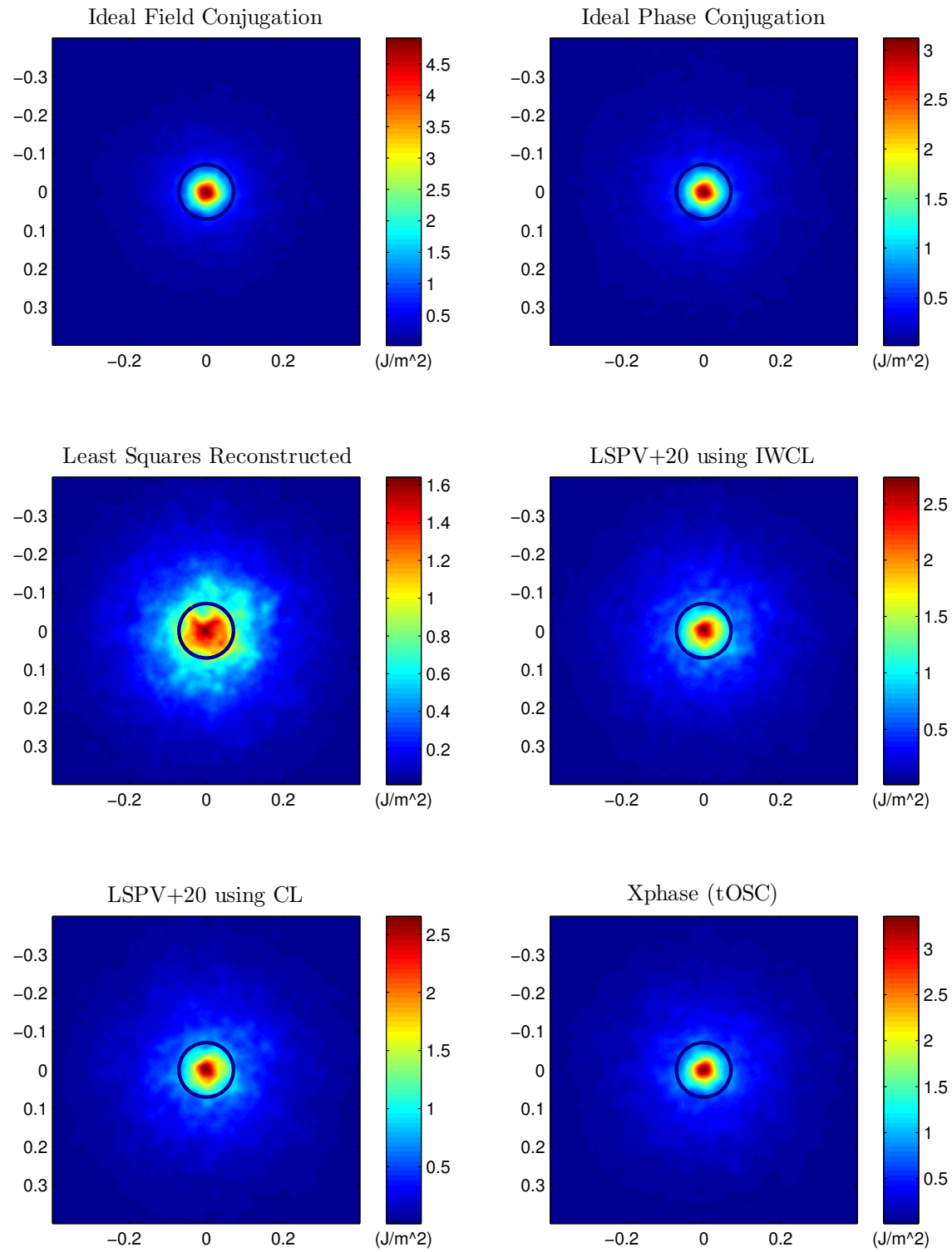


Figure 4.19: Target-plane irradiance patterns using a 10×10 DM with 10% inter-actuator coupling.

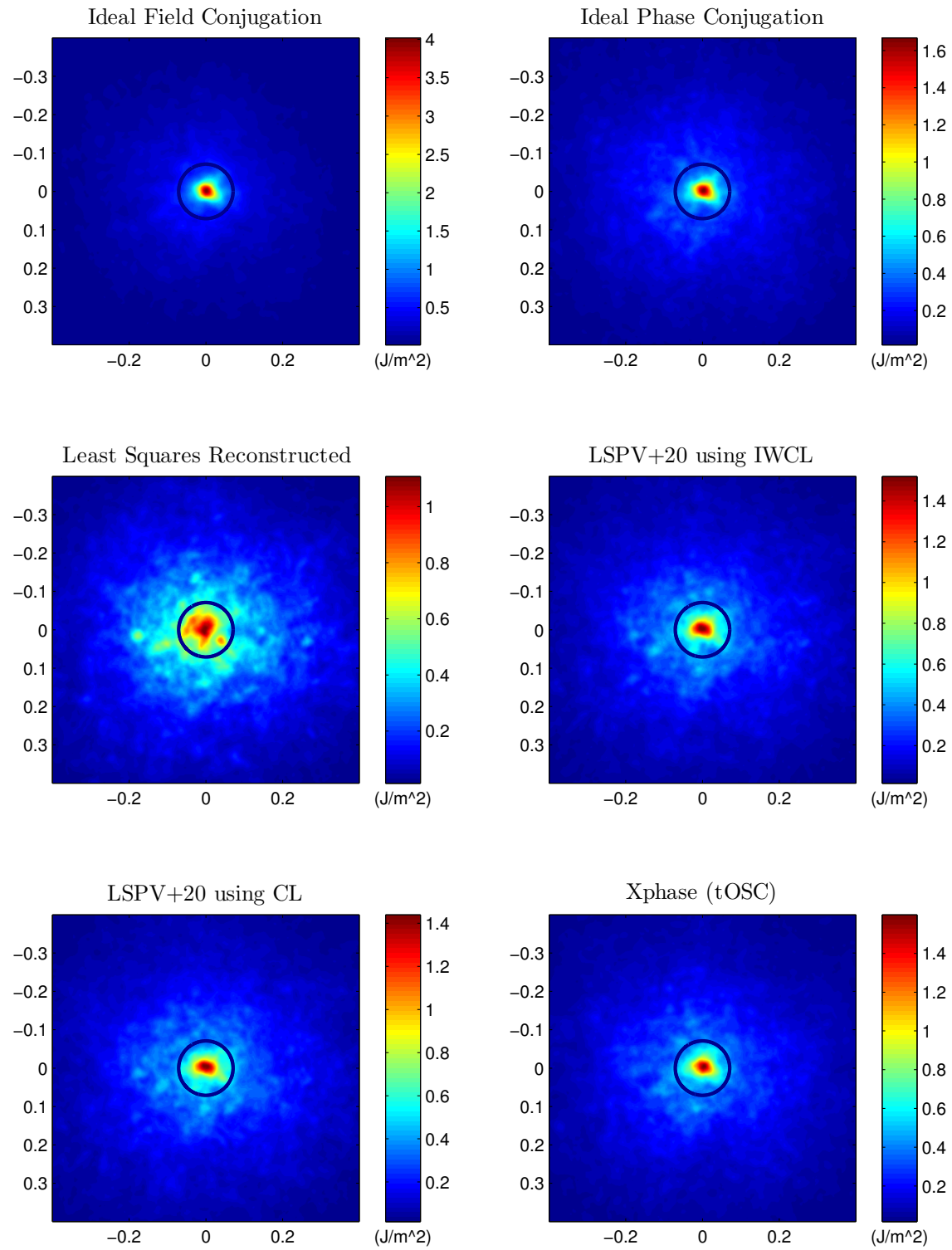


Figure 4.20: Target-plane irradiance patterns using a 19×19 DM with 10% inter-actuator coupling.

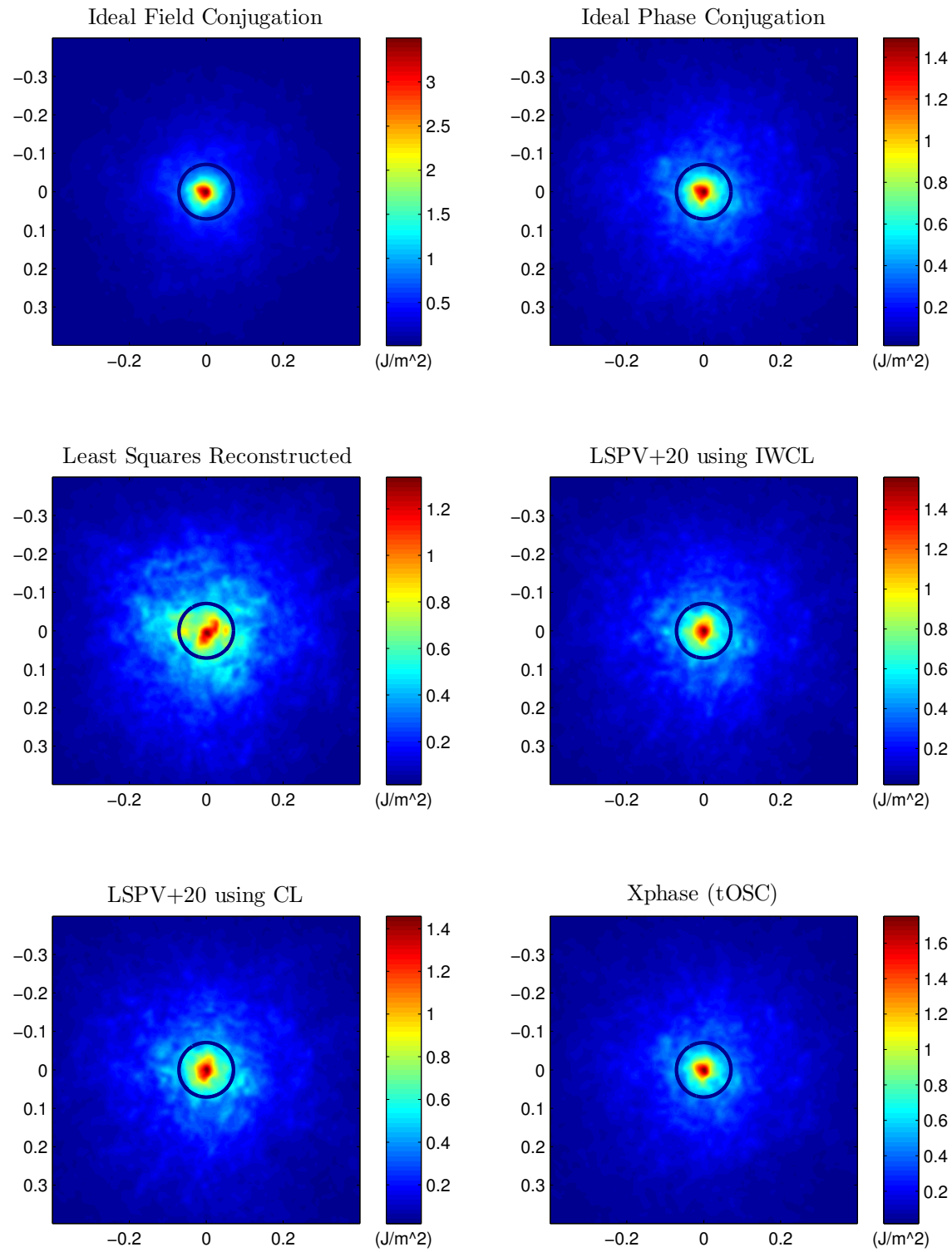


Figure 4.21: Target-plane irradiance patterns using a 32×32 DM with 10% inter-actuator coupling.

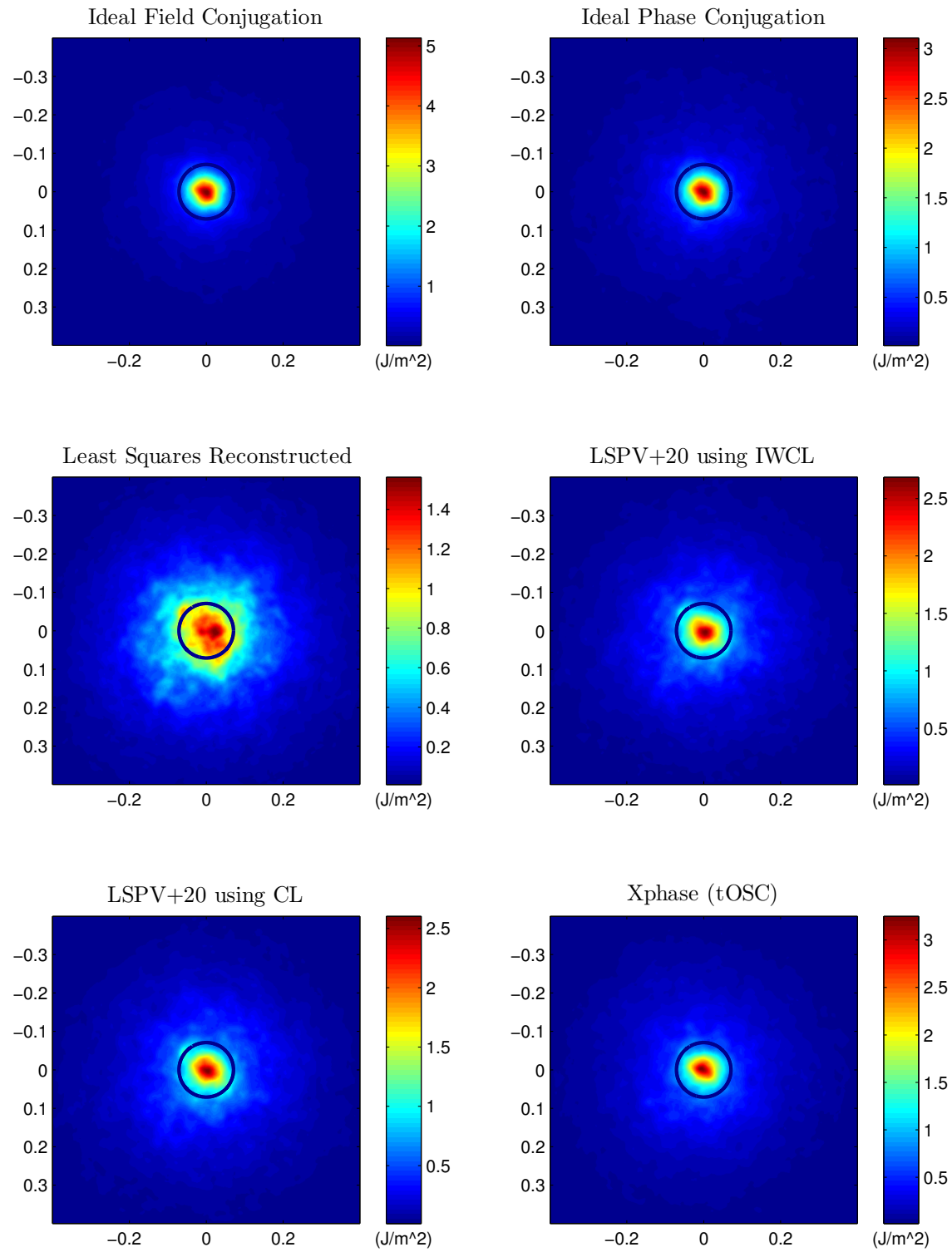


Figure 4.22: Target-plane irradiance patterns using a 10×10 DM with 20% inter-actuator coupling.

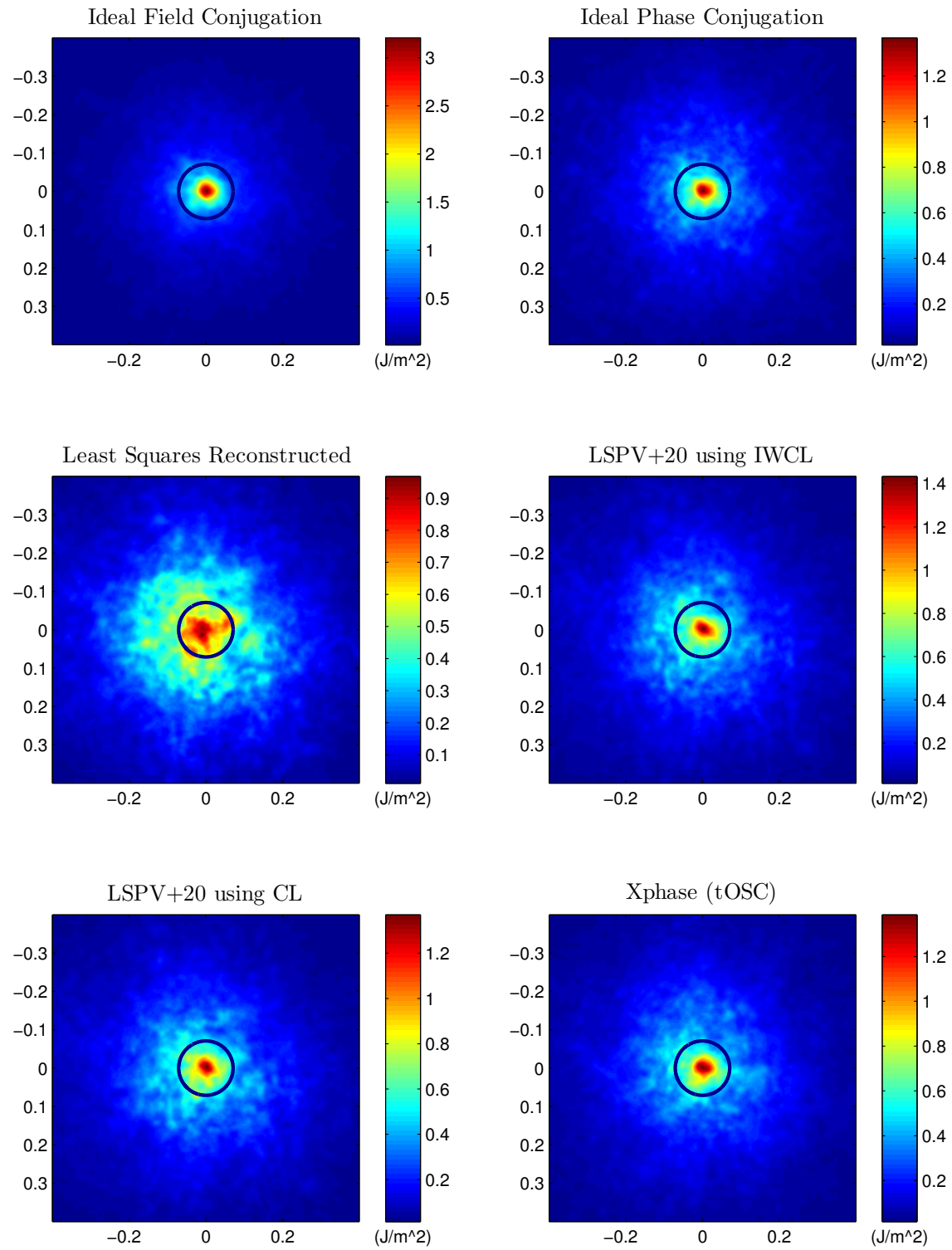


Figure 4.23: Target-plane irradiance patterns using a 19×19 DM with 20% inter-actuator coupling.

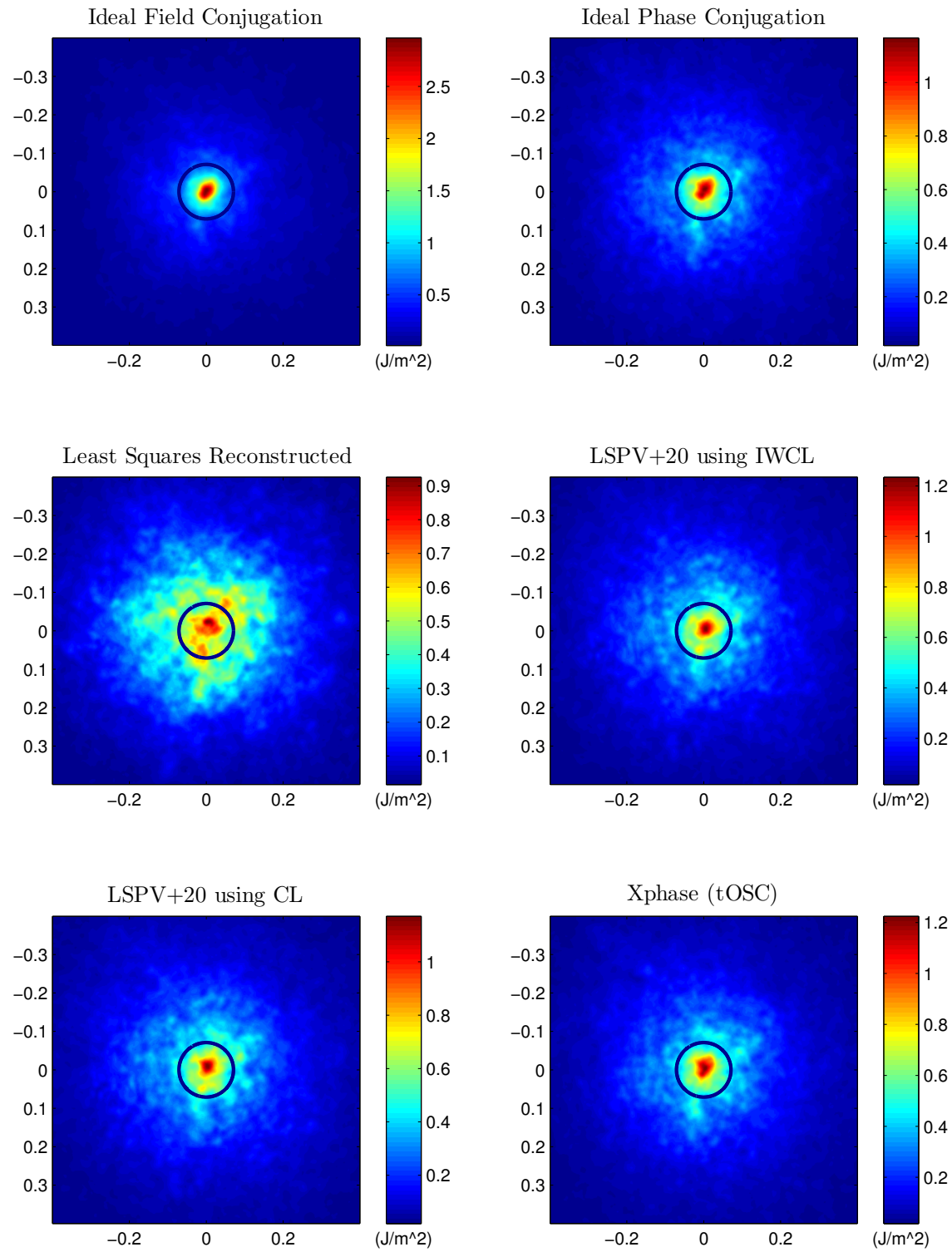


Figure 4.24: Target-plane irradiance patterns using a 32×32 DM with 20% inter-actuator coupling.

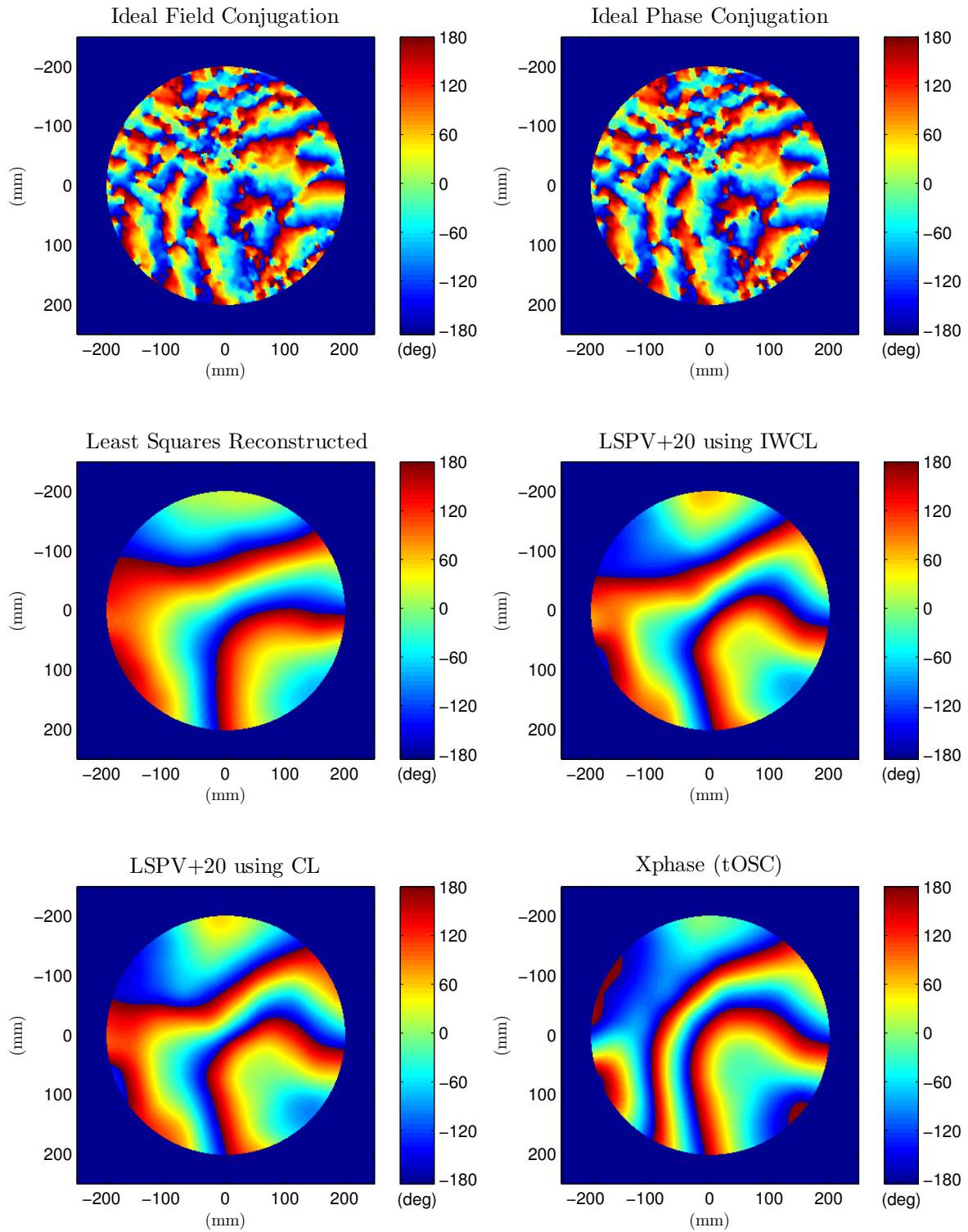


Figure 4.25: Example DM profiles using a 10×10 DM with 20% inter-actuator coupling.

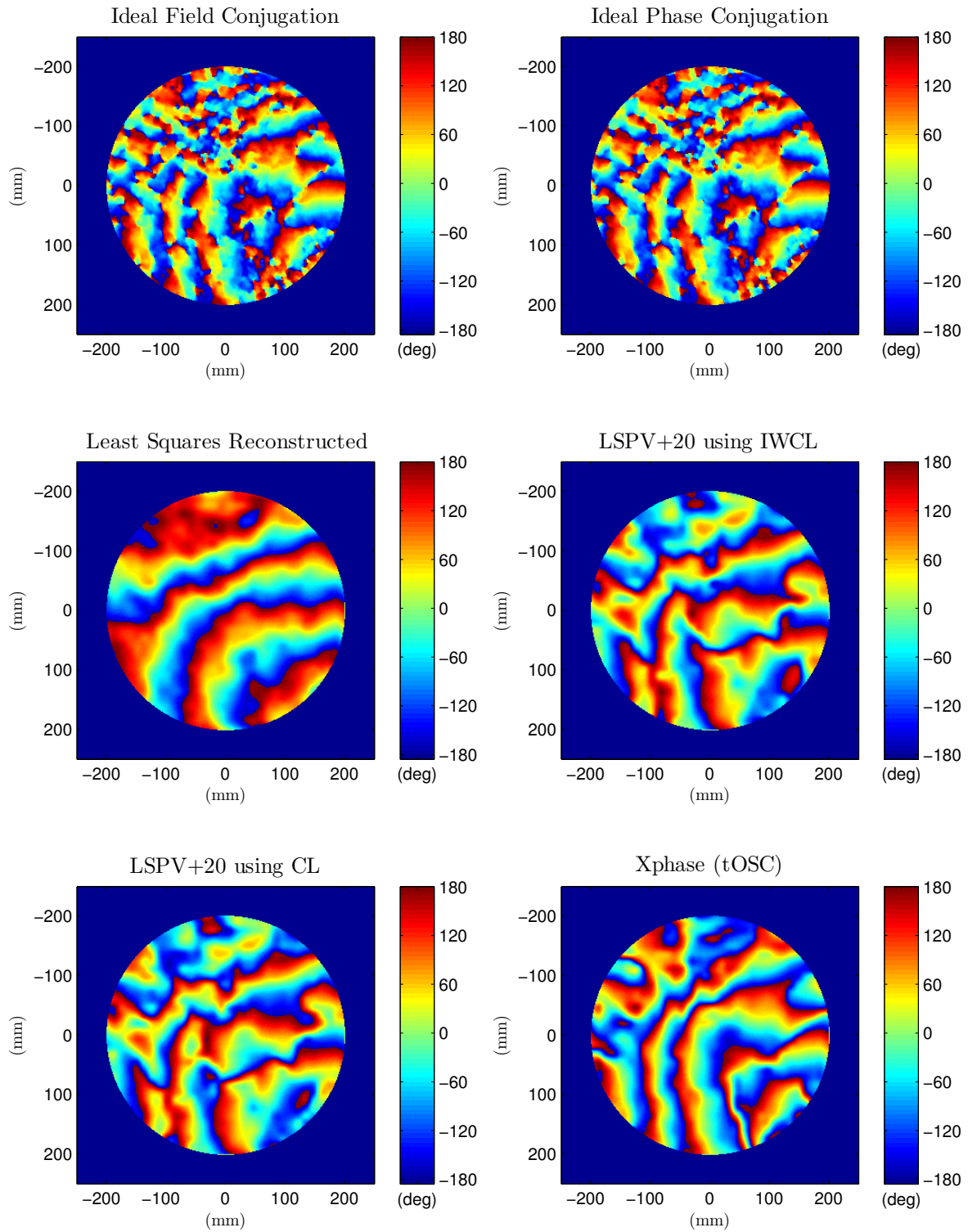


Figure 4.26: Example DM profiles using a 32×32 DM with 10% inter-actuator coupling.

V. Conclusions

This chapter presents a summary of the research completed as part of this Master’s work. Challenges overcome, key results, and future work are given. The research and observations made here build upon the previous work of Pellizzari and Schmidt, where this effort was aimed at transitioning their research towards a realistic implementation. In doing so, many new discoveries were made in the hopes of extending current AO capabilities in strong turbulence regimes.

5.1 Challenges Overcome

- *Developed realistic AO system model.* This was the crucial next step from the previous research. A realistic SRI model was developed, incorporating frame-by-frame fiber coupling effects, a first of its kind for this research. System radiometry was modeled, allowing for meaningful shot noise, sensor read noise, and quantization noise effects. Care was given to correctly model the independent tilt and higher-order control systems, including the complete higher-order data processing pipeline. In doing so, data-flow optimizations were made specific to PCO-based wavefront reconstruction and AO control.
- *Complex, multi-dimensional parameter space.* This research analyzed effects of Rytov number, Fried’s parameter, Greenwood frequency, and SNR for each wavefront reconstructor tested. This five dimensional parameter space created hundreds of gigabytes of simulation results which had to be efficiently tracked and managed. Running the simulations to explore the complete parameter space took weeks, even utilizing several high performance computers. Given the simulation requirements, significant development effort was given to optimize code. This framework is now available for future research.

- *Bring AFIT AO hardware to an operational state.* As this research began, AFIT’s AO system was plagued with a variety of issues that led to unreliable performance. Working in conjunction with the primary contractor, the author assisted in finding, diagnosing, and correcting a number of software and hardware issues. The author learned LabVIEW in order to become proficient with the hardware interfacing and control code. Since no manuals were available, the author learned and wrote quick guides for common procedures. A full-system optical alignment procedure was developed, reducing the time required from 12 hours to only two. Unfortunately, at the final stages of this research a circuit board failure rendered the DM inoperable before any meaningful data could be taken. Initial AO system characterization results were presented at the 2011 SPIE Defense, Sensing, and Security conference.
- *Developed an ATS configuration change to allow high-Rytov simulations.* In the configuration from the contractor, the ATS could simulate high-Rytov number conditions but only with prohibitively small r_0 ’s. In the simulations performed the ratio of DM actuator spacing to r_0 was kept, at most, to one. However, in the original configuration, the ATS could not maintain that ratio at $\sigma_x^2 = 1$. The author developed an optical modification that would allow much greater emulation capabilities in the $r_0 : \sigma_x^2$ parameter space of interest to this research.

5.2 Key Results

- *Demonstrated greatly improved strong turbulence AO performance in terms of both mean Strehl and Strehl variance.* The AO performance gains using a PCO wavefront reconstructor over the traditional least squares reconstructor in terms of mean field estimated Strehl ratio and Strehl ratio normalized standard deviation are summarized in Table 5.1. Mean Strehl is a metric of absolute AO correction performance (higher is better), and the Strehl standard deviation is a metric of correction stability (lower is better). These results were presented at the 2012 IEEE Aerospace conference.

Table 5.1: Aggregate AO performance gains of all PCO-based wavefront reconstructors over the traditional least squares reconstructor.

σ_x^2	Mean Strehl	Normalized Strehl Standard Deviation
0.04	0.2%	-2.4%
0.5	19.1%	-50.6%
1	126.4%	-57.6%

- *Further reconstructor comparison under more realistic conditions.* It turns out LSPV+1 is hard to beat in terms of performance gain relative computations required in most cases. However, as the Rytov number increases above roughly 0.5, a broader search becomes important as the PDF of h_{opt} was shown to broaden. The simplicity of LSPV+4 with very similar performance to the more advanced reconstruction algorithms proposed by Pellizzari make it a good choice in high-Rytov conditions.
- *Identified cause of fades from PCO-based AO and demonstrated a potential solution.* When in closed-loop operation in strong turbulence, PCO algorithms can cause short-term fades as h_{opt} varies. These drops in Strehl are not caused by the higher-order control law as much as different tilt components associated with each PCO rotational realization. The tilt is removed from the higher-order corrections and instantly dumped on the tracking system; causing the fades. One solution was found by allowing tilt in the higher-order corrections with conservative controller gains. This prevented the fades with a slight tradeoff in mean Strehl ratio. Unfortunately, a realistic system with slight misalignments would require a zero-DC-gain control law to implement a similar solution. Additionally, this puts higher stroke requirements on the DM when tilt is being included. With this new understanding future work in control design could help mitigate these fades based on the application requirements.

- *Demonstrated and developed theory on improved PCO performance in weak turbulence, low SNR regimes.* In weak turbulence, where no branch points are present, a consistent performance improvement of the PCO reconstructors over traditional least squares was found. Although the difference is small, this was completely unexpected based on previous concerns of noise corrupting the PCO process. A new theory proposed by the author shows in high-noise conditions, least squares reconstructors can introduce phase anomalies to the AO corrections. However, the PCO process removes these phase discrepancies introduced by the least squares reconstruction. These findings will be presented at the 2012 SPIE Optics and Photonics conference.
- *Developed a set of theories regarding phase anomalies in high wavefront gradient conditions.* When localized wavefront phases being reconstructed from an SRI are greater than π radians between adjacent subapertures, the least squares reconstructor will alias, leading to a phase anomaly in the reconstructed field. This can be mitigated using a higher density of SRI subapertures, at the cost of SNR. Alternatively, initial results show the PCO corrects the phase anomalies introduced by the least squares reconstruction.
- *Formulated an optimized data flow for an AO system using PCO.* Started by diagnosing coupling between the high-order and tracking control systems when using a PCO-based wavefront reconstructor. Since PCO reconstruction is not a single matrix operation, decoupling tilt from the higher-order commands required a new data flow process. The resulting process, illustrated in Fig. 3.4, minimizes matrix multiplies while maximizing AO effectiveness.
- *Conducted first beam projection simulations using PCO wavefront reconstruction techniques.* Conducted at the end of this research, this establishes a foundation

for future efforts to investigate these novel reconstruction methods with respect to beam projection applications. Although the initial simulation results identified needed changes, initial observations indicate promise over traditional least squares reconstruction. The identified flaws have since been fixed and follow-up simulation results will be presented at the 2012 DEPS Beam Control Conference.

- *Extensible AFIT AO system model for future research.* The model is configurable to varying levels of realism and AO capabilities. Allows isolation of the research problem at hand without the difficulties of hardware work and the assumptions of analytical work. This includes the first modeling of realistic fiber coupling to our specific SRI optical setup – crucial to realistic noise modeling.

5.3 Future Work

- *Hardware verification of simulation results.* Unfortunately, the DM amplification circuit board failed prior to beginning hardware testing and verification of the simulation work presented here. This will be an essential step forward in verifying all theories formulated thus far regarding PCO-based wavefront reconstruction and control.
- *Hardware verifications using real atmospheric turbulence.* Following hardware verification in the lab, the next step would be to test out the system performance using real atmospheric turbulence. As the realism is increased, new challenges are often discovered and additional validity is given to the theory.
- *Additional verification of phase anomaly theories.* A set of initial simplified tests were made to form the theories presented on phase anomalies. More rigorous testing to relate the theories to more realistic scenarios is needed.
- *Further investigation into a practical tilt coupling between the control systems to reduce fades.* A more in-depth consideration of the tilt coupling effects between

the tracking system and a higher-order system implementing a PCO wavefront reconstructor is needed. A zero-DC-gain controller is required to account for realistic component misalignments, which was not implemented here. Another alternative could be a feed-forward tilt-offloading between the two control systems as h is varied.

- *Investigate adaptive controlling techniques with a PCO-based reconstructor.* Promising improvements in AO performance by Gibson [26] and Poyneer [32] using adaptive AO control have been applied towards traditional weak turbulence techniques. Investigation as to whether these algorithms would work with the PCO non-unique rotational phase component would be needed.
- *Effects of SRI performance with respect to platform vibrations.* Moving the SRI out of a lab setup could reduce the fringe stability and thus the fidelity of the initial SRI wrapped measurements. This could be crudely simulated by disturbing the lab bench without requiring transportation of the system outside the lab.
- *Further previous work on the hybrid SRI–Shack-Hartmann WFS using the simulation model created here.* The simulation model developed as part of this research would be an excellent and easily extended platform on which to further previous work in designing an effective hybrid WFS. This may involve dynamic power splitting, comparative wavefront reconstruction, and more complex control techniques. The range of investigations and potential improvements are extensive, and this would be the first detailed test of a realistic implementation without the issues involved in full hardware integration.
- *Further thought into IWCL and CL metrics in the PCO algorithms that operate over the residual phase error, as opposed to the fully aberrated field.* In steady-state closed loop operation, the wavefront reconstructors do not observe the fully aberrated beacon phase. Rotational phase effects, including branch cuts, will be of

reduced visibility – often to the point where the branch cuts are below the threshold for detecting them at all. Only as the turbulence evolves in time are features visible, yet still not completely visible. These metrics do improve PCO performance with respect to the aliasing phase anomalies, but the author questions whether this is the best way to evaluate the “goodness” of a particular reconstruction when operating in closed loop.

Appendix A: Detailed Simulation Results

The following plots show the compiled simulation results for each reconstructor over all conditions tested. Each grid-point represents a simulated one second AO run. Note that the simulations with higher Greenwood frequencies will run over many more Greenwood periods than the lower Greenwood frequency cases. Unfortunately, it would have been computationally prohibitive to run all of the low-Greenwood cases long enough to hold the number of Greenwood periods constant. While this is a definite compromise, I think the usefulness of the results is still strong.

The left column is the mean field-estimated Strehl, calculated from after the higher-order control system is enabled through the end of each simulation run. The right column shows normalized standard deviation of the prior field-estimated Strehl ratio. This second statistic provides an idea for the system stability, where lower is better. The color axes have been fixed for each section below for easier comparison.

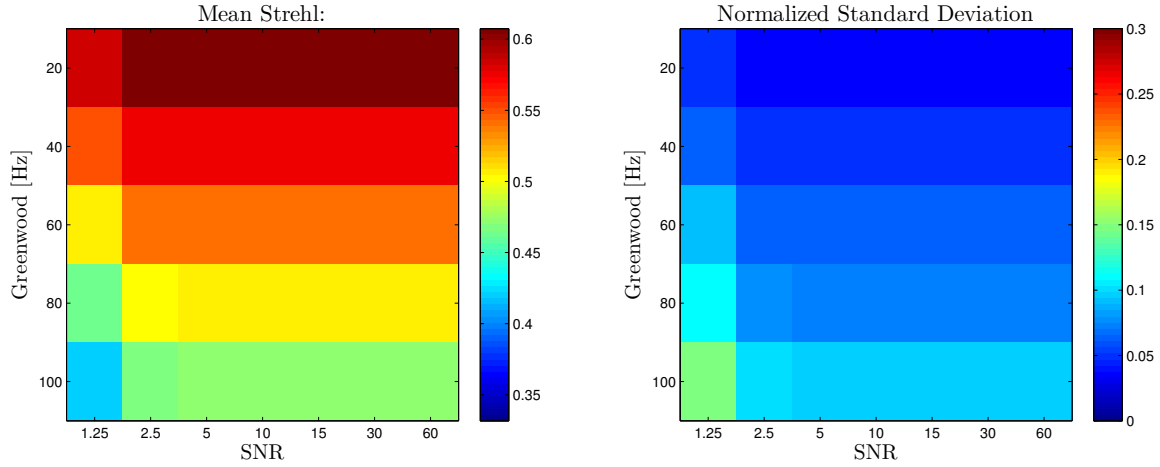


Figure A.1: Least-Squares Reconstructor. Weak Turbulence: $\sigma_\chi^2 = 0.04$, $d/r_0 = 1$

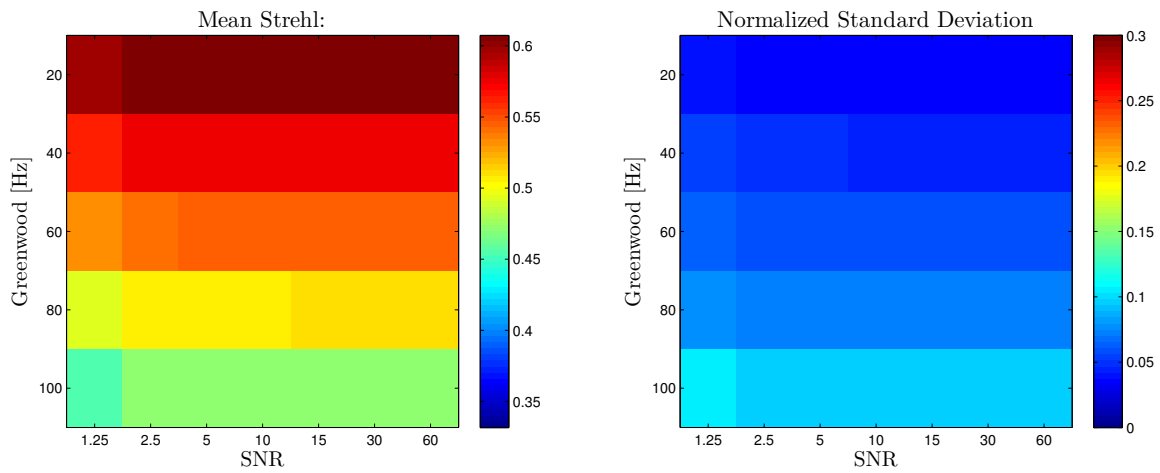


Figure A.2: LSPV+1 Reconstructor. Weak Turbulence: $\sigma_\chi^2 = 0.04$, $d/r_0 = 1$

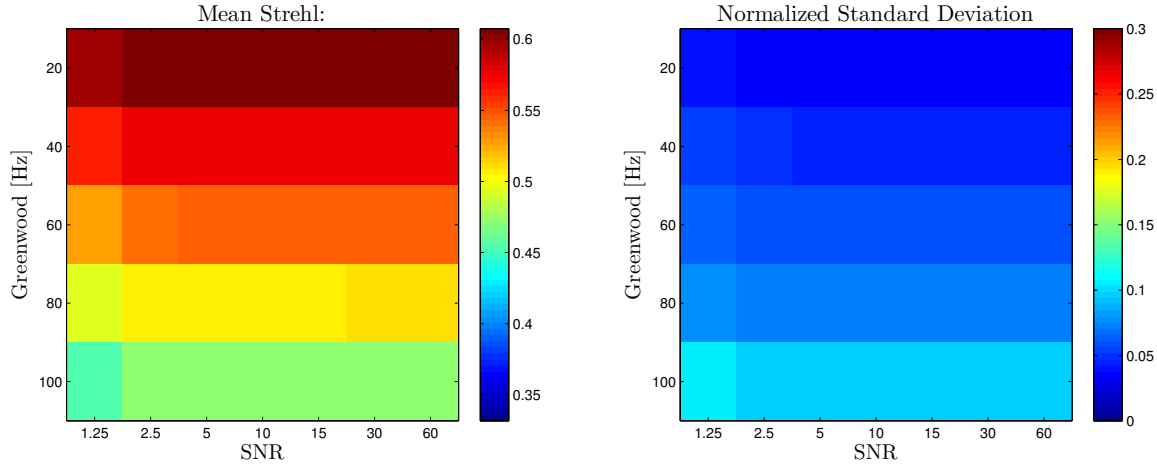


Figure A.3: LSPV+4 Reconstructor. Weak Turbulence: $\sigma_\chi^2 = 0.04$, $d/r_0 = 1$

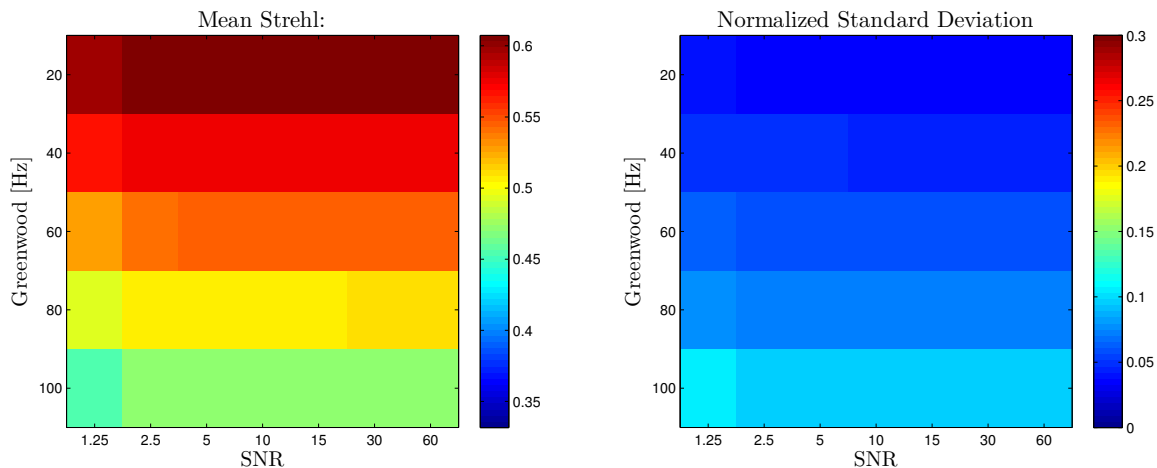


Figure A.4: Histogram Reconstructor. Weak Turbulence: $\sigma_\chi^2 = 0.04$, $d/r_0 = 1$

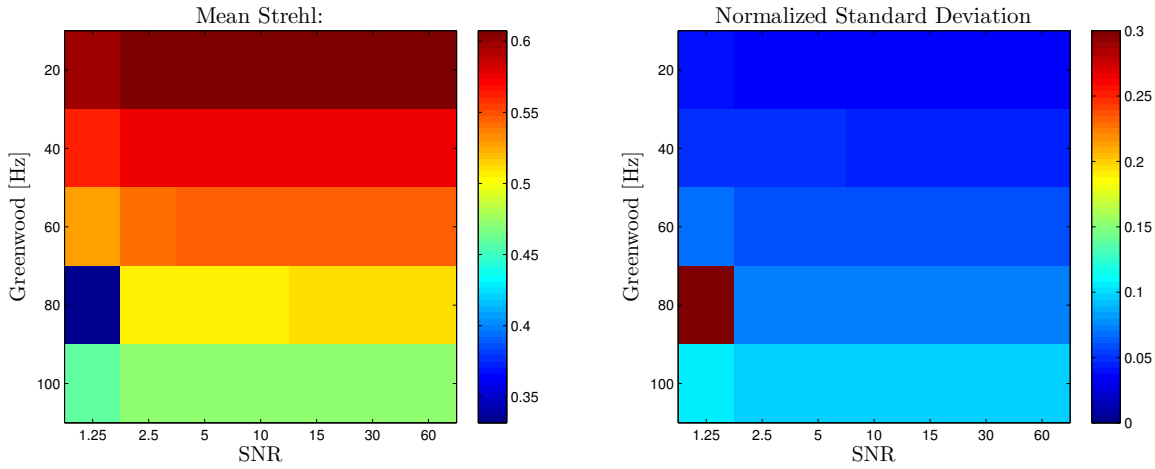


Figure A.5: Iterative Probing Reconstructor. Weak Turbulence: $\sigma_\chi^2 = 0.04$, $d/r_0 = 1$

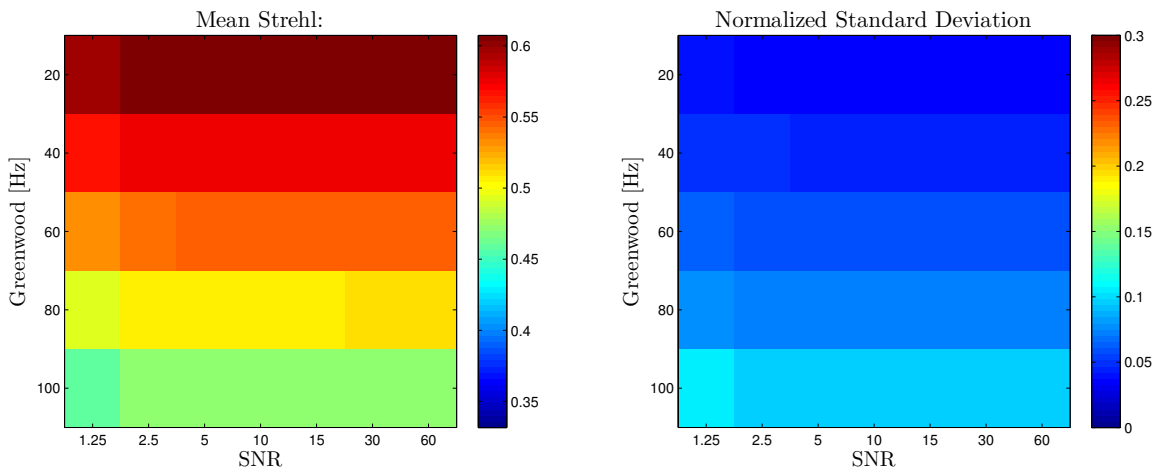


Figure A.6: Golden-Ratio Reconstructor. Weak Turbulence: $\sigma_\chi^2 = 0.04$, $d/r_0 = 1$

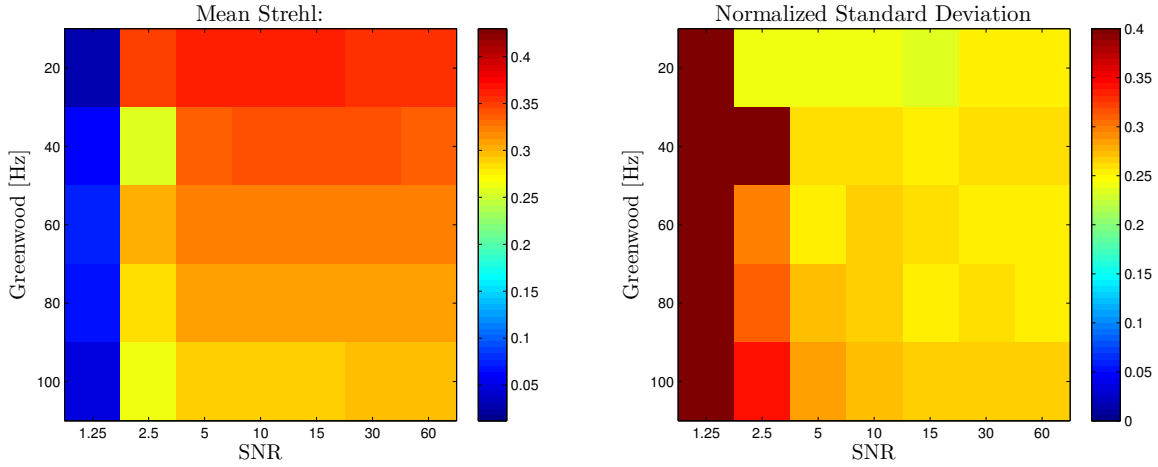


Figure A.7: Least-Squares Reconstructor. Medium Turbulence: $\sigma_\chi^2 = 0.5$, $d/r_0 = 1$

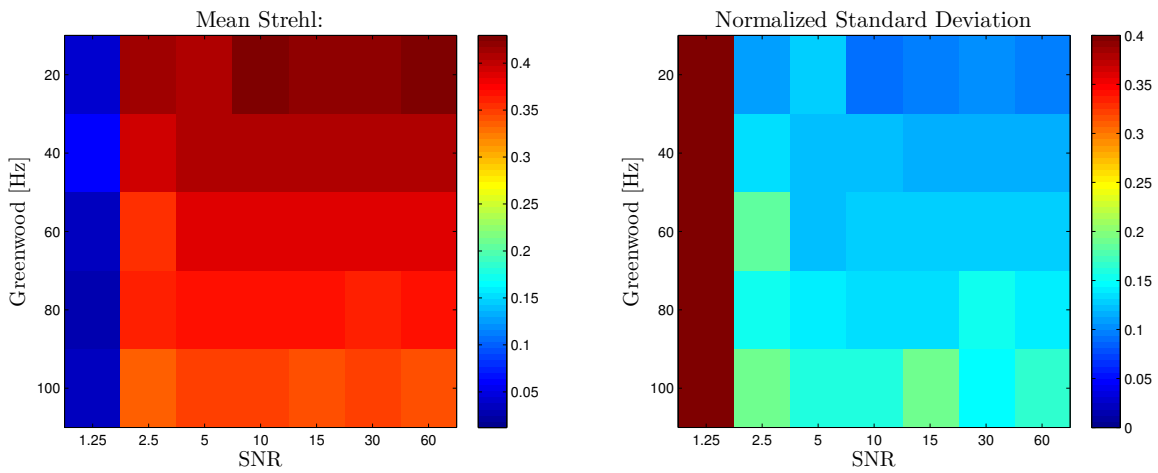


Figure A.8: LSPV+1 Reconstructor. Medium Turbulence: $\sigma_\chi^2 = 0.5$, $d/r_0 = 1$

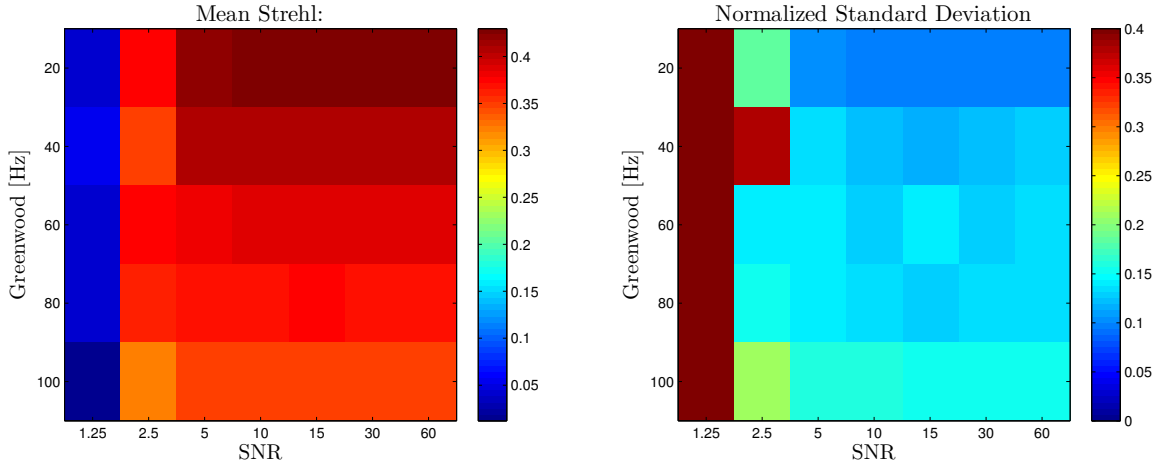


Figure A.9: LSPV+4 Reconstructor. Medium Turbulence: $\sigma_\chi^2 = 0.5$, $d/r_0 = 1$

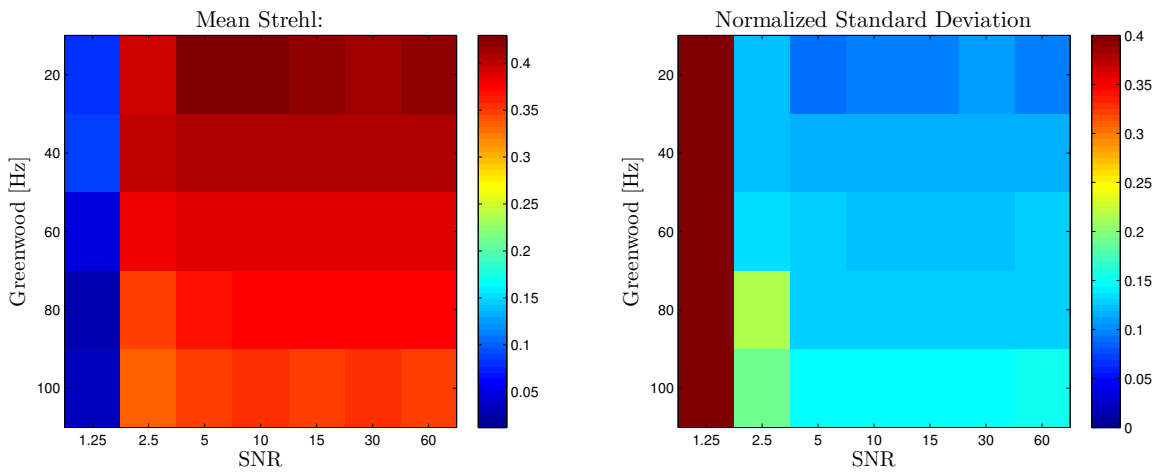


Figure A.10: Histogram Reconstructor. Medium Turbulence: $\sigma_\chi^2 = 0.5$, $d/r_0 = 1$

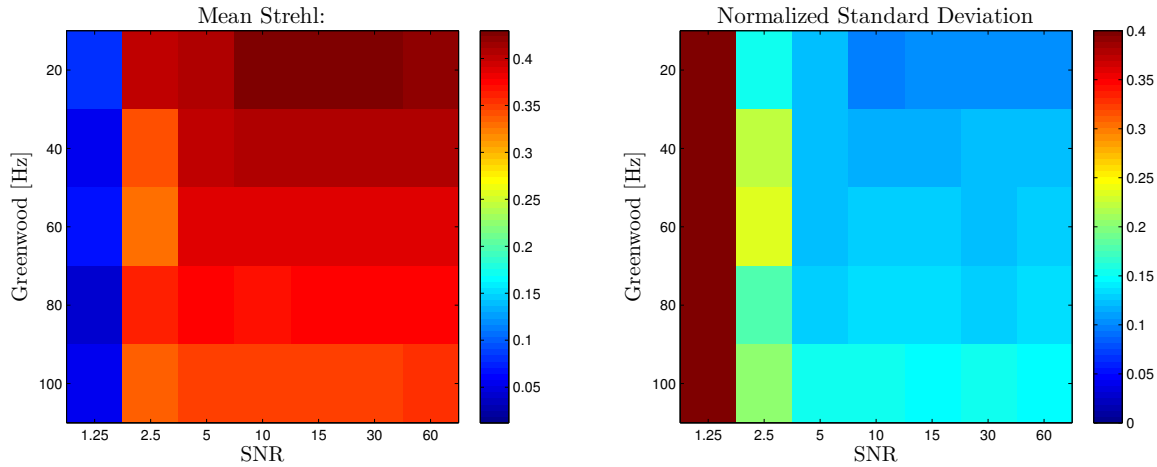


Figure A.11: Iterative Probing Reconstructor. Medium Turbulence: $\sigma_\chi^2 = 0.5$, $d/r_0 = 1$

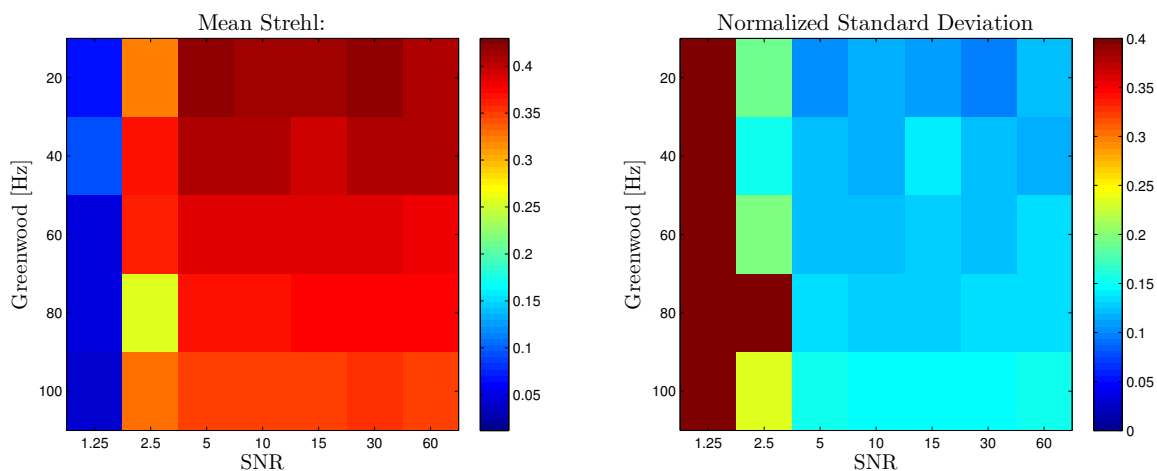


Figure A.12: Golden-Ratio Reconstructor. Medium Turbulence: $\sigma_\chi^2 = 0.5$, $d/r_0 = 1$

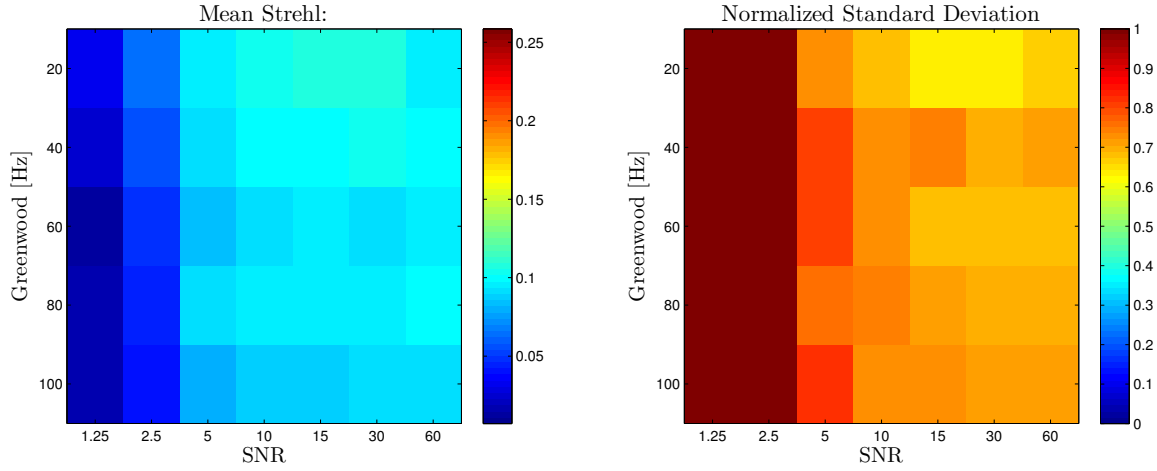


Figure A.13: Least-Squares Reconstructor. Strong Turbulence: $\sigma_\chi^2 = 1$, $d/r_0 = 1$

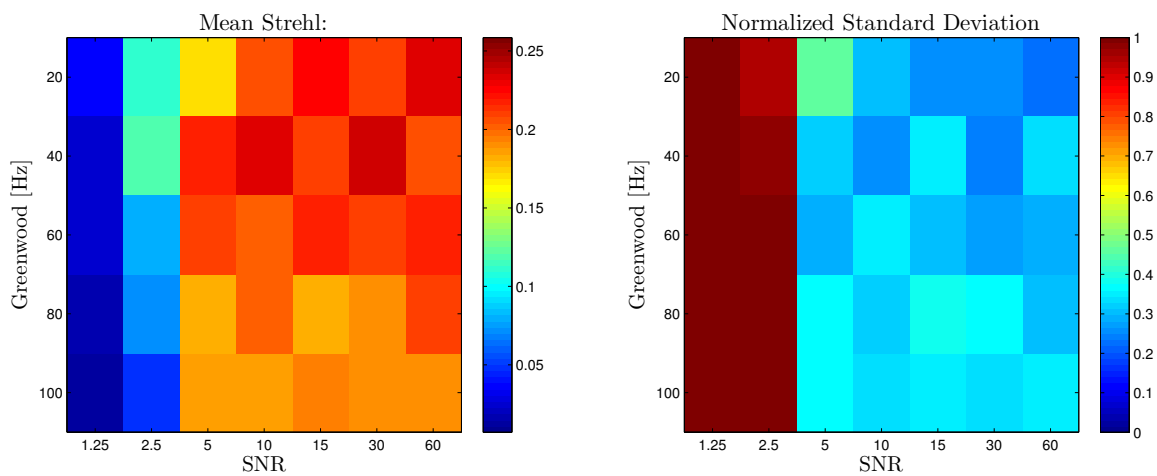


Figure A.14: LSPV+1 Reconstructor. Strong Turbulence: $\sigma_\chi^2 = 1$, $d/r_0 = 1$

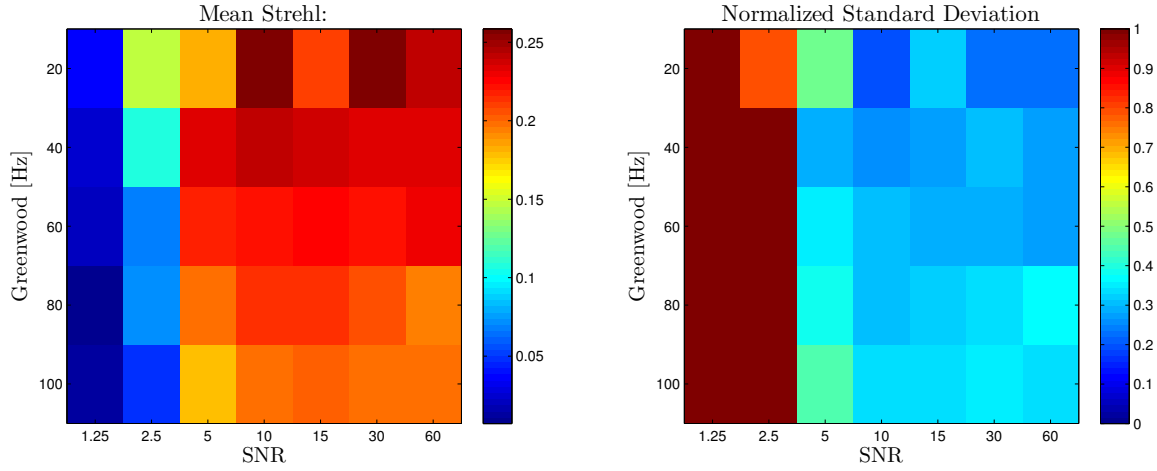


Figure A.15: LSPV+4 Reconstructor. Strong Turbulence: $\sigma_\chi^2 = 1$, $d/r_0 = 1$

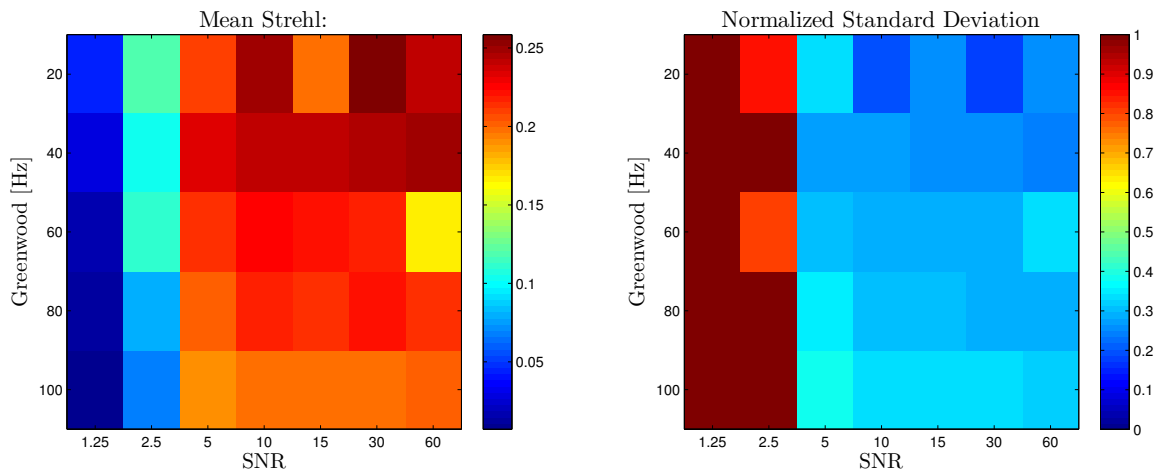


Figure A.16: Histogram Reconstructor. Strong Turbulence: $\sigma_\chi^2 = 1$, $d/r_0 = 1$

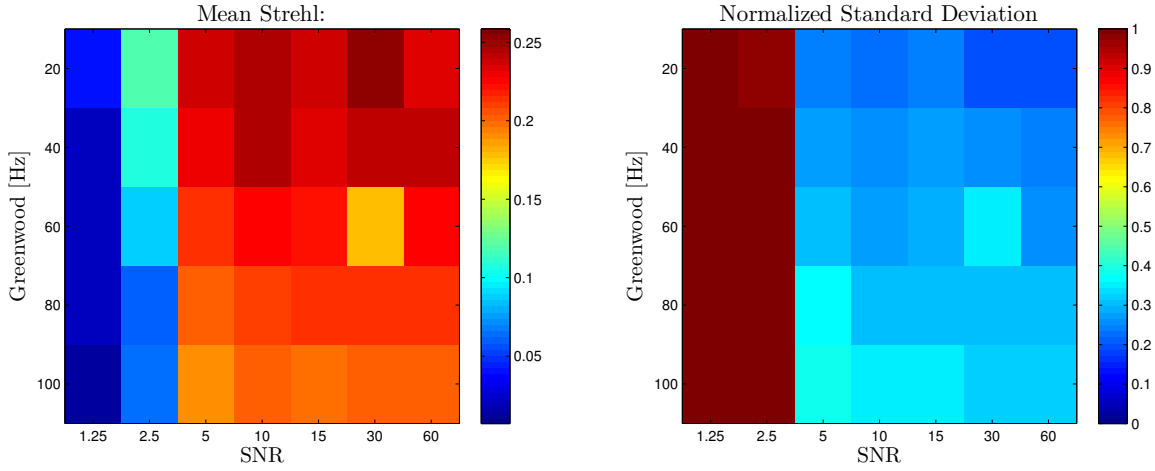


Figure A.17: Iterative Probing Reconstructor. Strong Turbulence: $\sigma_\chi^2 = 1$, $d/r_0 = 1$

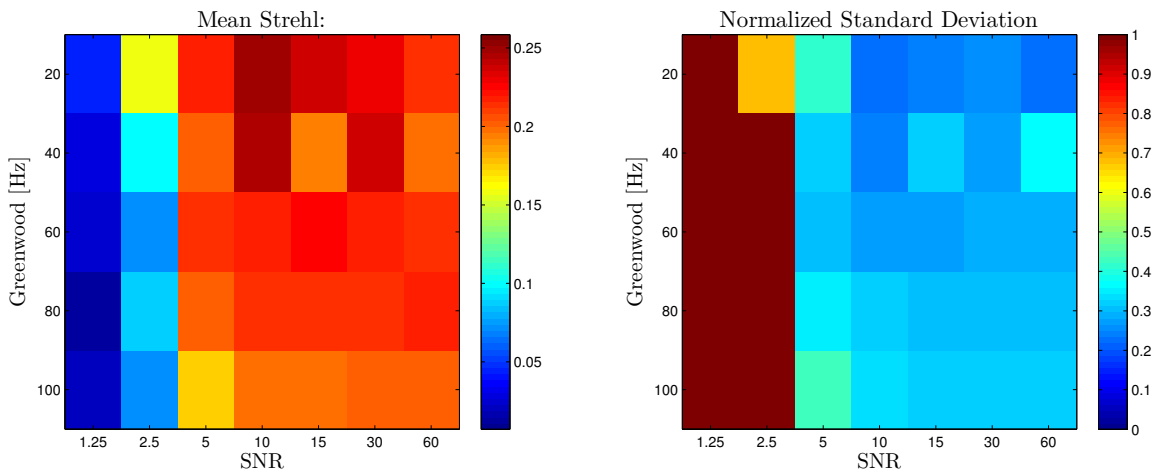


Figure A.18: Golden-Ratio Reconstructor. Strong Turbulence: $\sigma_\chi^2 = 1$, $d/r_0 = 1$

Appendix B: PCO Rotational Phase Tilt Propagation

This appendix presents a simple simulation tracing a rotational wavefront through the higher-order data path. It is related to how the tracking system perceives the wavefront tilt both before and after the higher-order corrections are applied.

The simulation starts with the rotational phase shown in Fig. B.1, with a uniform irradiance across the entire field. For this example, the wavefront sensor is idealized, giving no sensing errors or noise effects. The least squares reconstruction is also shown and is mostly flat as discussed in Sec. 2.3. Note that to the tracker, the rotational phase does not have any tilt. Figure B.2 shows the tracker spot for the uncorrected input field. It has a doughnut-like shape, but it is centered on the sensor array.

The four PCO rotational reconstructions are plotted in Fig. B.3. In each rotational realization, a tilt component is defined by the location of the branch cut. It is important to distinguish this tilt component from the tilt component viewable by the tracker. The tilt component with respect to the higher-order system is defined by the tilt-removal operator from Sec. 3.1.1. To this operator, each rotational realization has a tilt component as shown in Fig. B.4. The tilt-removal operator is applied to all four rotational realizations, and the resulting outputs are applied to a DM. Sending the original rotational field onto each DM realization, and then looking again at what the tracker would see exposes an apparent shift in each of the tracker spots. Figure B.5 plots each tracker output. Note that the spots are no longer doughnut-like, so the higher-order phase aberrations were correctly compensated. However, the tilt components removed from each rotational realization, not only are visibly different, but they clearly propagate to the tracking system. Unfortunately, it does take a finite amount of time for the tracking system to react to these changes. That is the cause of the fades when h_{opt} changes in a high Rytov environment.

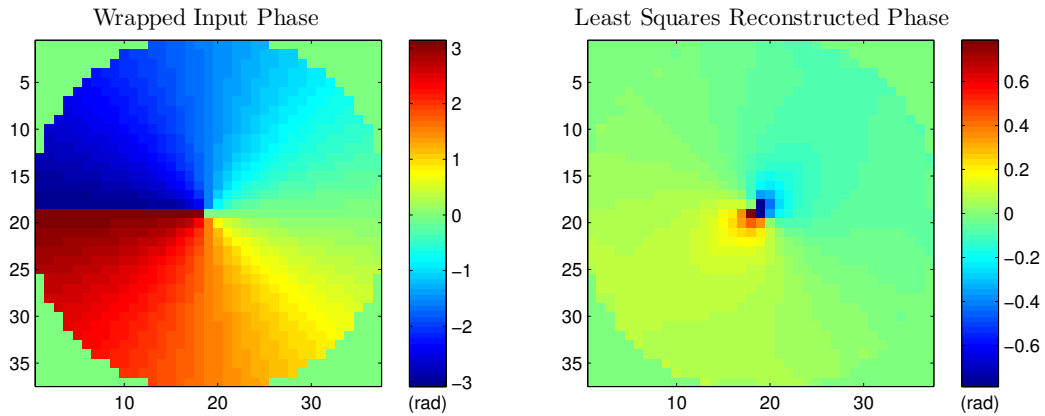


Figure B.1: A hypothetical rotational phase (left), and its corresponding least squares reconstruction (right).

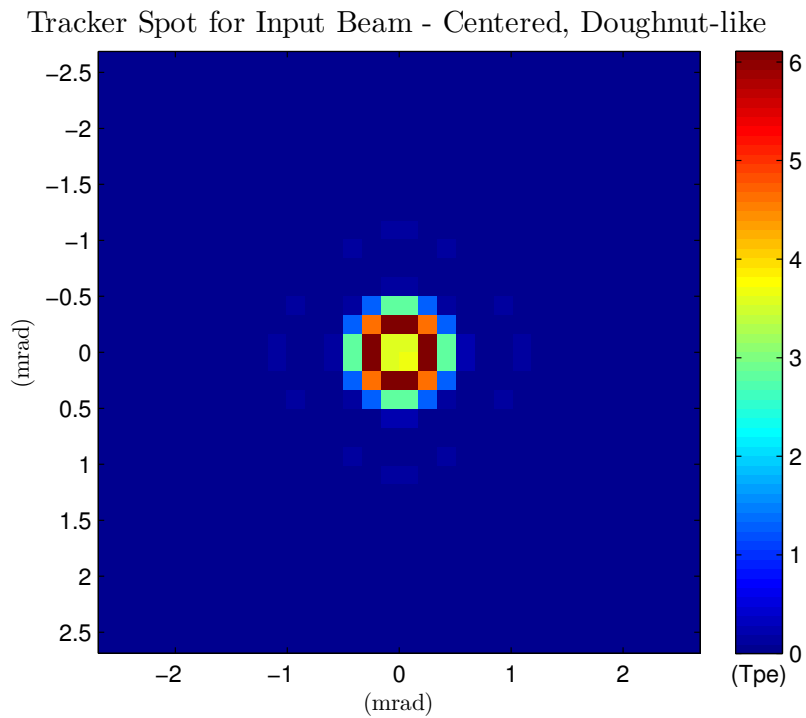


Figure B.2: The tracker image of the input field, from Fig. B.1.

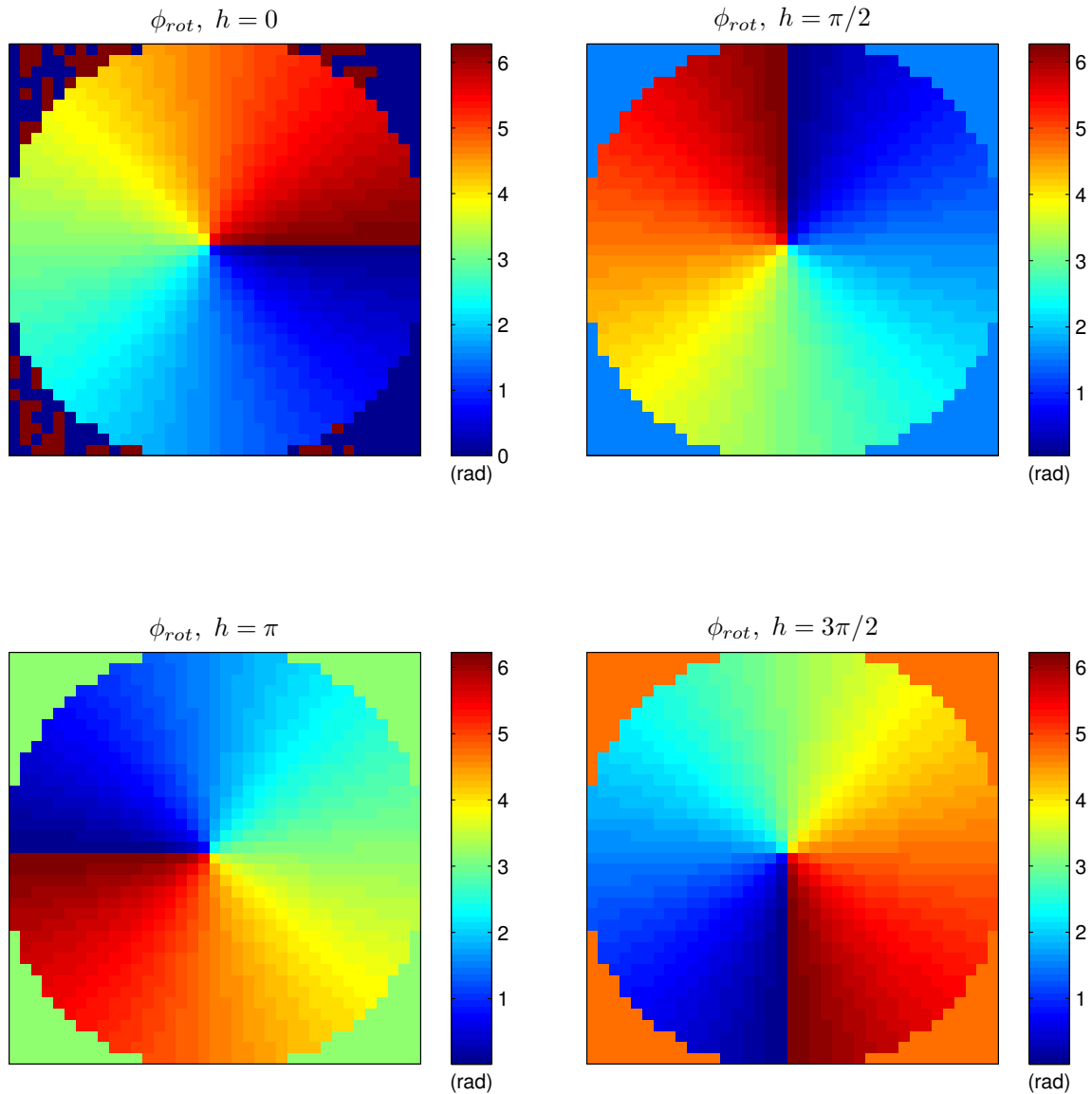


Figure B.3: The four PCO rotational phase realizations from an LSPV+4 reconstructor over the rotational field from Fig. B.1.

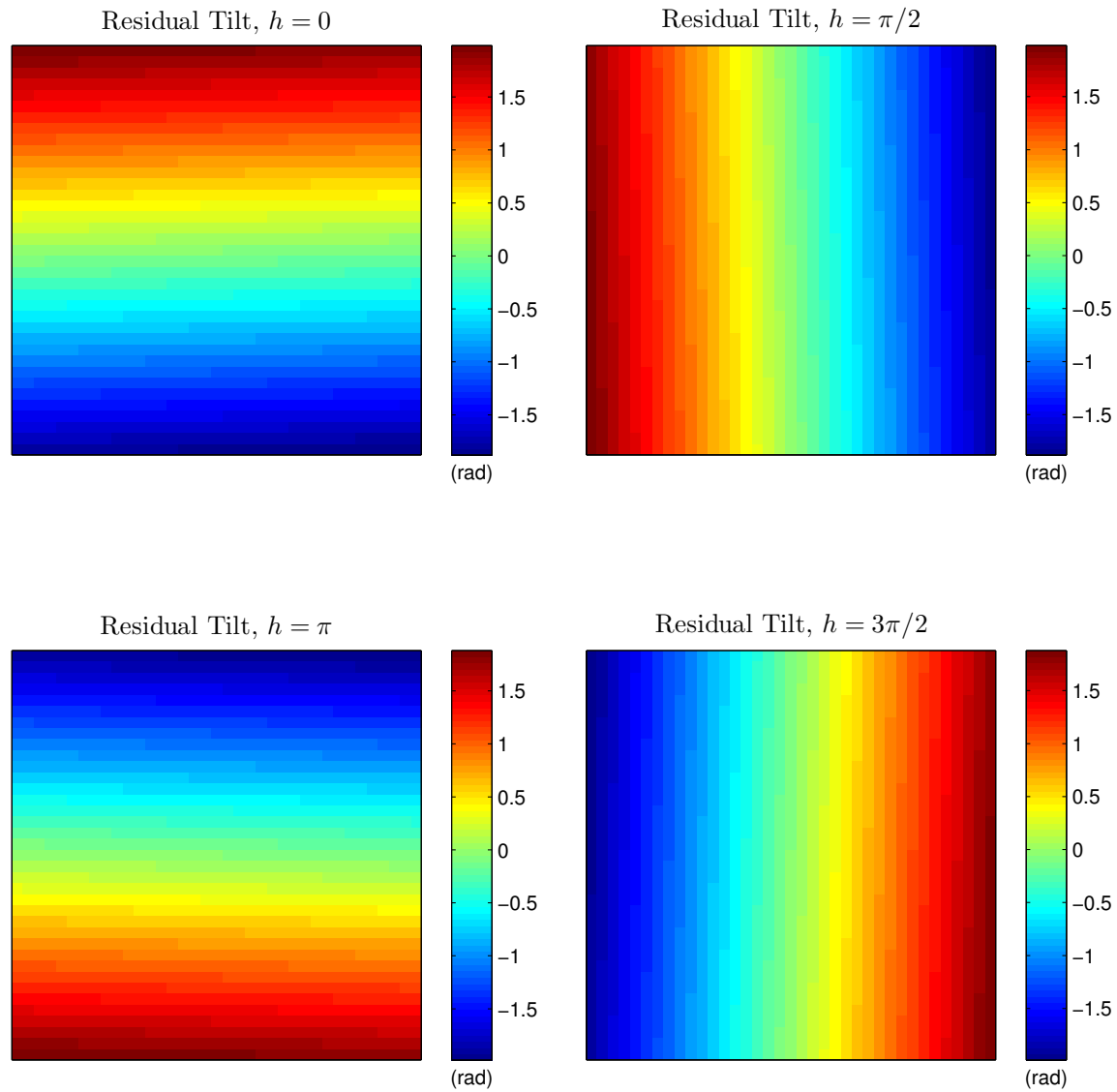


Figure B.4: The four corresponding tilt components from each rotational phase realization of Fig. B.3.

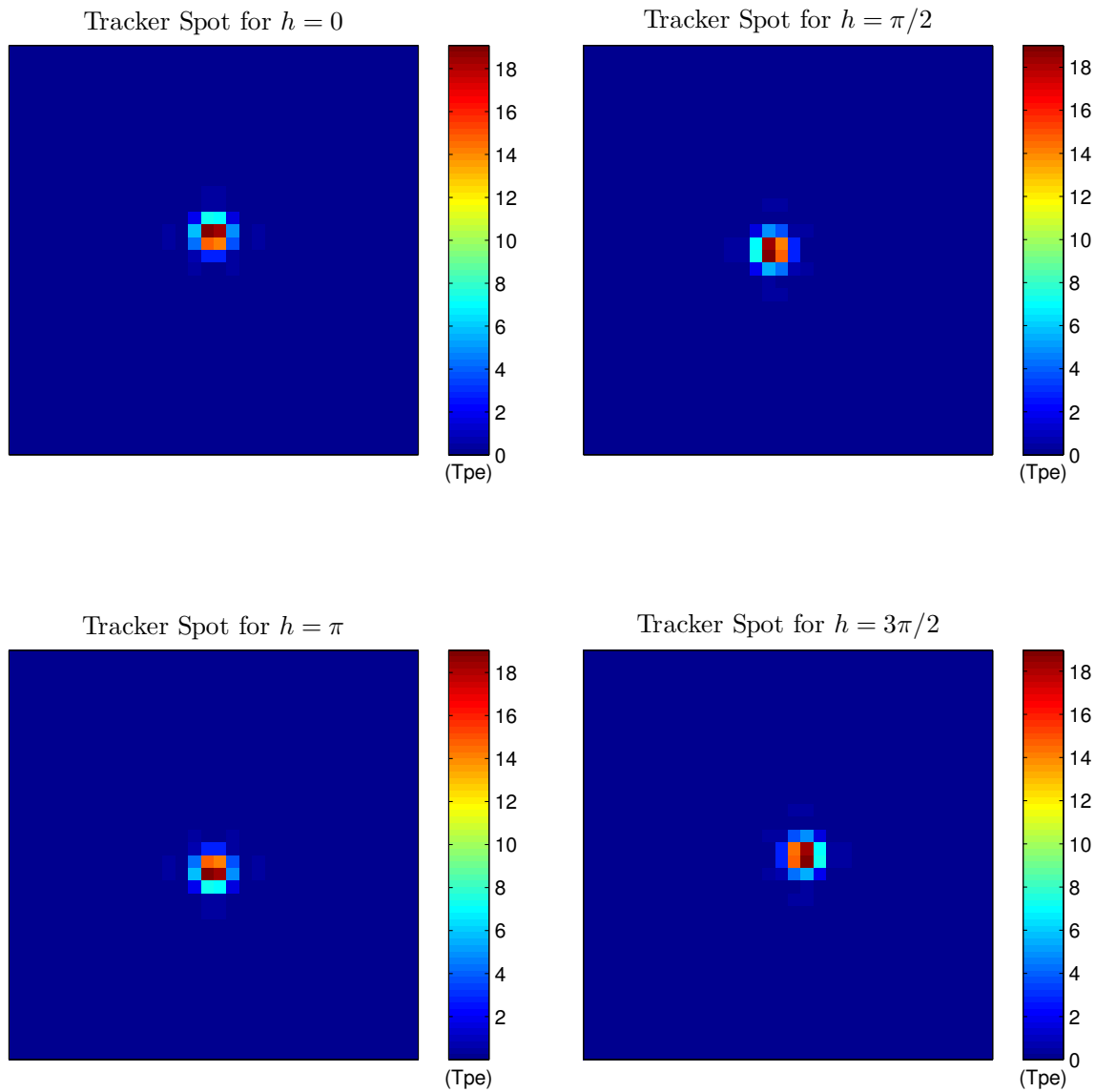


Figure B.5: The four resulting tracker measurements after the higher-order corrections from each rotational phase realization of Fig. B.3.

Bibliography

- [1] *Multi-DM.* Datasheet, Boston Micromachines. URL <http://www.bostonmicromachines.com/vision-science.htm>.
- [2] *Spatial Light Modulators.* Datasheet, Boulder Nonlinear Systems, Inc, November 2010. URL <http://www.bnonlinear.com/products/xyslm/XYSeriesDS0909.pdf>.
- [3] “Fast Steering Mirrors”, 2011. URL http://www.opticsinmotion.net/fast_steering-mirrors.html.
- [4] Andrews, L.C. “An Analytical Model for the Refractive Index Power Spectrum and Its Application to Optical Scintillations in the Atmosphere”. *Journal of Modern Optics*, 39(9):1849–1853, 1992.
- [5] Andrews, L.C. and R.L. Phillips. *Laser Beam Propagation Through Random Media*. Press Monographs. SPIE Press, 2005. ISBN 9780819459480.
- [6] Barchers, J. D. *Control law for a high resolution self-referencing interferometer wavefront sensor used with a low resolution deformable mirror*. Technical Report AR-17, SAIC, Longmont CO, December 2002.
- [7] Barchers, Jeffrey D. and Brent L. Ellerbroek. “Improved compensation of turbulence-induced amplitude and phase distortions by means of multiple near-field phase adjustments”. *J. Opt. Soc. Am. A*, 18(2):399–411, Feb 2001.
- [8] Corrsin, Stanley. “On the Spectrum of Isotropic Temperature Fluctuations in an Isotropic Turbulence”. *Journal of Appl. Phys.*, 22(4):469 –473, apr 1951. ISSN 0021-8979.
- [9] Fried, D. L. “Optical Resolution Through a Randomly Inhomogeneous Medium for Very Long and Very Short Exposures”. *J. Opt. Soc. Am.*, 56(10):1372–1379, Oct 1966.
- [10] Fried, D. L. *Using the Hidden Phase Formulation in Wave Front Reconstruction*. Technical Report TN-100, tOSC, August 1999.
- [11] Fried, D. L. *Four-, Three-, and Two-Bin Algorithms*. Technical Report TN-187, tOSC, December 2004.
- [12] Fried, David L. “Least-square fitting a wave-front distortion estimate to an array of phase-difference measurements”. *J. Opt. Soc. Am.*, 67(3):370–375, Mar 1977.
- [13] Fried, David L. “Branch point problem in adaptive optics”. *J. Opt. Soc. Am. A*, 15(10):2759–2768, Oct 1998.

- [14] Fried, David L. “Adaptive optics wave function reconstruction and phase unwrapping when branch points are present”. *Optics Commun*, 200(16):43 – 72, 2001. ISSN 0030-4018.
- [15] Ghiglia, D.C. and M.D. Pritt. *Two-dimensional phase unwrapping: theory, algorithms, and software*. Wiley-Interscience publication. Wiley, 1998. ISBN 9780471249351.
- [16] Golub, G.H. and C.F. Van Loan. *Matrix Computations*. Johns Hopkins Studies in the Mathematical Sciences. Johns Hopkins University Press, 1996. ISBN 9780801854149.
- [17] Goodman, J.W. *Statistical optics*. Wiley series in pure and applied optics. Wiley, 1985. ISBN 9780471015024.
- [18] Goodman, J.W. *Introduction To Fourier Optics*. McGraw-Hill physical and quantum electronics series. Roberts & Company, 2005. ISBN 9780974707723.
- [19] Greenwood, Darryl P. “Bandwidth specification for adaptive optics systems”. *J. Opt. Soc. Am.*, 67(3):390–393, Mar 1977.
- [20] Hill, R. J. and S. F. Clifford. “Modified spectrum of atmospheric temperature fluctuations and its application to optical propagation”. *J. Opt. Soc. Am.*, 68(7):892–899, Jul 1978.
- [21] Hudgin, Richard H. “Wave-front reconstruction for compensated imaging”. *J. Opt. Soc. Am.*, 67(3):375–378, Mar 1977.
- [22] Janesick, James R. *Photon Transfer*. SPIE Press, 2007.
- [23] MacEvoy, Bruce. “Astronomical Seeing”. Website, 2012. URL <http://www.handprint.com/ASTRO/seeing1.html>.
- [24] Malacara, Daniel. *Optical Shop Testing*. John Wiley & Sons, Inc., 3 edition, 2007.
- [25] Merritt, Paul. *Beam Control for Laser Systems*. Directed Energy Professional Society, 1 edition, 2012.
- [26] Monirabbasi, Salman and Steve Gibson. “Adaptive control in an adaptive optics experiment”. *J. Opt. Soc. Am. A*, 27(11):A84–A96, Nov 2010.
- [27] Noll, Robert J. “Zernike polynomials and atmospheric turbulence”. *J. Opt. Soc. Am.*, 66(3):207–211, Mar 1976.
- [28] Obukhov, A.M. and ARMY Biological Labs Frederick MD. “Structure of the Temperature Field in Turbulent Flow”. 1968.
- [29] Oppenheim, Alan V. and Ronald W. Schafer. *Discrete-Time Signal Processing*. Prentice Hall, 3 edition, 2010.

- [30] Pellizzari, C. and J.D. Schmidt. “Phase unwrapping in the presence of strong turbulence”. *Aerospace Conference, 2010 IEEE*, 1 –10. March 2010. ISSN 1095-323X.
- [31] Pellizzari, Casey. *Phase Unwrapping in the Presence of Strong Turbulence*. Master’s thesis, AFIT, 2010.
- [32] Poyneer, Lisa and Jean-Pierre Véran. “Predictive wavefront control for adaptive optics with arbitrary control loop delays”. *J. Opt. Soc. Am. A*, 25(7):1486–1496, Jul 2008.
- [33] Press, W.H. *Numerical Recipes: The Art of Scientific Computing*. Cambridge University Press, 2007. ISBN 9780521880688.
- [34] Rhoadarmer, T. A. “Development of a self-referencing interferometer wavefront sensor”. J. D. Ginglewski, M. T. Gruneisen, & M. K. Giles (editor), *SPIE Conference Series*, volume 5553 of *SPIE Conference Series*, 112–126. October 2004.
- [35] Rhoadarmer, Troy A., Jeffrey D. Barchers, John D. Ginglewski, Mikhail A. Vorontsov, Mark T. Gruneisen, Sergio R. Restaino, and Robert K. Tyson. “Noise analysis for complex field estimation using a self-referencing interferometer wave front sensor”. volume 4825, 215–227. SPIE, 2002.
- [36] Roggemann, Michael C. and David J. Lee. “Two-Deformable-Mirror Concept for Correcting Scintillation Effects in Laser Beam Projection Through the Turbulent Atmosphere”. *Appl. Opt.*, 37(21):4577–4585, Jul 1998.
- [37] Schmidt, Jason D., Michael J. Steinbock, and Eric C. Berg. “A flexible testbed for adaptive optics in strong turbulence”. 2011. Presented at SPIE Defense, Sensing, and Security Orlando 2011.
- [38] Schmidt, J.D. *Numerical Simulation of Optical Wave Propagation*. SPIE, 2010.
- [39] Steinbock, Michael J., Jason D. Schmidt, and Milo W. Hyde. “Comparison of branch point tolerant wavefront reconstructors in the presence of simulated noise effects”. *Aerospace Conference, 2012 IEEE*, 1 –13. march 2012. ISSN 1095-323X.
- [40] Strang, Gilbert. *Linear Algebra and Its Applications*. Brooks/Cole, Cengage Learning, 4 edition, 2006.
- [41] Tyson, R. *Principles of Adaptive Optics*. Series in Optics and Optoelectronics. Taylor & Francis, 2010. ISBN 9781439808580.
- [42] Tyson, R. K. *Introduction to Adaptive Optics*. SPIE Optical Engineering Press, 2000.
- [43] Tyson, Robert K. and Benjamin W. Frazier. *Field Guide to Adaptive Optics*. SPIE Press, 2 edition, April 2012.

- [44] USAF Chief Scientist. “Technology Horizons: A Vision for Air Force Science and Technology During 2010-2030”, May 2010. Volume 1.
- [45] Venema, Todd M. *Closed-loop Adaptive Optics Control in Strong Atmospheric Turbulence*. Ph.D. thesis, AFIT, 2008.
- [46] Venema, Todd M. and Jason D. Schmidt. “Optical phase unwrapping in the presence of branch points.” *Opt. Express*, 16(10):6985–6998, May 2008.
- [47] Wheeler, Daniel J. and Jason D. Schmidt. “Coupling of Gaussian Schell-model beams into single-mode optical fibers”. *J. Opt. Soc. Am. A*, 28(6):1224–1238, Jun 2011.
- [48] Wheelon, A.D. and A.D. Wheelon. *Electromagnetic Scintillation: Weak Scattering*. Electromagnetic Scintillation. Cambridge University Press, 2003. ISBN 9780521801997.

Vita

Michael J. Steinbock received a B.S. in Electrical and a B.S. in Computer Engineering from Washington University in St. Louis in 2010. He immediately followed up with his Masters degree in Electro-Optics at the Air Force Institute of Technology (AFIT) and plans to continue on for a PhD. At AFIT, Michael manages the OPTECS group adaptive optics (AO) system and helped in the initial system characterization. While at AFIT, Michael also served as the AFIT SPIE Student Chapter President, taking the chapter to several firsts throughout his term. He is a member of Eta Kappa Nu, the Institute of Electrical and Electronics Engineers (IEEE), the International Society for Optical Engineering (SPIE), and the Directed Energy Professional Society (DEPS).

REPORT DOCUMENTATION PAGE

Form Approved
OMB No. 0704-0188

The public reporting burden for this collection of information is estimated to average 1 hour per response, including the time for reviewing instructions, searching existing data sources, gathering and maintaining the data needed, and completing and reviewing the collection of information. Send comments regarding this burden estimate or any other aspect of this collection of information, including suggestions for reducing this burden to Department of Defense, Washington Headquarters Services, Directorate for Information Operations and Reports (0704-0188), 1215 Jefferson Davis Highway, Suite 1204, Arlington, VA 22202-4302. Respondents should be aware that notwithstanding any other provision of law, no person shall be subject to any penalty for failing to comply with a collection of information if it does not display a currently valid OMB control number. PLEASE DO NOT RETURN YOUR FORM TO THE ABOVE ADDRESS.

1. REPORT DATE (DD-MM-YYYY)	2. REPORT TYPE	3. DATES COVERED (From — To)		
14-06-2012	Master's Thesis	Oct 2010–June 2012		
4. TITLE AND SUBTITLE		<p>Implementation of Branch-Point-Tolerant Wavefront Reconstructor for Strong Turbulence Compensation</p> <p>5a. CONTRACT NUMBER</p>		
		<p>5b. GRANT NUMBER</p> <p>F4F5AL2073MG10</p> <p>5c. PROGRAM ELEMENT NUMBER</p>		
		<p>5d. PROJECT NUMBER</p> <p>ENGJON192J</p> <p>5e. TASK NUMBER</p>		
		<p>5f. WORK UNIT NUMBER</p>		
7. PERFORMING ORGANIZATION NAME(S) AND ADDRESS(ES)			8. PERFORMING ORGANIZATION REPORT NUMBER	
<p>Air Force Institute of Technology Graduate School of Engineering and Management (AFIT/EN) 2950 Hobson Way WPAFB, OH 45433-7765</p>			AFIT/GE/ENG/12-45	
9. SPONSORING / MONITORING AGENCY NAME(S) AND ADDRESS(ES)			10. SPONSOR/MONITOR'S ACRONYM(S)	
<p>Air force Office of Scientific Research Kent Miller 3875 Randolph St., Suite 348 Arlington, VA 22203 (703) 696-8573, kent.miller@afosr.af.mil</p>			AFOSR/NE	
			11. SPONSOR/MONITOR'S REPORT NUMBER(S)	
12. DISTRIBUTION / AVAILABILITY STATEMENT				
<p>DISTRIBUTION STATEMENT A: APPROVED FOR PUBLIC RELEASE; DISTRIBUTION UNLIMITED</p>				
13. SUPPLEMENTARY NOTES				
<p>This work is declared a work of the U.S. Government and is not subject to copyright protection in the United States.</p>				
14. ABSTRACT				
<p>Branch points arise in optical transmissions due to strong atmospheric turbulence, long propagation paths, or a combination of both. Unfortunately, these conditions are very often present in desired operational scenarios for laser weapon systems, optical communication, and covert imaging, which suffer greatly when traditional adaptive optics systems either cannot sense branch points or implement non-optimal methods for sensing and correcting branch points. Previous research by Pellizzari presented a thorough analysis of various novel branch point tolerant reconstructors in the absence of noise. In this research a realistic model of the Air Force Institute of Technology's adaptive optics system is developed and used for the first realistic tests of these branch point tolerant reconstructors. Utilizing a self-referencing interferometer as the high-order wavefront sensor—this type of sensor being theoretically immune to scintillation—this effort has extended previous theoretical work by adding realistic noise effects to the SRI's measurements before reconstructing the wavefronts and applying the control law. Not only is the adaptive optics correction shown to outperform the traditional techniques by as much as 126%, but several new theories and refinements to existing theories were discovered along the way. This study provides a foundation to guide hardware implementation in the future, where noise effects will be present.</p>				
15. SUBJECT TERMS				
<p>Adaptive Optics, Wavefront Reconstruction, Optical Communication, Scintillation</p>				
16. SECURITY CLASSIFICATION OF:		17. LIMITATION OF ABSTRACT	18. NUMBER OF PAGES	19a. NAME OF RESPONSIBLE PERSON (ENG) Maj Milo W Hyde IV
a. REPORT	b. ABSTRACT	c. THIS PAGE	UU	140
U	U	U		19b. TELEPHONE NUMBER (include area code) (937) 255-3636 ext. 4371; Milo.Hyde@afit.edu